Extreme ultraviolet hyperspectral coherent diffractive imaging

by

Yijian Meng

Thesis submitted to the
Faculty of Graduate and Postdoctoral Studies
In partial fulfillment of the requirements
For the M.Sc. degree in
Physics

Ottawa-Carleton Institute of Physics
Department of Physics
University of Ottawa

Abstract

We demonstrate hyperspectral imaging using two time-delayed, coherent extreme ultraviolet (XUV) sources. The approach combines broadband XUV high-harmonic generation, holographic imaging, and Fourier transform spectroscopy. The two harmonics sources are spatially separated at generation,and overlap in the far field resulting in a double slit diffraction pattern. We record the two-dimensional intensity modulation as a function of relative time delay; the Fourier transform determines the spatially dependent spectrum. To reduce the delay jitter and improve the spectral resolution, we demonstrate a novel experimental setup that records the relative delay of the two pulses through optical interference. Moreover, we have demonstrated that this broadband approach can be extended to Fourier transform holographic imaging, which avoids extensive phase retrieval computations. Applications include imaging of biological materials near the carbon K-edge.

Acknowledgements

I would like to express the deepest appreciation to my supervisor, Dr. David Villeneuve. I am grateful that he accepted me into this fantastic group, for his continuous support, and invaluable scientific guidance.

I would like to thank David Crane, Bert Avery, Cameron McPhaden, and Andrei Naumov for their technical support and advice on the lab equipment.

I would like to acknowledge Laurent Mercadier and Jeff Fraser for preparing the imaging samples for this thesis.

I am grateful to Dominik Geissler, TJ Hammond, Kyung-Taec Kim, Marko Haertelt, Andre Staudte, and Paul Corkum, for illuminating discussions and ideas. I would like to thank Chunmei Zhang for her kind support and sharing valuable beamtime at atto2. I would also like to acknowledge the help I received from Claude Marceau in the last two weeks of the experiment.

I would like especially to give thanks to my thesis editors: Andre Staudte, TJ Hammond, Dominik Geissler, and David Villeneuve. I am grateful for their generosity and thoughtful comments.

In addition, I would like to thank my family for their unconditional support and all the good friends from the group who have enriched my past two years.

Table of Contents

List of Figures

Chapter 1

Introduction

From the early days of microscopy, where Antonie van Leeuwenhoek observed the first single cell organism, to the first crystallography experiment in which Max von Laue simultaneously confirmed the structure of the crystal lattice and the wave property of X-rays, our understanding of the nature continues to progress as we gain direct access to what was previously hidden [1].

Research in X-ray diffractive imaging continues this great tradition and has begun to provide unprecedented access to the structure and function of proteins and viruses. In this chapter, we briefly summarize the challenges in imaging bio-molecules, and the advantage of X-ray diffractive imaging in comparison to competing technologies, which together have formed a blossoming field of research with multi-billion dollar international funding in the past decade.

The diffraction limit dictates the optimum imaging resolution for conventional imaging systems, and is on the order of the wavelength of the illumination light source. For many bio-molecules, a resolution of a few nanometers is required. This is much smaller than the wavelength of visible light, and so one must turn to either X-rays or electrons.

For a microscope with the capability of direct imaging, there are at least two essential optical elements: the condenser lens acts to condense the illumination onto the sample. and the imaging lens collects the light diffracted from the sample and creates a magnified image of the object.

Conventional X-ray optics include X-ray mirrors and zone plates. X-ray mirrors are capable of focusing X-rays at grazing angle but at the expense of introducing optical

aberrations. Due to this problem, grazing angled mirrors are not suitable for image-forming systems.

In comparison to grazing mirrors, zone plates introduce less optical aberration, but an inherent problem is their low efficiency and difficulties to manufacture with higher image resolution. Zone plates are made from radially symmetric rings which are alternating from opaque to transparent. They focus the incoming light by diffraction from the transparent areas, while blocking light at the opaque regions. The imaging resolution is 1.22 times the finest outermost ring of the zone plate [2]. The zone plate's focal length is dependent on the wavelength and is thus suitable only for monochromatic sources. In the past few years, zone plate manufacturing has improved imaging resolution down to 10 nm with 0.6% efficiency [3]. Given its recent progress, one can be optimistic that the resolution will continue to improve, and complement other imaging methods.

Imaging systems based on electrons are capable of higher illumination flux per area and better imaging resolution in comparison to most x-ray sources. However, interaction between electrons and samples causes short penetration depth and requires samples with thickness on the order of tens of nanometers. In addition, radiation damage to the sample is generally more severe in electron microscopes in comparison to X-rays, which limits the selection of samples.

In contrast to these direct imaging methods, both coherent diffractive imaging (CDI) and crystallography collect the radiation that diffracts through the sample. Since only the intensity of the diffraction pattern is recorded, the phase information that is required to fully reconstruct the image is lost. Phase reconstruction algorithms are needed to recreate a real image of the sample. Crystallography uses a crystallized sample to increase the signal of the diffracted beam, whereas coherent diffractive imaging uses non-crystallized samples but requires more photon flux. A schematic experimental setup for a diffraction experiment is shown in figure 1.1.

The difference between the two approaches (CDI and crystallography) is significant when it comes to flexibility in the imaging sample selection. For crystallography, the sample needs to be crystallized in a perfect condition to ensure its purity, homogeneity, and functionality. The use of noncrystalline samples reduces the difficulty of sample preparation, which is notoriously challenging for larger molecules. Combining the penetration depth of X-ray, and the use of noncrystalline samples, coherent diffractive imaging using X-rays would in principle allow observing samples in their natural environment such as

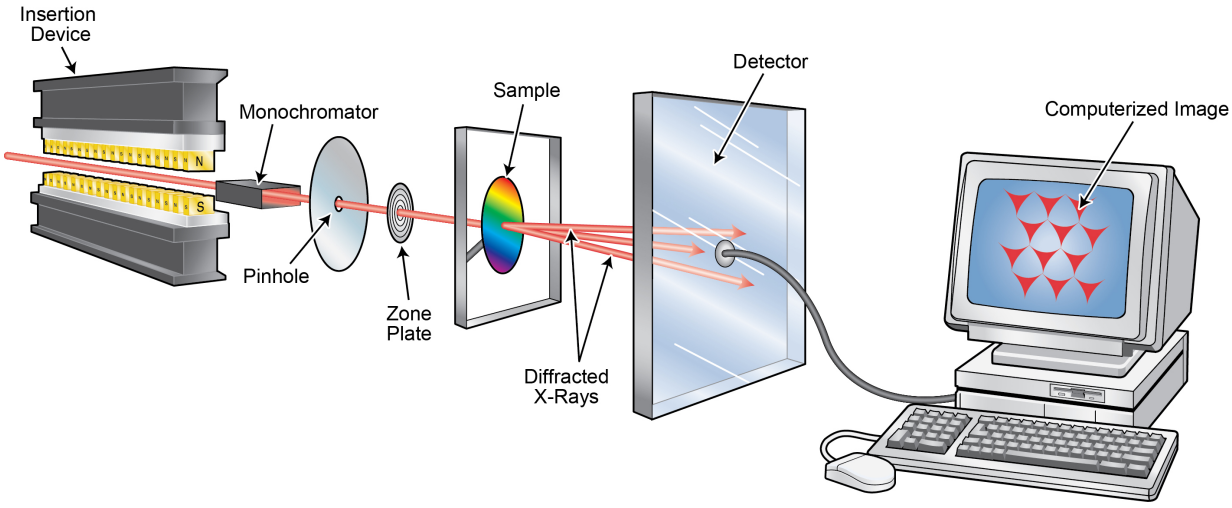

Figure 1.1: The picture illustrates a typical setup for X-ray microscopy. The X-ray source is an undulator in a synchrotron. The emission is spectrally filtered by an monochromator, and a zone plate focuses the X-rays onto the sample. The detector collects the diffracted light, and a computer reconstructs the sample using a phase retrieval algorithm. Picture Credit: Argonne National Laboratory.

water and solutions. An example of coherent diffractive imaging is shown in figure 1.2.

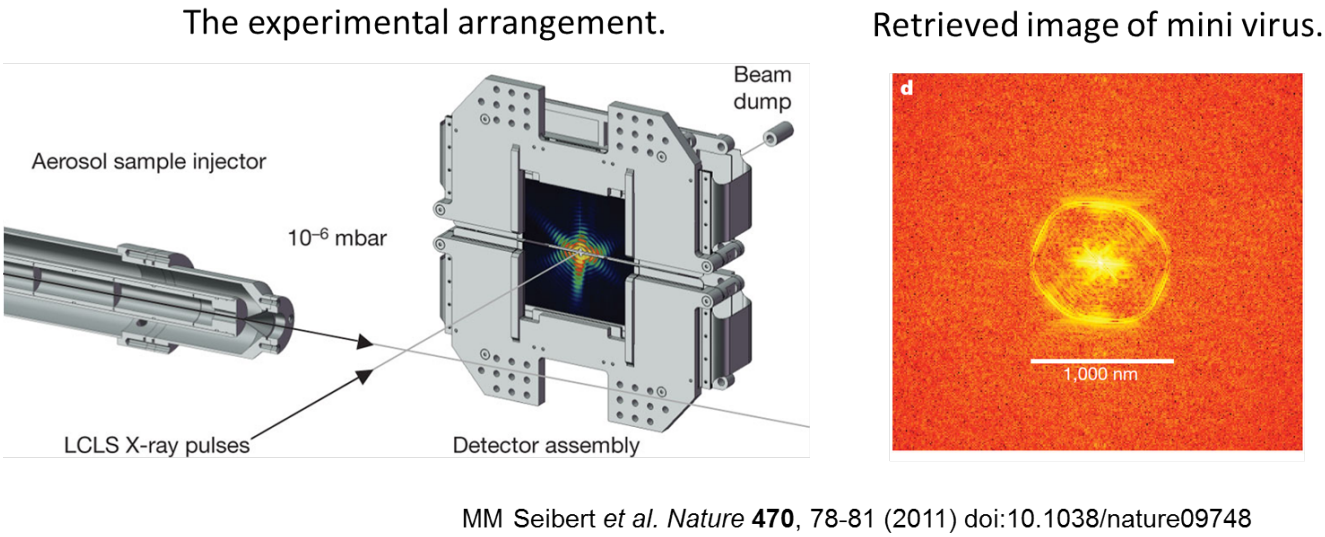

Figure 1.2: An example of recent progress in x-ray coherent diffractive imaging. A single minivirus particle is imaged at 32-nm resolution using the free electron laser at the Linac Coherent Light Source (LCLS) at Stanford University [4].

Within the X-ray spectrum, the "water" window from 2 to 5 nm attracts particular interest for biology and chemistry. The water window extends between the carbon K-edge (280 eV) and the oxygen K-edge (530 eV) [5]. K-edge refers to the increase in photon absorption at the binding energy of the K-shell electron of atoms. The Both elements are abundant in biological and chemical samples. During interaction between photons and atoms, photons are much more likely to be absorbed by the atoms when the photon energy is above the binding energy of an electronic shell. This causes a sudden increase in the attenuation coefficient as the photon energy increases. absorption near the K-edge is not only sensitive to to the element, but also to the local environment of the atom such as neighboring atoms and chemical bonds. For example, the carbon K-edge for phenylene, nitrile and ester groups appears at 285, 286.6 and 288.3 eV, respectively [6]. Water is relatively transparent to soft X-rays in the water window whereas carbon-containing structures within biological samples are highly absorbing [7]. This helps to create high imaging contrast with material sensitivity [8, 9].

The current state of the art X-ray sources are synchrotron and free electron laser light sources. Both sources are large facilities on the scale of hundreds of meters up to kilometers, and cost between hundreds of millions up to billions of dollars [10]. An example of a free electron laser is the Linac Coherent Light Source (LCLS), shown in figure 1.3. The high cost of these facilities means that beam time is expensive and difficult to obtain. Therefore there is a need for smaller-scale alternatives.

A possible alternative to synchrotron facilities is the tabletop high order harmonic generation source (HHG). HHG sources require lasers that can produce millijoule-energy, femtosecond-duration pulses. Femtosecond lasers are commercially available and cost \$250k–1M, which is 2 to 3 orders magnitude less than synchrotron and FEL sources. High order harmonic generation produces a broadband spectrum from XUV to soft X-rays. As of today, the spectrum of HHG sources has already extended into the water window and beyond 1 keV, but increasing the photon flux is still a subject of intense research [7].

In this thesis, we explore a novel imaging technique called hyper-spectral coherent diffractive imaging. Using a broadband light source based on high order harmonic generation, it would provide an ideal platform for collecting spectrally resolved diffraction patterns of a wide range of samples. Once this approach is extended into the water window region, it can provide material sensitivity to imaging of biological or chemical samples by utilizing K-edge absorption of atoms and molecules, while achieving high imaging resolution of a

Figure 1.3: Birds eye view of the Linac Coherent Light Source (LCLS). The instrument was converted from the existing linear accelerator at Stanford Linear Accelerator Center (SLAC) and it achieved first lasing in April 2009. The source is capable of producing a trillion X-ray photons per pulse, at 100 femtosecond pulse duration. The picture shows the 2 mile long linear accelerator [11].

few nanometers with a tabletop X-ray source that will be widely accessible.

The content of the thesis is divided into six chapters. In **chapter 2**, background information of the thesis is provided. The chapter focuses on three separate fields of research: coherent diffractive imaging, Fourier transform spectroscopy and high harmonic generation. They form the basis of the experimental techniques developed in this thesis work. **Chapter 3** describes the experimental methods and image retrieval procedures used in the Fourier transform spectroscopy. In addition, the chapter describes the phase referencing technique, which is a versatile experimental technique with a wide range of applications. **Chapter 4** examines how effect Fourier transform spectroscopy can spectrally filter a selected wavelength . In **chapter 5**, computer simulations are presented to examine the noise effect on four different object retrieval routines. **Chapter 6** presents the main experimental results: the proof of principle test for broadband hyperspectral Fourier transform holography. Finally, **chapter 7** summarizes the achievement of this thesis and its relevance to future research directions.

Chapter 2

Basics

We use high order harmonics of an 800 nm light as our broadband extreme ultraviolet source for coherent diffractive imaging. The method of coherent diffractive imaging is described in section 2.1, and the mechanism of high order harmonic generation is described in section 2.5. The resolution of coherent diffractive imaging increases with narrower bandwidth of the diffracted light. Section 2.6 introduces an older measuring technique called Fourier transform spectroscopy, which we used to spectrally resolve a broadband diffraction pattern and produce effectively a series of narrow bandwidth signals.

2.1 Coherent diffractive imaging

Coherent diffractive imaging (CDI), also called lensless imaging, is a microscopy technique capable of imaging non-crystalline samples. The CDI experiment collects the intensity of the far-field diffraction pattern, and uses phase retrieval algorithm to reconstruct the imaging sample. The diffraction intensity at the far-field is equivalent of the squared Fourier modulus of the object density. In the past decade, CDI has retrieved structural information from a broad range of subjects: nanotubes, nanocrystals, quantum dots, viruses, and cells [12, 13, 14, 15, 16].

The resolution of coherent diffractive imaging is bounded by two limits: The first limit is the diffraction limit [17]:

$$d = \frac{\lambda}{2sin\theta}, \tag{2.1}$$

where λ is the wavelength, θ is the half angle of the maximum cone of light collected after the sample, and d is the imaging resolution at diffraction limit. In theory, diffraction limited image resolution can be improved by measuring at larger θ. However, there's a practical issue: the signal to noise ratio of the recorded diffraction pattern drops at larger angle of the diffracted light after the sample, which is detrimental to the noise-sensitive image reconstruction algorithm.

To demonstrate the lower signal to noise ratio, we have simulated a one dimensional far-field diffraction pattern of an aperture using 40 nm XUV light (see figure 2.1). The diffraction pattern of an aperture has an analytical solution using Fraunhoffer approximation. Given that the state of art optical instrument can focus XUV light down to 10 µm diameter, we assume the same uniform intensity profile before the aperture of 1 µm and 200 nm [18].

As shown in figure 2.1, the intensity of the diffracted light drops more than three order of magnitude at 20 degree off-axis angle for a 1 µm aperture. The narrower aperture has a more even distribution of the diffraction pattern, but the diffraction intensity at higher off-axis angle remains the same. For an imaging system, the main contribution of noise is shot noise, and the signal to noise ratio is the square root of the photon numbers collected at a camera pixel. This means the lower photon flux at higher angle of diffracted light results in lower signal to noise ratio.

This causes a problem in the image reconstruction algorithm since reconstruction routines can be disrupted by noise [19]. As a result, the useful angle of the diffracted light for image reconstruction is limited to brighter region of the diffraction pattern. Longer or more intense illuminations are needed for increasing signal to noise ratio and improving diffraction limited resolution.

The second limit is the spectral limit. The spectral bandwidth has two implications: the temporal coherence length, and the magnification. The temporal coherence length is given by $\Delta\lambda^2/\lambda$. When we collect the diffraction intensity at an off-axis angle, the diffracted lights across the sample has different path lengths. For the path length difference to be the smaller than the temporal coherence length, we can give the following expression: [17, 20]:

$$r \geq \frac{\Delta\lambda z}{P}, \tag{2.2}$$

where r is the image resolution, $\Delta\lambda$ is the spectral bandwidth, z is the distance between

the imaging sample and the imaging plane, P is the size of camera pixel.

The spectral limit based on magnification can be explained as follows: Using the same imaging geometry, the magnification factor is inversely proportional to the wavelength. Therefore, the spectral bandwidth will blur the retrieved object image due to different magnification at different wavelengths.

The spectral limit based on magnification is given by:

$$d_s = \frac{D\Delta\lambda}{\lambda}, \tag{2.3}$$

where d_s is the image resolution, D is the largest dimension of the object.

The spectral limit shows how critical the narrow bandwidth is to the image resolution. At synchrotron sources, the spectral limit is not the limiting factor for imaging resolution since the spectral bandwidth can be as narrow as 1×10^{-4} nm [20]. However, for broadband sources such high order harmonic generation, the spectral bandwidth can be as much as 40 nm. In this case, the spectral limit becomes the main limitation of imaging resolution, and spectral filters are required for higher imaging resolution. However, this leads to loss of photon intensity at the filtered bandwidth, and is at odds with improving the diffraction limited resolution. The idea of coherent diffractive imaging was proposed by Sayre in 1952

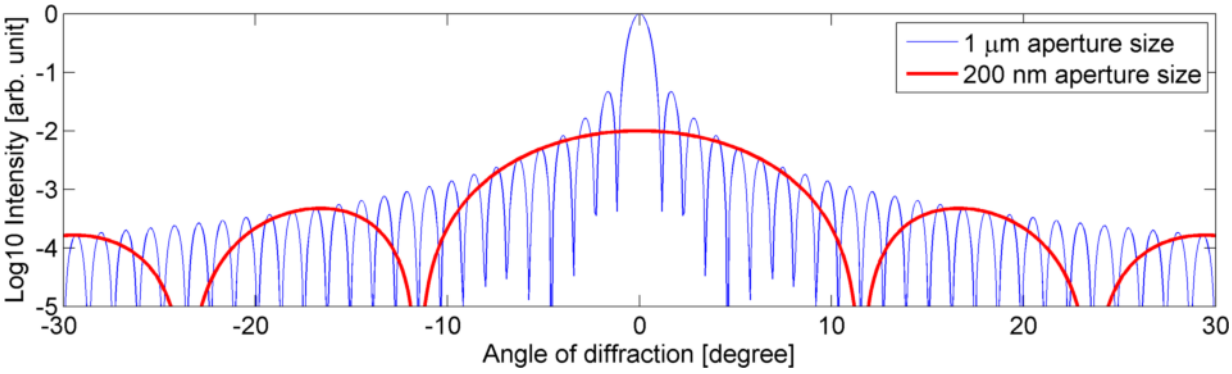

Figure 2.1: Figure shows the far-field diffraction pattern of an aperture; the intensity of the side lobe drops to 10^{-5} at 1 radians off axis.

[21]: if the electron density function describing a single unit cell vanishes outside a, the length of a cell, the structure of a single unit crystal can be completely determined by collecting value in the reciprocal space at $X = 0 \pm 1/a \pm 2/a \pm ...$ The coherent diffractive imaging experiment was not realized until 47 years later than the first proposal, where

Miao et al. demonstrated imaging of a non-crystalline sample at 75 nm resolution using a Synchrotron Light Source [22]. Soon after that, a series of studies were undertaken to image non-crystalline samples using X-rays from synchrotron radiation and free electron lasers, soft X-ray and XUV from high order harmonic sources, and electrons from field emission electron gun [23, 17, 24, 25, 26, 27, 28, 12].

The first experiment of coherent diffractive imaging using a high order harmonic source was conducted by Sandberg et al [17]. The experiment used a pair of narrow bandwidth mirrors to select a single harmonic order. The mirror pair has a combined reflection coefficient of 6 percent. The total acquisition time for the experiment was two hours for maximum spatial resolution of 200 nm. The long acquisition time comes from the lower photon flux at off-axis angle.

In a later paper, coherent diffractive imaging and holography were combined to a new method called Fourier transform holography, where the far-field phase was directly measured using a reference beam. The spatial resolution was improved to 50 nm spatial resolution at one hour acquisition time[23]. Another study by the CEA group shows that by increasing intensity of the driving laser, the photon flux of HHG can be scaled up and retrieve an object image by Fourier transform holographic imaging with a single femtosecond laser pulse [29].

In a 2014 paper, broadband diffractive imaging was achieved based on method of Fourier transform spectroscopy. The spectrum was measured at each camera pixel, and diffraction images were collected simultaneously at multiple wavelengths. However, only near-field diffraction pattern were collected since the dimension of the entire imaging sample is on the mm range, and to achieve far-field imaging requires more than one kilometer of light propagation [30].

2.2 Near-field and far-field diffraction

Coherent diffractive experiments collect the diffracted light from a sample and use the intensity of the diffraction pattern to retrieve the sample. Due to Huygens' principle, each point of the light can be seen as the secondary wave front that acts as a point source. The diffraction pattern is created by the interference of the secondary wave fronts from the sample. The most basic equation for light diffraction is the Kirchhoff diffraction expression. This equation, however, cannot always be solved analytically and is difficult to implement

through numerical methods. There are two separate approximations that can be used to simplify the Kirchhoff diffraction expression. The condition to which one approximation is valid can be determined by Fresnel number F:

$$F = \frac{a^2}{z\lambda}, \tag{2.4}$$

where a is the size of sample, λ is the wavelength, and z is the distance where light has propagated from the object plane(defined in figure 2.2).

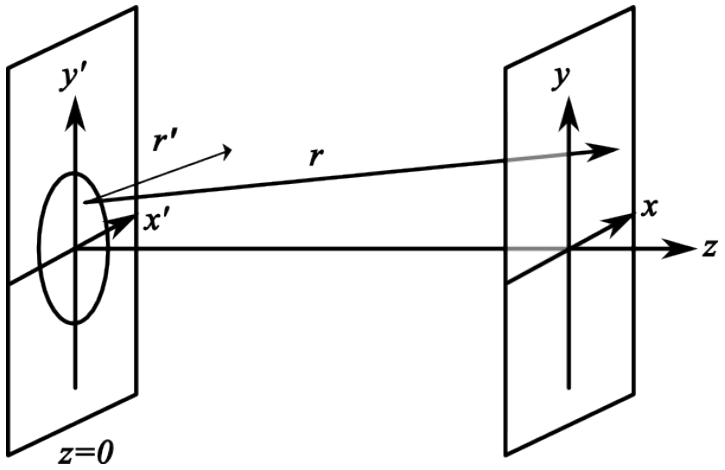

Figure 2.2: z=0 is the object plane, x,y are the coordinates in the imaging plane at z [31].

Fresnel diffraction, also known as near-field diffraction, can be used for when F $\geq$ 1 [32].

$$E(x,y,z) = \frac{e^{ik'z}}{i\lambda z}\int\int_{-\infty}^{\infty} E(x',y',0)e^{\frac{ik'}{2z}[(x-x')^2+(y-y')^2)]}dx'dy', \tag{2.5}$$

where E(x,y,z) is the electric field. k' is the wavenumber of the electric field. x,y,z,x',y' are the spatial coordinate shown in figure 2.2.

Fraunhoffer diffraction, also known as far-field diffraction, is used to describe the wave diffraction after propagation to effectively infinite far away where the electric field from a point source can be approximated as a plane wave. This condition is satisfied when F$\ll$ 1.

$$E(x,y,z) = \frac{e^{ik'z}}{i\lambda z}\int\int_{-\infty}^{\infty} E(x',y',0)e^{\frac{ik'}{2z}(xx'+yy')}dx'dy'. \tag{2.6}$$

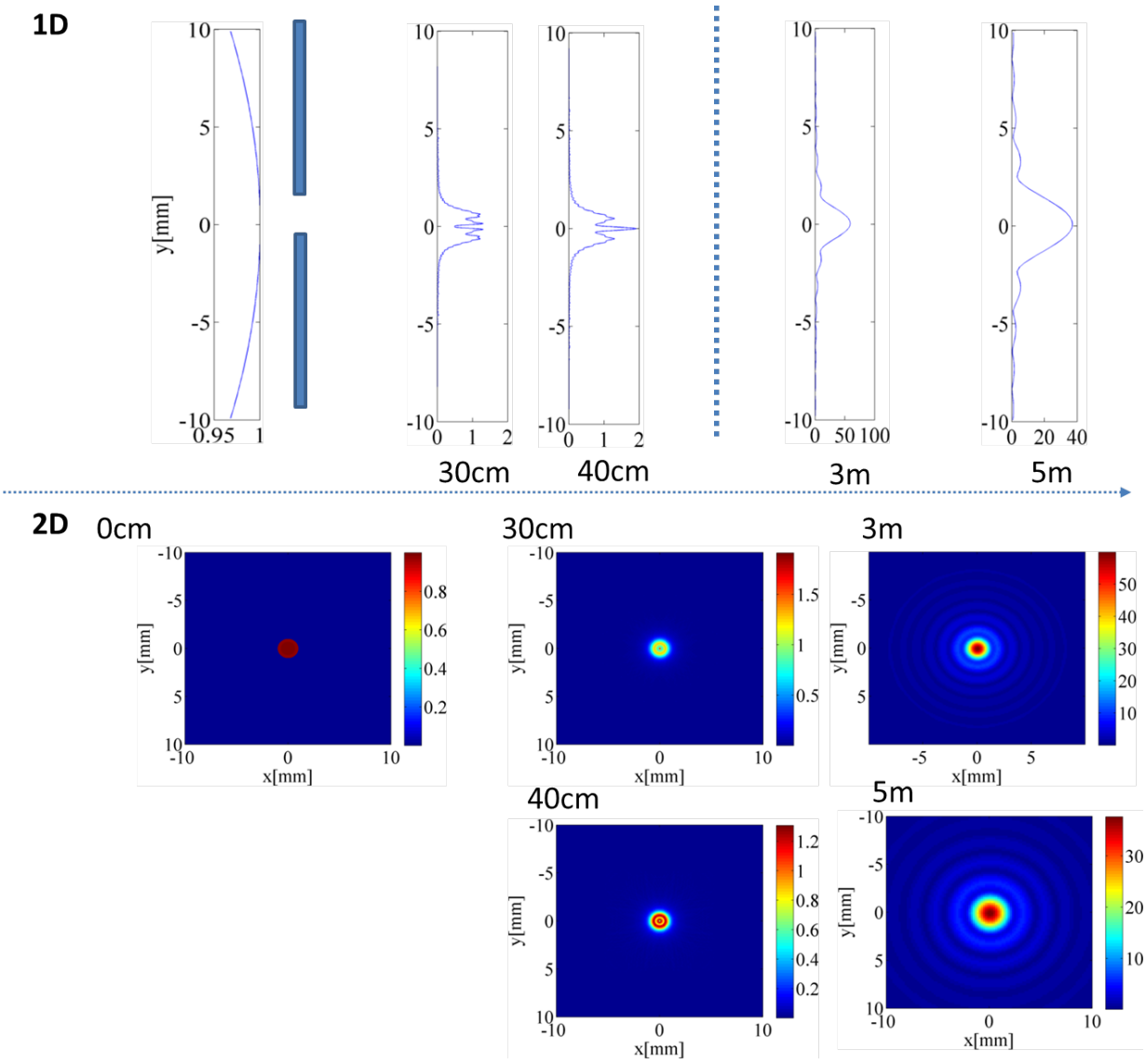

Figure 2.3: Figure shows the diffraction of a Gaussian beam after a 2mm wide aperture. Top graphs show 1D cross section of the diffraction pattern. At the near-field (Fresnel diffraction), diffraction pattern of the beam changes continuously as the beam propagate. In contrast, the diffracted beam in the far-field does not change its shape during propagation; only its size grows bigger. The bottom graphs shows the same information but in 2 dimensions. As the bean propagates, the relative intensity of the ring gradually increases with respect to the center.

By the change of variable,

$$k = (u, v) = (x, y)\frac{k'}{2z}. \tag{2.7}$$

The far-field diffraction can be seen as the reciprocal space of the object space, with k as its coordinate.

$$E(u, v) = \mathcal{F}(E(x, y, 0)). \tag{2.8}$$

Fraunhoffer diffraction is especially useful for phase retrieval algorithms since it links the object plane to the far-field diffraction pattern by Fourier transformation. The intensity of the far-field diffraction pattern is measured in coherent diffractive imaging.

2.3 Phase retrieval

In a coherent diffraction experiment, the complete information of the diffracted light includes both amplitude and phase. However, an imaging system records only the intensity of the diffracted light. Visible light oscillates in the petahertz range, which no existing electronic devices can follow [33]. Only by interference with a known field, phase information can be retrieved with the additional complexity of a holographic setup. Figure 2.4 illustrates the importance of phase.

It is well known that 1D phase retrieval does not have a unique solution [34]. The 1D far-field diffraction pattern is the Fourier transformation of the object. The discrete Fourier transformation is:

$$G(u) = \frac{1}{n}\sum_{x=0}^{n-1} g(x)e^{-iux}. \tag{2.9}$$

Substituting e^{-ix} with α, the equation can be rearranged as a polynomial:

$$G(u) = \frac{1}{n}\sum_{x=0}^{n-1} g(x)\alpha^{u}. \tag{2.10}$$

The fundamental theory of algebra dictates that all polynomials of one variable can be factored. This leads to ambiguity of phase retrieval since each complex conjugate of any factor of the Fourier transform gives the same Fourier domain magnitude. Luckily, the same principle does not apply for polynomial of 2 or more variables; this gives possibility of the 2D phase retrieval problems [35].

Most of the successful phase retrieval algorithms today are modified from the Gerchberg-Saxton algorithm. The Gerchberg-Saxton algorithm can be described as follows: given the modulus of the complex function g and its Fourier pair G, the algorithm iterates between the two functions by Fourier transformation. An initial random phase is assigned to function g as a starting point of the algorithm. The magnitude of g and G is replaced by the known modulus during each iteration. The algorithm converges to an unique solution where the complex phase of G and g are recovered [36].

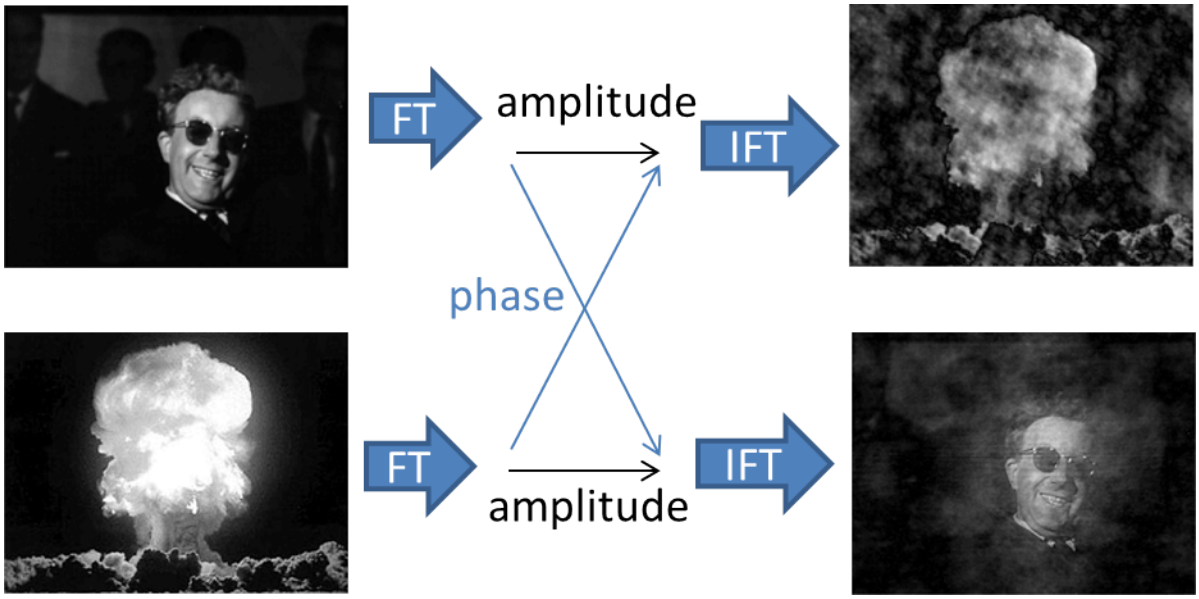

Figure 2.4: The above picture illustrates the importance of phase in image retrieval. For the Fourier transformation of two pictures, their magnitude and phase were switch before performing inverse Fourier transform. It can be shown by combining the phase of the Fourier transformed Dr. Strangelove, and magnitude of Fourier transformed atomic bomb, gives a picture similar to the Dr. Strangelove rather than the bomb.

2.3.1 Variation: Hybrid input output retrieval(HIO)

Fienup proposed a modification of Gerchberg-Saxton algorithm for reconstruction of an object from the modulus of its Fourier transform [37]. The key difference of Fienup's routine from the Gerchberg-Saxton algorithm is that the modulus of the real space is unknown. This is an important improvement because the modulus of the real space is often unknown. The algorithm uses an oversampled intensity measured at the reciprocal

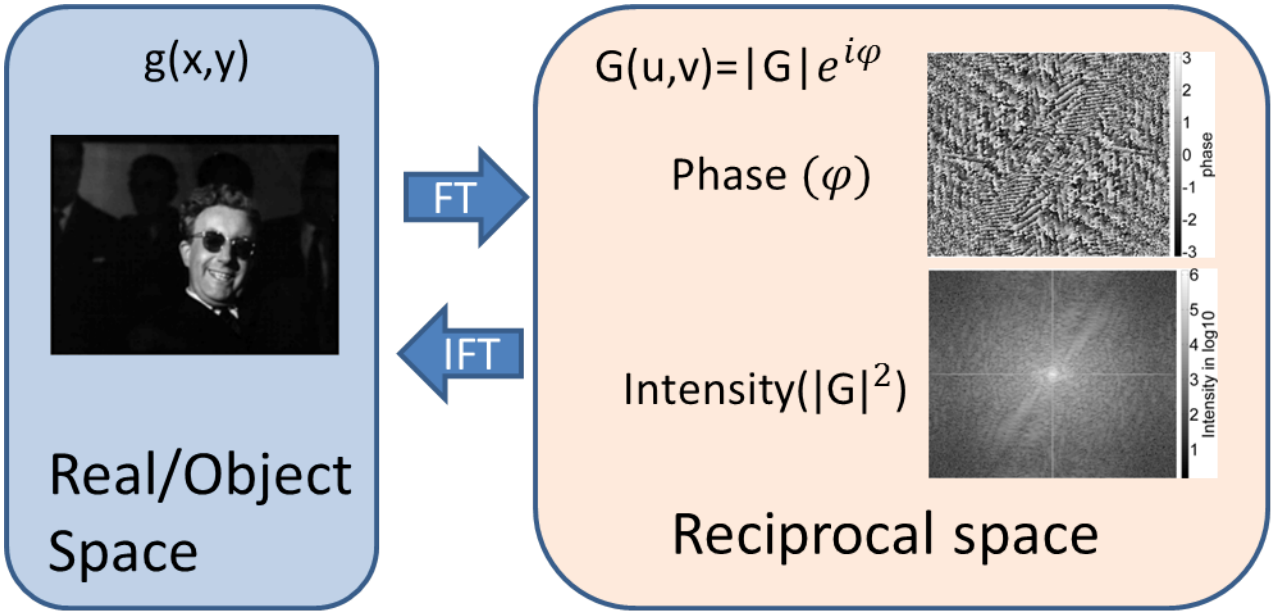

Figure 2.5: Relationship between the real and reciprocal space. In the context of coherent diffractive imaging experiment, the intensity in the reciprocal space is the far diffraction pattern

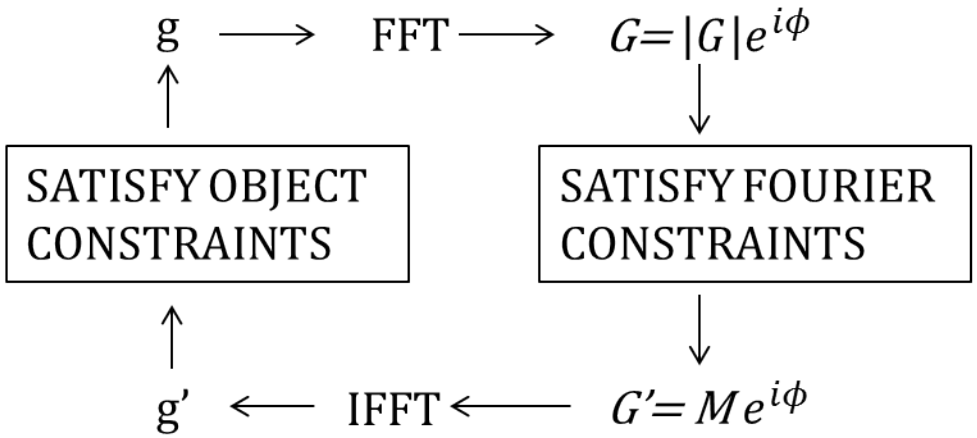

Figure 2.6: Block diagram for iterative phase retrieval algorithm. M is the Fourier modulus of the object, which remains constant at each iteration.

space, which in principle, contains the phase information of real space with fewer sample points. The relation between reciprocal space and real space is illustrated in figure 2.5. To impose convergence of the iteration, prior knowledge about the object was used during the reconstruction.

In real space, the support for phase retrieval includes the size of the object and positivity of the object density. At the beginning of the algorithm, a random phase is assigned to the reciprocal space. Then HIO iterates between reciprocal space and real space while imposing object support and known Fourier modulus (see figure 2.6). For each iteration, the algorithm reduces the amplitude outside the support and imposes positive values in the object space. This ensures the reconstructed object converges to an estimated size while being physically real.

Step 0, this step is used only at the 1st loop of the iteration. Later loops repeat step 1 through step 4 . The Fourier modulus $M(k)$ is obtained by taking the square root of the measured far-field diffraction intensity, $I_{far(k)}$. $k = (u, v)$ are the coordinates of the reciprocal space. After a random phase ϕ is assigned to the Fourier space, inverse Fourier transformation is performed to give a starting point of the iteration. We omit coordinates when there is no ambiguity.

$$g' = \mathcal{F}^{-1}(e^{i\phi}.M), \tag{2.11}$$

where

$$M = |\sqrt{I_{far}}|. \tag{2.12}$$

Step 1, transfer from real space to reciprocal space (see figure 2.2)

$$G = \mathcal{F}(g'). \tag{2.13}$$

Step 2, meet Fourier constraint. Replace amplitude with M, the square root of the measured far field diffraction intensity.

$$G' = M.\frac{G}{|G|)}. \tag{2.14}$$

Step 3, transfer from reciprocal space back to real space, only the real component is taken

$$g' = Re(\mathcal{F}^{-1}(G'))). \tag{2.15}$$

Step 4, apply object support in the real space.

$$g_{i+1}[\varepsilon] = \begin{cases} g'[\varepsilon], & \text{if } \varepsilon \in \gamma \cap g'[\varepsilon] \geq 0, \\ g[\varepsilon] - \beta g'[\varepsilon], & \text{if } \varepsilon \notin \gamma \cup g'[\varepsilon] < 0, \end{cases} \tag{2.16}$$

where $\varepsilon = (x, y)$, the coordinates in the real space, β is a free parameter which controls the strength of the feedback loop. γ is the support in the object domain, it is given by the loose boundary of the sample dimensions. HIO gradually reduces the magnitude outside the object support.

2.3.2 Variation: Oversampling smoothness(OSS)

The OSS phase retrieval algorithm is designed to counter the problem of noisy data [19]. In a typical coherent diffractive imaging experiment, the main source of the noise is the shot noise, which follows a Poisson distribution. This affects more the higher frequencies of the reciprocal space, where the signal-to-noise ratio is lower. The core of OSS phase retrieval algorithm is HIO. The improvement comes from the high frequency filter utilized in the reciprocal space. The algorithm starts out with 100 independent copies. Each sample has a different initial random phase, and goes through its own retrieval loop. The best copy is selected at the end of algorithm based on an error metric defined in the reciprocal space. During the OSS algorithm, the high frequency filter in the reciprocal space gradually decreases its effective cutoff frequency. The filter has a Gaussian distribution, and the standard deviation increases by linear steps at a constant number of iterations, from on the order of N(number of sample point in each dimension) to 1/N.

$$g'_{i+1}[\varepsilon] = \begin{cases} g''[\varepsilon], & \text{if } \varepsilon \in \gamma, \\ \mathcal{F}^{-1}[\mathcal{F}(g''_i).W(k))], & \text{if } \varepsilon \notin \gamma, \end{cases} \tag{2.17}$$

where

$$g''_i[\varepsilon] = \begin{cases} g'[\varepsilon], & \text{if } \varepsilon \in \gamma \cap g'[\varepsilon] \geq 0, \\ g[\varepsilon] - \beta g'[\varepsilon], & \text{if } \varepsilon \notin \gamma \cup g'[\varepsilon] < 0, \end{cases} \tag{2.18}$$

where $\varepsilon = (x, y)$ is the coordinate of the object space, $k = (u, v)$ is the coordinate of the reciprocal space. $W(k)$ is a high frequency filter based on a normalized Gaussian function,

it is defined as follows:

$$W(k) = e^{-\frac{1}{2}(\frac{k}{\sigma})^2}, \tag{2.19}$$

where σ is the standard deviation of a Gaussian distribution.

2.3.3 Variation: Relaxed Averaged Alternating Reflections

Relaxed Averaged Alternating Reflections (RAAR) is a phase retrieval routine proposed by Luke et al [38]. In the original paper, the algorithm is shown to have an order of magnitude improvement of image reconstruction over the hybrid input output algorithm.

To describe RAAR phase retrieval routine, we first define a projector $P_M(g)$:

$$P_M(g(\varepsilon)) = \begin{cases} \mathcal{F}^{-1}(M(\varepsilon)\frac{\mathcal{F}(g(\varepsilon)}{|\mathcal{F}(g(\varepsilon)|)}), & \text{if } \mathcal{F}(g(\varepsilon)) \neq 0, \\ \mathcal{F}^{-1}(M(\varepsilon)), & \text{otherwise ,} \end{cases} \tag{2.20}$$

where $M(\varepsilon)$ is the Fourier modulus of the reciprocal space

R_M is defined as the corresponding reflector for the projector P_M:

$$R_M = 2P_M - I, \tag{2.21}$$

where I is the identity operator

RAAR uses the same iteration step as HIO with step 4 replaced by the following expression:

$$g_{i+1}(x) = \begin{cases} P_M(g_i))(x), & \text{if } n \in D \& R_M(g_i) \geq 0, \\ \beta_i(g_i)(x) - (1-2\beta_i)P_M(g_i)(x), & \text{otherwise,} \end{cases} \tag{2.22}$$

where β_i is a free parameter. For better reconstruction, β_i increases at each iteration from 0.7 to 1.

We compare the speed of image reconstruction between HIO and RAAR algorithms in figures 2.7 and 2.8. They both retrieve a clear image within 3000 iterations.

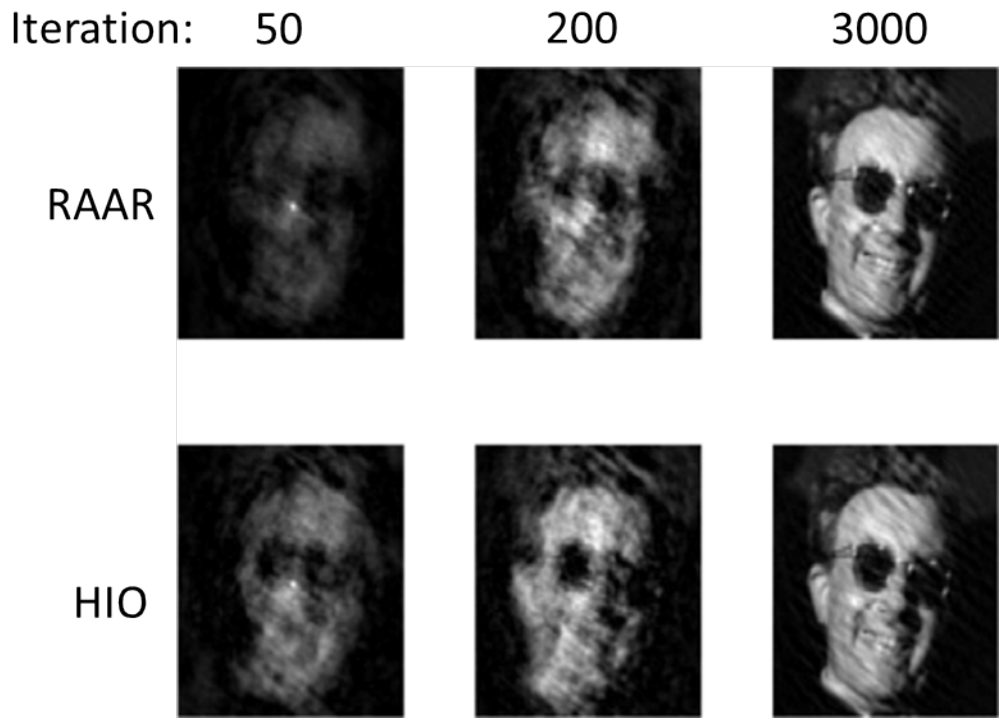

Figure 2.7: Comparison between the image reconstruction speed of HIO and RAAR algorithm. The two algorithms give similar performance given the same initial condition.

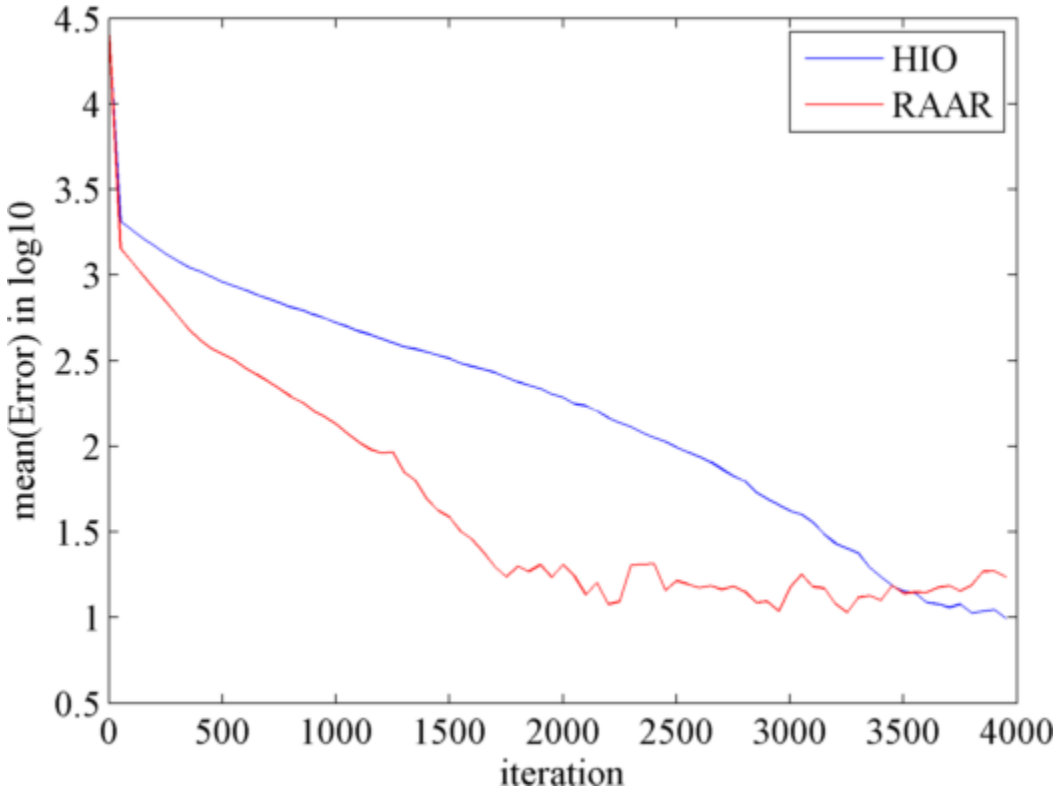

Figure 2.8: The error is measured by the difference between the modulus of reciprocal space at each iteration and the known modulus of reciprocal space. The RAAR gives a superior convergence speed to the known modulus. However, the quality of the recovered image are comparable based on figure 2.7.

2.4 Fourier transform holography

Fourier transform holography was introduced by Guizar-Sicairos et al [39]. It combines coherent diffractive imaging and holography for direct phase retrieval. This allows direct imaging of a sample without using an iterative phase retrieval algorithm. In this approach, the far-field diffraction of a known object acts as a reference beam. The known object can be a point source reference using a small aperture, or an extended reference slit. Here, we show the derivation of Fourier transform holography.

Consider a known object that acts as reference r, and an unknown object o that are at a different position. We call the sum of the two objects as g.

$$g(x, y) = o(x, y) + r(x, y). \tag{2.23}$$

Assume g is illuminated by a plane wave. g is then proportional to the electric field at the object plane. Here, we ignore the factor of proportionality as it does not change our result, and use g as our electric field in the object plane, which is our object space.

In coherent diffractive imaging, the intensity of far-field diffraction pattern is recorded on an imaging device. This intensity distribution is the equivalent of the absolute square of the Fourier transformation of g.

$$I_{far} = M^2 = |\mathcal{F}(g)|^2 . \tag{2.24}$$

As shown in appendix A.2, the inverse Fourier transform of I_{far} gives us the auto-correlation of the original object g:

$$\mathcal{F}^{-1}(I_{far}) = \mathcal{F}^{-1}[|\mathcal{F}(g)|^2] = g \otimes g. \tag{2.25}$$

Using equation 2.23, we can expand equation 2.25 in terms of the unknown object o and the reference object r

$$g \otimes g = o \otimes o + r \otimes r + r \otimes o + o \otimes r. \tag{2.26}$$

Now consider using a single slit reference:

$$l_{slit}(x,y) = l(x)\delta(y - y_o), \tag{2.27}$$

where

$$l(x) = \begin{cases} 0 & \text{if } x < -L/2, \\ 1 & \text{if } -L/2 \leq x < L/2, , \\ 0 & \text{if } x \geq L/2, \end{cases} \tag{2.28}$$

where L is the length of the single slit.

With the single slit reference, we can apply a linear operator $\mathcal{L} = \frac{d}{dx}$ to equation 2.26 to recover the object.

$$\mathcal{L}(f \otimes f) = \mathcal{L}(o \otimes o) + \mathcal{L}(r \otimes r) + \mathcal{L}(r \otimes o) + \mathcal{L}(o \otimes r). \tag{2.29}$$

It can be shown in appendix A.5 that:

$$\mathcal{L}(r \otimes o) = -\mathcal{L}(r) \otimes o = r \otimes \mathcal{L}(o). \tag{2.30}$$

with this property, we have:

$$\mathcal{L}(f \otimes f) = \mathcal{L}(o \otimes o) + \mathcal{L}(r \otimes r) - \mathcal{L}(r) \otimes o + o \otimes \mathcal{L}(r). \tag{2.31}$$

$\mathcal{L}(r)$ gives us the derivative of a single slit, a two-point Dirac Delta function:

$$\mathcal{L}(r) = \frac{d(l(x)\delta(y - y_o))}{dx} = -\delta(x - L/2)\delta(y - y_o) + \delta(x + L/2)\delta(y - y_o). \tag{2.32}$$

Now we substitute 2.32 into 2.31, the last two terms of equation 2.31 then becomes:

$$\begin{aligned} &- \mathcal{L}(r) \otimes o + o \otimes \mathcal{L}(r) \\ &= [\delta(x - L/2)\delta(y - y_o) - \delta(x + L/2)\delta(y - y_o)] \otimes o + ... \\ &\quad o \otimes [-\delta(x - L/2)\delta(y - y_o) + \delta(x + L/2)\delta(y - y_o)] \\ &= o(x + L/2, y + y_o) - o(x - L/2, y + y_o) - o(-x + L/2, -y + y_o) + o(-x - L/2, -y + y_o). \end{aligned} \tag{2.33}$$

Here we use the sifting property of the Dirac Delta function inside a cross-correlation (See Appendix A.7, A.8). This gives us four copies of the object.

The first two terms of the equation 2.31 are the derivatives of the autocorrelation function of o and r, which are not used in the object retrieval.

$$\frac{d}{dx}(o \otimes o + r \otimes r). \tag{2.34}$$

For implementation with discrete data, the derivative of the single slit is taken in the reciprocal space using the following property (see appendix A3) [39]:

$$\mathcal{L}(\mathcal{F}^{-1}(I_{far})) = \mathcal{F}(iu.I_{far}). \tag{2.35}$$

where u is the coordinate in the reciprocal space, which corresponds to the slit direction in the object space, and i is the imaginary unit.

The entire retrieval procedure can be summarized as follows:

$$\begin{aligned}\mathcal{F}(iu.I_{far}) &= \frac{d}{dx}[o \otimes o + r \otimes r] + ... \\ &o(x + L/2, y + y_o) - o(x - L/2, y + y_o) - o(-x + L/2, -y + y_o) + o(-x - L/2, -y + y_o).\end{aligned} \tag{2.36}$$

If the spacing between o and r is greater than the size of the autocorrelation of o and r, the first two terms of equation 2.36 do not overlap spatially with the last four terms, and we can retrieve four isolated copies of the object. Since Fourier transform holography uses the diffraction intensity at the reciprocal space, its image resolution is subject to the diffraction limit and spectral limit. In addition, the resolution of the Fourier transform holography is also determined by the size of the reference. In the case of a reference slit, the retrieved resolution is greater or equal to the width of the slit.

2.5 HHG as source

High order harmonic generation is a highly nonlinear process between the intense laser source and atoms/molecules [40, 41]. A characteristic of high order harmonics is that it exhibits a plateau region where a relative flat intensity can be observed across a broad spectrum [42]. This differentiates it from the landscape of perturbative harmonic gener-

ation, where the signal goes down exponentially as the harmonic order increases. The physical origin of this phenomenon was later explained by an intuitive model introduced by the seminal paper of Paul Corkum, where the harmonic generation process is broken down into a three step model [43].

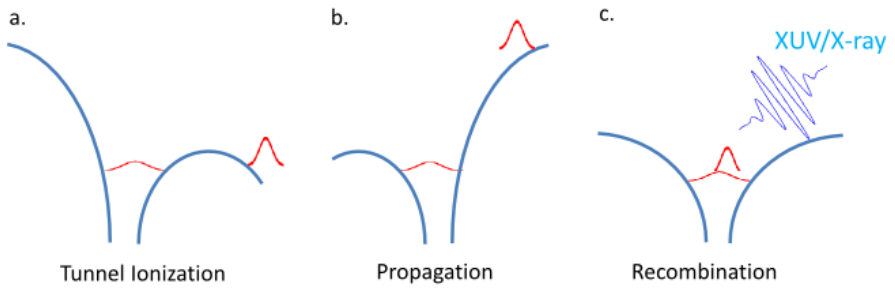

Figure 2.9: Cartoon figure for three step model.

1. The electron wave packet tunnels out in the presence of an intense laser field (2.9 a)
2. Free electron accelerates in the laser field (2.9 b.)
3. Electron wave packet recombines with the parent electron and emits high order harmonic (2.9 c.)

The three step model suggests that the plateau comes from the frequency of the continuum wave package as it was accelerated in the presence of the electric field. The emitted photon from high order harmonic generation carries the frequency structure of the free electron wave packet upon re-collision. Due to this unique feature, high order harmonic generation can produce short wavelength radiation. Harmonic emission occurs at each half cycle. For multi-cycle driving pulses, the spectrum of high order harmonic generation exhibits distinctive harmonic peaks at odd number multiples of the driving photon energy (see figure 2.12). This is due to destructive interference between two consecutive half laser cycles.

The highest harmonic produced with a given ionization potential of an atom or a molecule is approximately:

$$E_{max} = I_p + 3.17U_p, \tag{2.37}$$

where U_p is the ponderomotive energy F^2/ω^2, F is the laser electric field, ω is the frequency, I_p is the ionization potential, E_{max} is energy cutoff for the high order harmonics.

As shown in the cutoff equation, the harmonic cutoff energy increases by $I\lambda^2$ due to the increase in the ponderomotive energy, where λ is the wavelength of the driving beam. Naturally, higher cutoff energy requires increasing laser intensity and using longer wavelength. However, increasing laser intensity can lead to ionization saturation caused by a pre-pulse, which prevents high order harmonic generation at the peak laser intensity. Longer wavelength increases the time that the electron packet spends in the continuum. This causes the spreading of the wave function and decrease the possibility of recombination from recollision. The scaling law for high harmonic conversion efficiency is proportional to $\lambda^{-6.5}$ in Kr [44]. Despite these experimental challenges, several groups have demonstrated promising results for HHG well into the X-ray spectrum [7, 45, 46].

2.5.1 Setup for HHG

The most common driving laser source for high order harmonic generation is the Ti:sapphire pulsed laser at 800 nm with femtosecond pulse duration. Ti-sapphire crystals have high damage threshold which allows higher photon input.

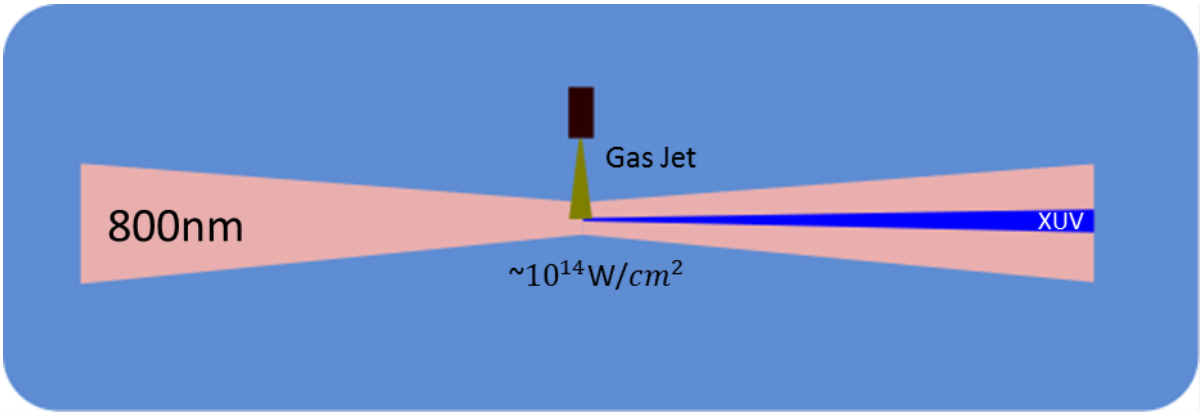

Figure 2.10: The figure shows a typical setup for high order harmonic generation. The 800 nm light is focused into a vacuum chamber at photon intensity on the order of $10^{14}W/cm^2$ High order harmonics are produced at the laser focus.

To use high order harmonic as a light source, the gas is usually chosen to be an inert gas with higher ionization potentials in comparison to reactive gas. Due to absorption

of XUV in atmosphere, HHG sources are inside vacuum chambers. A typical pressure in vacuum chamber is 10^{-3} mtorr. Figure 2.10 shows a typical setup for high order harmonic generation.

2.5.2 Simulated high order harmonic generation

We performed simulation of high order harmonic generation of a single atom using an numerical routine based on the Lewenstein model [47, 48]. Figure 2.11 shows the simulated high order harmonic emission from a few cycle 800 nm pulse with $1 \times 10^{14} W/cm^2$ at the peak intensity laser intensity. With high order harmonics emission at each half cycle, the multi-cycle driving pulse produces a train of XUV pulses. The gas medium used in the simulation is Argon. Figure 2.12 shows the power spectrum of the HHG emission in figure 2.11. On a linear scale, we can observe visible harmonic peaks from 13 eV to 41 eV, corresponding from the 9th harmonic to the 27th harmonic.

Figure 2.11: HHG emission of few cycle laser pulse. Harmonic pulse emits at each half cycle of the driving electric field E(t).

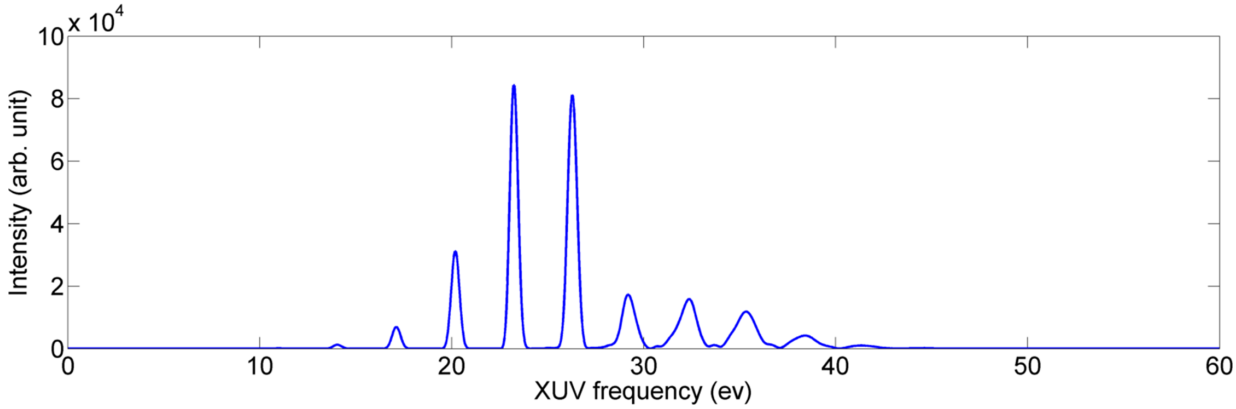

Figure 2.12: Simulated power spectrum from high order harmonic generation. The harmonic peaks are at the odd multiple photon energy of the driving laser field.

Figure 2.13 shows the spectrally filtered HHG emission at the 17th harmonic with 1 eV or 0.1 eV bandwidth. The narrower bandwidth of the filtered HHG emission corresponds to longer emission time. Figure 2.14 shows both the autocorrelation trace of the high order

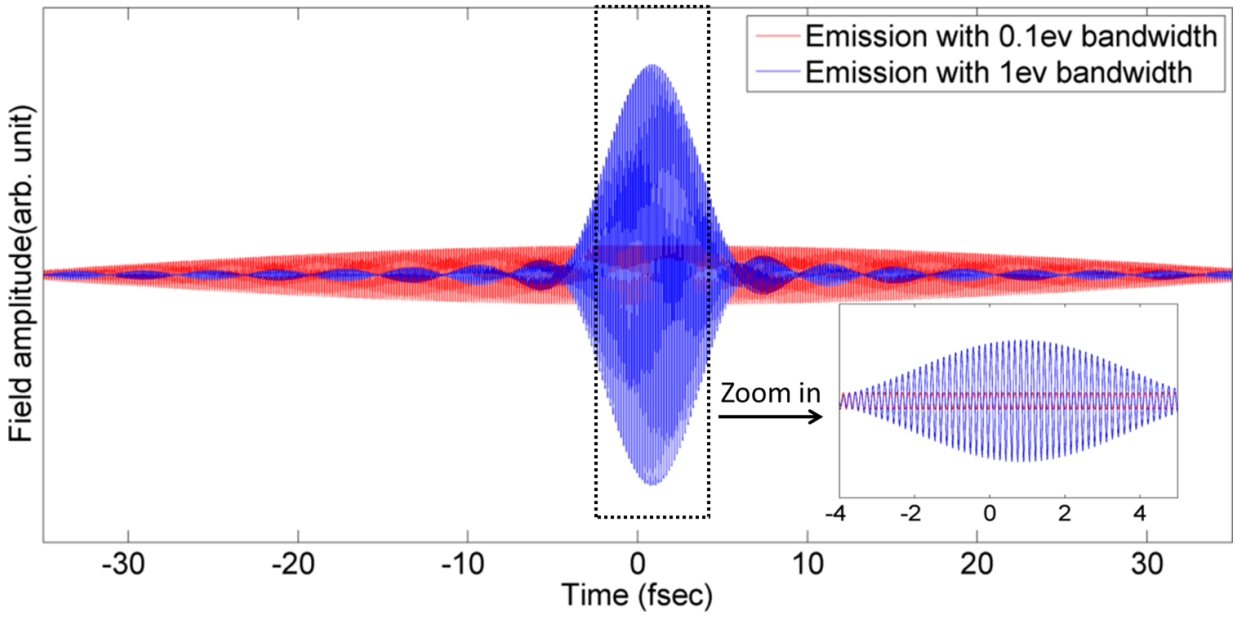

Figure 2.13: Simulated HHG emission at 17th harmonic with 1 eV or 0.1 eV bandwidth. The narrower bandwidth of the filtered emission corresponds to longer emission time.

harmonic emission and its the spectrally filtered emission. The coherence length of electric field corresponds to the full width half maximum of the auto-correlation function, which is given by:

$$L_c = \frac{c}{n\Delta f} \tag{2.38}$$

where Δf is the bandwidth of the electric field, c is the speed of light, and n is the dielectric constant of the optical medium. Our simulation using spectrally filtered high order harmonics agrees qualitatively with the equation. Hence, to retrieve with a narrower spectral resolution, a longer time scan is required to cover its corresponding coherence length.

2.6 Fourier transform spectroscopy

Fourier transform spectroscopy is a measuring technique that allows the simultaneous collection of spectral information from broadband sources [49]. This approach improves the signal to noise ratio by a factor of N (number of resolved frequencies) in comparison to the direct intensity measurement with a monochromator. Using the fact that the autocorre-

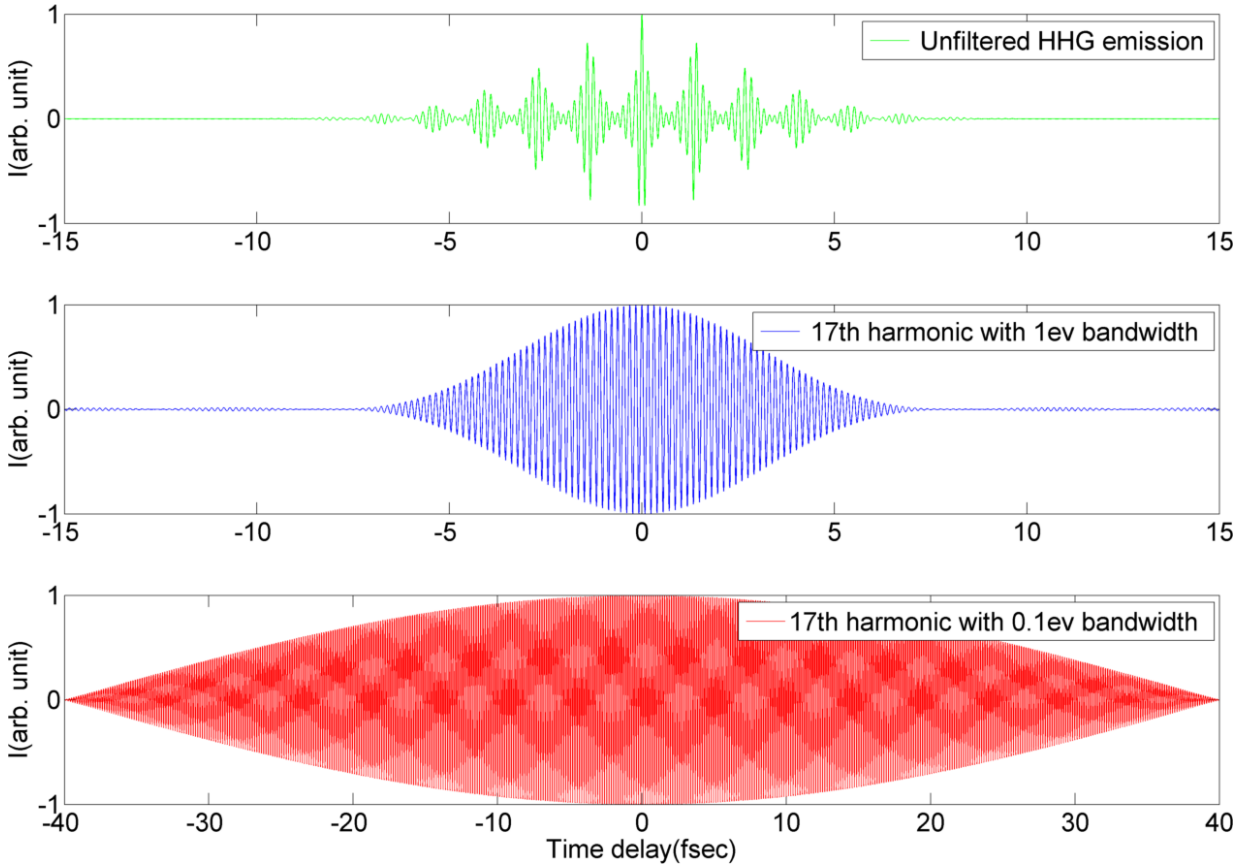

Figure 2.14: Simulated autocorrelation trace of HHG emission and its spectral filtered emission at 17th harmonic with 1 eV or 0.1 eV bandwidth. The narrower bandwidth corresponds to longer full width at half maximum.

lation trace and the power spectrum represents a Fourier pair (see appendix A.2), we can collect a discrete autocorrelation trace in order to obtain the power spectrum.

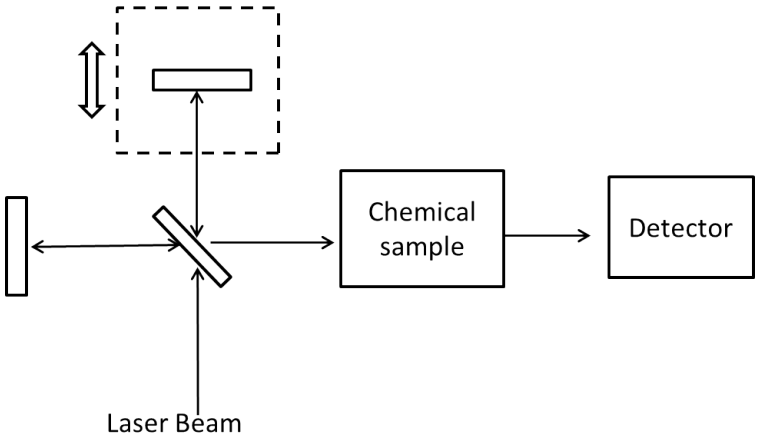

Figure 2.15: Schematic diagram of Fourier transform spectroscopy.

A typical setup for Fourier transform spectroscopy is a Michelson interferometer. A coherent light source is split into two identical copies by a beam splitter. One beam is reflected by a stationary mirror and the other by a moving mirror. The two beams would travel through different path lengths before they recombine at the output. The path length is tuned by the position of the moving mirror. As the moving mirror scans through different positions, the two beams produce different interference patterns at different relative time delay. The intensity of the time integrated interference pattern is collected at a discrete time delay to extract an autocorrelation function. A sample is often placed in the recombined beam to collect its absorption spectrum. For an arbitrary electric field $E(\tau)$ with finite pulse duration, where the field strength is zero outside [-T,T], the signal output from a Michelson interferometer can be described as follows:

$$\begin{aligned} I_\omega(\tau) &= \int_{-T}^{T} |E(t) + E(t+\tau)|^2 dt \\ &= \int_{-T}^{T} [E(t) + E(t+\tau))(E^*(t) + E^*(t+\tau))] dt \\ &= \int_{-T}^{T} [E(t)E^*(t) + E^*(t+\tau)E(t+\tau) + E(t)^*E(t+\tau) + E(t)E^*(t+\tau)] dt \\ &= \int_{-T}^{T} [2E(t)E^*(t) + 2Re(E(t)E^*(t+\tau))] dt, \end{aligned} \tag{2.39}$$

where τ is the time delay between the two identical signals, I is the signal received at the camera at each delay, $E(t)$ is the electric field.

Rewrite E(t) as a Fourier series

$$E(t) = \sum_{\omega=-\infty}^{\infty} \frac{E(\omega)e^{i\omega t}}{\sqrt{2T}}, \tag{2.40}$$

where ω is the frequency and $\sqrt{2T}$ is a normalization factor for the definite integral

$$\begin{aligned} I_\omega(\tau) &= \frac{\int_{-T}^{T} 2E(\omega)E^*(\omega)dt}{2T} + \sum_{\omega=-\infty}^{\infty} E(w)2\frac{Re(\int_{-T}^{T} e^{i\omega t}e^{-i\omega(t+\tau)}dt)}{2T} \\ &= \sum_{\omega=-\infty}^{\infty} 2|E(\omega)|^2 + |E(\omega)|^2 cos(\omega\tau). \end{aligned} \tag{2.41}$$

The first term has a constant value for all delay positions. The second term shows that the signal measured at each delay can be rewritten as a Fourier cosine Series with coefficient of spectral intensity. This term gives the spectral intensity after Fourier transformation, and is used as our autocorrelation function.

The highest frequency that can be obtained from Fourier transform spectroscopy is determined by the sampling rate. For a discrete-time system of sampling rate f_s, $0.5f_s$ is its Nyquist frequency. The frequency component above Nyquist frequency is indistinguishable from the lower-frequency component [49]. To avoid this effect, the autocorrelation trace should be sampled with a frequency greater than the Nyquist frequency of its highest significant frequency content. The highest frequency from a discrete time scan is inversely

proportional to the delay steps.

$$f_m = f_s/2 = \frac{1}{2\Delta t}, \tag{2.42}$$

where f_m is the highest frequency sampled, and Δt is the length of each delay step.

The spectral resolution of Fourier transform spectroscopy is inversely proportional to the length of the scan:

$$\frac{1}{N\Delta t} = \Delta f, \tag{2.43}$$

where N is the number of the delay step, Δt is the length of each step, and Δf is the resolution in the frequency domain.

One of the first XUV Fourier transform spectroscopy experiments was done by Kovacev et al [50]. Their setup used a traditional Michelson interferometer inside a vacuum chamber. This arrangement reduces the noise generated from air fluctuations. The lowest detectable harmonic was at 89 nm. In a subsequent work, Nabekawa et al. measured the coherence length of an attosecond second pulse train [51]. Instead of delaying the fundamental beam, they directly split the XUV by a couple of D shaped mirrors. The auto-correlation trace is then obtained by delaying one of the D-mirror using a piezo-stage. They were able to resolve harmonics as high as the 25th at the zero order diffraction of a grating, and the 33rd in the first order diffraction. The zero order diffraction contains harmonics of different orders, thus the noise of different frequencies accumulate at the same pixel of the imaging device. At first order diffraction, the harmonics are spatially separated and the noise of each harmonic only influences its own autocorrelation trace.

Chapter 3

Experimental method

The imaging resolution from coherent diffraction imaging decreases with increasing source bandwidth (see section 2.1). In order to utilize a broadband high order harmonic source, a common approach is to spectrally filter out a single harmonic. This approach leads to a tradeoff between the imaging resolution imposed by the spectral limit and the diffraction limit (see section 2.1). Using the technique of Fourier transform spectroscopy, we extract the spectral information at each camera pixel. By simultaneously collecting a spectrally resolved broadband image, the signal-to-noise ratio is improved since no photon bandwidth is filtered. In addition, the spectrally resolved broadband information leads to an over-sampled diffraction pattern, which in principle improves the robustness of the phase retrieval algorithm [20].

3.1 Experimental setup

The conventional design for Fourier transform spectroscopy is a Michelson interferometer to delay between two identical beams. Given that there are no beam splitters in the spectral range of XUV or X-ray, we split a 800 nm beam, and use the two 800 nm beams to produce two time-delayed XUV high order harmonics beams. High order harmonic generation is a coherent process, and the copies of 800 nm beams generate two identical XUV light pulses during the interaction with a gas jet. The 800 nm beam comes from a 50 femtosecond, 16 mJ, Ti:sapphire laser at 100 Hz repetition rate. The energy we used in our experiment is 5 mJ per pulse at the entrance of our setup. The 800 nm beam is vertically linearly

polarized in the lab frame and has the pointing stability of a few microradians.

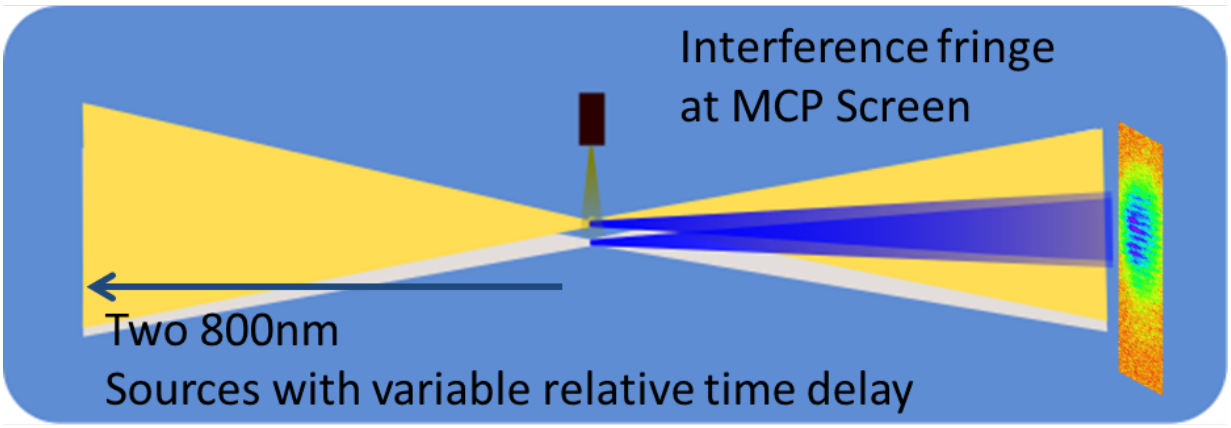

Figure 3.1: The setup for two source interference. The two high order harmonic sources are spatially separated at birth, and propagate to overlap in the far field. The two sources interfere in the far field and produce a two slit diffraction pattern for each harmonic.

Since high order harmonic generation is a highly nonlinear process, spatial overlap of the two 800 nm beams will cause strong perturbation of the generation process at the laser foci. To minimize this effect, we design our setup to spatially separate the two 800 nm light at the foci. After the high order harmonics are produced at the focus, they propagate and overlap in the far-field (see figure 3.1).

Fourier transform spectroscopy requires the collection of the autocorrelation trace. This means we have to delay two identical beams at better accuracy, and greater resolution in comparison to the wavelength. For example, the 21st harmonic has a wavelength of 38 nm. Using the Nyquist criterion, the delay step needs to be shorter than 19 nm, equivalent to 63 attoseconds in time delay. The stability needs to be better than 31 attoseconds to retrieve the spectrum.

To improve the delay stability between the two beams, we designed a novel setup with inline delay between the two 800 nm sources. An inline delay improves the delay stability by having vibration and air fluctuations affecting the two beam paths in a similar way. We use a pair of Wollaston prisms to achieve this purpose. A Wollaston prism consists of two orthogonal polarized birefringent calcite wedges (see figure 3.2). Each calcite wedge has two optical axes with different refractive indices. By moving the Wollaston prism in the perpendicular direction with respect to the incident beam, the beam passes through

longer distance inside one calcite wedge and shorter distance in the other. Due to the birefringence, the change in the medium thickness translates to the relative time delay between the incident beams of vertical and horizontal polarization.

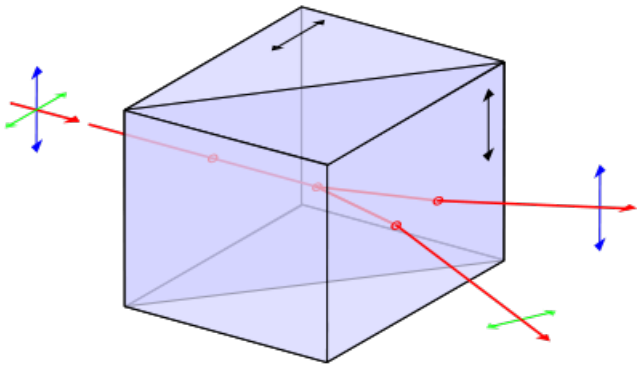

Figure 3.2: A Wollaston prism consists of two orthogonal polarized calcite wedges. It acts as a beam splitter by polarization [52].

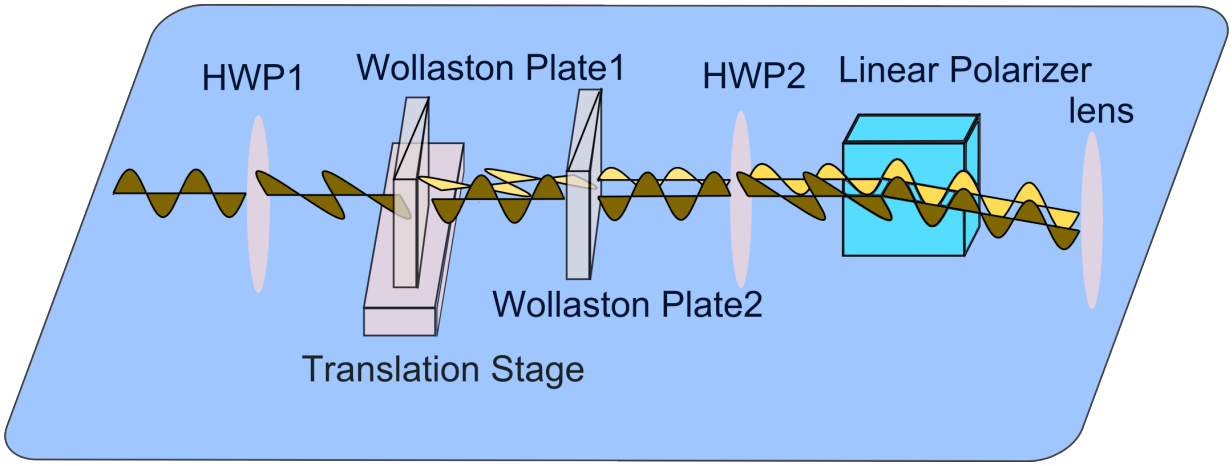

Figure 3.3: The experimental setup used for Fourier transform spectroscopy. The red and green wavy line represent the light path of two beams. All optical elements are mounted to an optical table

The experimental setup for the 800 nm can be seen in figure 3.3. The first half wave plate (HWP1) rotates the vertical polarization of the incident beam by 45 degree with respect to the vertical axis of the lab frame. The first Wollaston prism separates the input beam by vertical and horizontal polarization while directing the two beams into slightly different propagation directions. The first Wollaston plate is also used to control the delay

between the two beams via a translation stage (Newport MFA-PPD). The translation stage's minimum incremental motion is 100 nm, and the angle of calcite wedges inside the Wollaston prism are 5 degrees. This corresponds to 10 attoseconds of minimal incremental optical delay.

The second Wollaston prism sits on a mirror mount with two adjustable axes. It is used to control the relative angle between the two 800 nm beams. The angle between the two 800 nm beams can be tuned by changing the orientation of the Wollaston prism with respect to the incident beams. The difference in propagation directions results in two separate foci after passing the two beams through a focusing lens. The second wave plate (HWP2) rotates the polarization of the two beams from vertical and horizontal to +45 degree and -45 degree with respect to the vertical axis in the lab frame.

The linear polarizer after the wave plate reflects only the vertical component of the two beams. This creates two 800 nm beams with the same polarization and intensity. The reflected beams are used to generate XUV high order harmonics. The linear polarizer transmits the horizontal polarized beams which are used for optical phase referencing. We guide the horizontally polarized beams to the same table as our camera for recording XUV (see figure 3.4). This ensures similar propagating directions between XUV and the reference beams. We record the reference beams using an independent camera (model:WinCamD-UCD12). Ideally, we would like to use XUV for phase referencing since it has higher resolution, but we are currently limited by the space of our detector chamber. The method of phase referencing is described in section 3.2.

A lens of 40 cm focusing distance is used to focus the two vertically polarized 800 nm beams into a gas jet inside the vacuum chamber. We use a continuous gas jet of Argon with 1.8 bar backing pressure. A continuous gas jet is selected over a pulsed gas jet to ensure stability of the gas pressure during long data acquisition time.

The two 800 nm beams are spatially separated at the gas jet by 200 µm. This produces two identical but separate XUV pulse trains. The XUV beams propagate into a detector chamber and are focused onto an imaging sample. We focus the XUV using two focusing mirrors at grazing angles between 3 to 5 degrees (see figure 3.4). The two mirrors have 2.5 and 1.5 meter focusing distance at the normal incidence angle, respectively. The first mirror focuses XUV in the horizontal direction and the second mirror in the vertical direction. The focal spot size of the XUV beams is estimated to be on the order of 10 µm. We place the imaging sample of 20 µm few millimeters after the XUV focus to ensure even illumination

of both XUV beams. The imaging sample is mounted to a 3-dimensional translation stage inside the source chamber.

The XUV diffraction pattern is recorded 25 cm behind the sample. To image the XUV radiation, we use a combination of a micro-channel plate (MCP), a phosphor screen, and a high dynamic range CCD camera. The MCP consists of a two dimensional periodic array of miniature electron multipliers. The spatial resolution of the MCP is 10 µm which is determined by the spacing between electron multipliers. The XUV radiation induces a cascade of electrons that propagate through the MCP by the electric potential difference between the front and the back surface, which amplifies the original signal. The front surface of the MCP is grounded and the back surface is charged to 1.9 kV. The phosphor screen converts the electron cascade from the MCP into visible photons. The phosphor screen is charged to 3.9 kV. This creates 2kV of electric potential between the MCP and phosphor screen. Finally, a high dynamic range CCD camera (model: pco.1600) records the phosphor screen at 14 bit depth and 20 µm spatial resolution. The exposure time of the CCD camera is set to 400 ms for the two experiments described in chapter 4, and 2000 ms for Fourier transform holographic experiment in chapter 6.

The experimental setup of the vacuum system, imaging system, and optical elements can be seen in figure 3.5. All optical elements for the 800 nm beam are mounted to an optical table. We cover our optical table with aluminum walls to decrease the effect of air fluctuations. High order harmonics are generated inside the source chamber, and are focused onto a imaging sample inside the detector chamber.

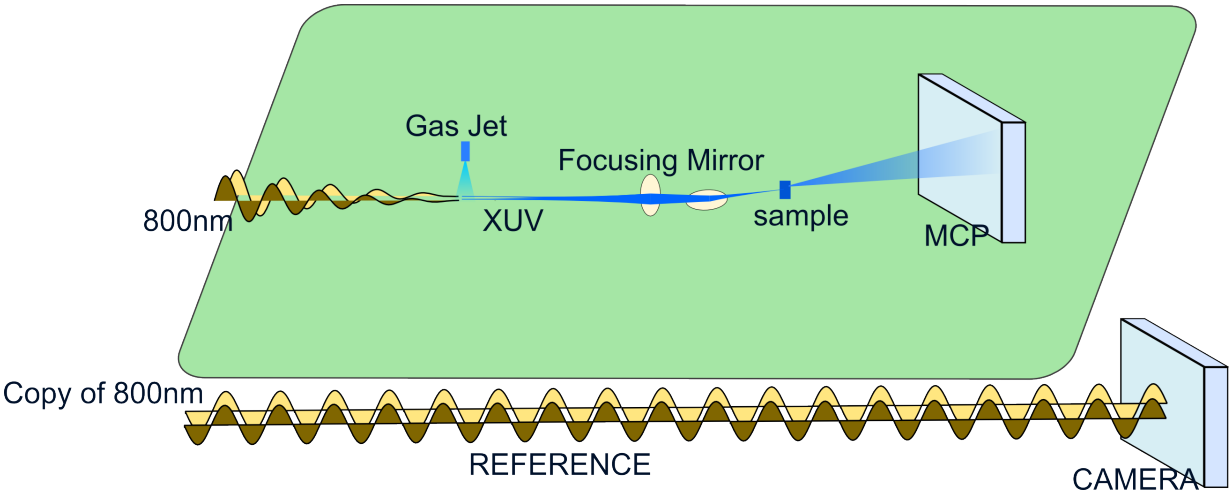

Figure 3.4: The experimental setup of XUV diffraction, and the phase referencing at 800 nm. We focus XUV light with two spherical mirrors. Each mirror is aligned at a grazing angle of few degrees. This improves the reflection coefficient at XUV but introduces astigmatism at the focus. Additional copies of 800 nm beams are used as the reference beams to calibrate the relative delay between the two XUV beams at the MCP screen. The method for phase referencing is described in section 3.2.

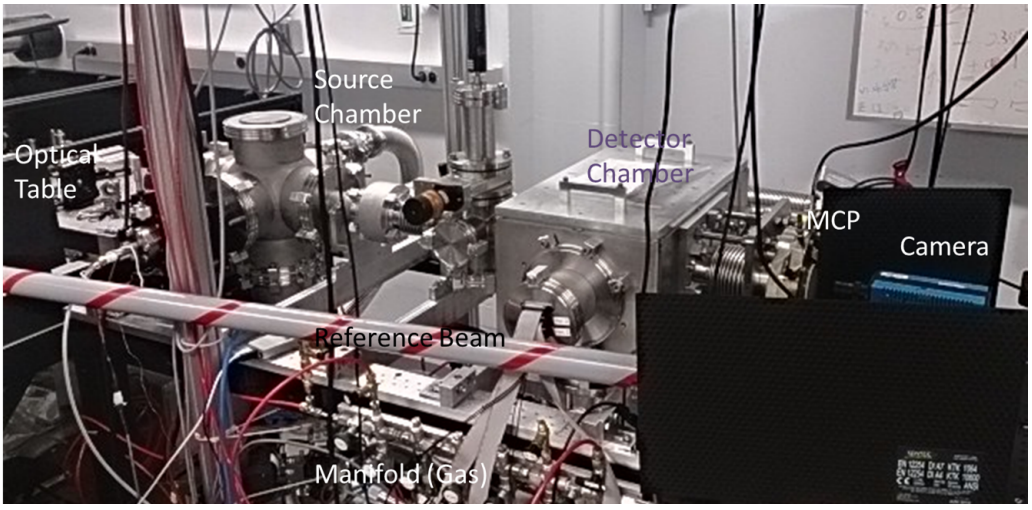

Figure 3.5: The relative positions of the optic table, source chamber, detector chamber, and camera. The delay stages are located on the optic table. The continuous gas jet and laser focus are inside the source chamber. Sample, focusing mirror, and the MCP are mounted inside the detector chamber. The reference beam shown in the picture is used for phase referencing.

3.2 Effective spectral resolution enhancement by phase referencing from optical interference

3.2.1 Introduction

In Fourier transform spectroscopy, the power spectrum is obtained from collecting the autocorrelation trace at a uniform time step. However, in experimental settings, the autocorrelation trace is collected at a non-uniform delay due to noise.

Consider the autocorrelation trace measured at a single camera pixel. The intensity at each delay position is the time integrated interference pattern of two identical beams. If the pointing of the two beams changes, the interference pattern and the relative time delay at the camera pixel also changes. If the pointing changes by 10 microradians per hour, the beam position would move by 50 µm at 5 meters away. For a standard XUV imaging device such as a MCP, which has a typical spatial resolution of 10 µm , the beam pointing instability could significantly change the image recorded. To retrieve the autocorrelation trace in the XUV domain, an optical delay step of a few nanometers is required. This demands not only the rigid construction of the optical elements, but also the decoupling of the experimental setup and the disturbances inside a lab environment such as heat, air fluctuations, and seismic noise.

It is even more challenging to retrieve an autocorrelation trace in the water window spanning wavelength from 2 nm to 5 nm. Sub-nanometer delay step cannot be achieved with the current commercial translation stages, and the delay stability of sub nanometer is extremely difficult to realize due to noise. Inline optical delay can improve the delay stability and resolution to sub-nanometer. But it uses variable thickness of a dispersive material, which lengthens the pulse duration and decreases the efficiency of high order harmonic generation. To generate a continuum spectrum, or to extend harmonics into the water window, a few optical cycle driving electric field is required.

In summary, the delay noise from beam pointing instability and the limitations of a translation stage, results in a non-uniform delay in the Fourier transform spectroscopy. In the conventional data retrieval procedure, we assume uniform delay at t_i and use discrete Fourier transformation to obtain the power spectrum:

$$\mathcal{F}_t(R_{auto}(x, y, t_i + \delta t_i)) = \mathcal{F}_t(R^*_{auto}(x, y, t_i)) = I(x, y, \omega), \tag{3.1}$$

where $R_{auto}(x, y, t_i+\delta t_i)$ is the distorted autocorrelation trace at non-uniform delay $t_i+\delta t_i$, $R^*_{auto}(x, y, t_i)$ uses the values of $R_{auto}(x, y, t_i+\delta t_i)$ at uniform delay, $I(x, y, \omega)$ is the retrieved power spectrum. When δt_i becomes significant compared to the quarter period of the light source, the quality of the retrieved power spectrum is undermined. In case where δt_i exceeds half period of the light sources, we can no longer retrieve the power spectrum based on the conventional Fourier transform spectroscopy.

3.2.2 Method

We overcome this technical difficulty using a novel approach named *phase referencing from optical interference*. We first produce two referencing beams from the original two sources by wavefront splitting. We can use a beam splitter for visible or UV sources, and a half mirror or diffraction grating for XUV, or X-ray sources. We use the original beam for conventional Fourier transform spectroscopy, and the referencing beams to extract the relative delay between the two sources. The retrieved optical delay is used to correct the non-uniform delay in Fourier transform spectroscopy.

We record the interference pattern of the two referencing beams as they overlap in the far field. For higher visibility of the interference pattern, we can either spectrally resolve or filter the broadband referencing beams with a diffraction grating or a narrow bandwidth mirror. The fringe pattern comes from the optical delay between the two sources. This includes the path difference and the time delay between the two sources. We use the spatial Fourier transformation of the interference pattern to extract the optical delay between the two sources. In practice, we record the phase of the most intense frequency. An ideal experimental setup for XUV, X-ray sources is shown in figure 3.6.

We perform phase referencing at every delay step of Fourier transform spectroscopy. In the lab environment, we would retrieve the non-uniform delay positions at $\tau = \tau_1, \tau_2, \tau_3, ...\tau_n$. We find the average delay step size τ_m by dividing $\tau_n - \tau_1$ by number of step n. We then linearly interpolate the autocorrelation function of the original beam $R_{auto}(y, \tau)$ to $R_{auto}(y, \tau_u)$, an autocorrelation function at uniform delay step, where $\tau_u = \tau_1, \tau_1+\tau_m, \tau_1 + 2\tau_m, ...\tau_n$. Figure 3.7 shows the flow chart for phase referencing.

To use this method, we need to spatially resolve the fringe spacing of the referencing beams at $\lambda L/d$. According to the Nyquist sampling criterion, each fringe must be sampled by more than 2 image pixels. The resolution of the retrieved phase is given by the fringe

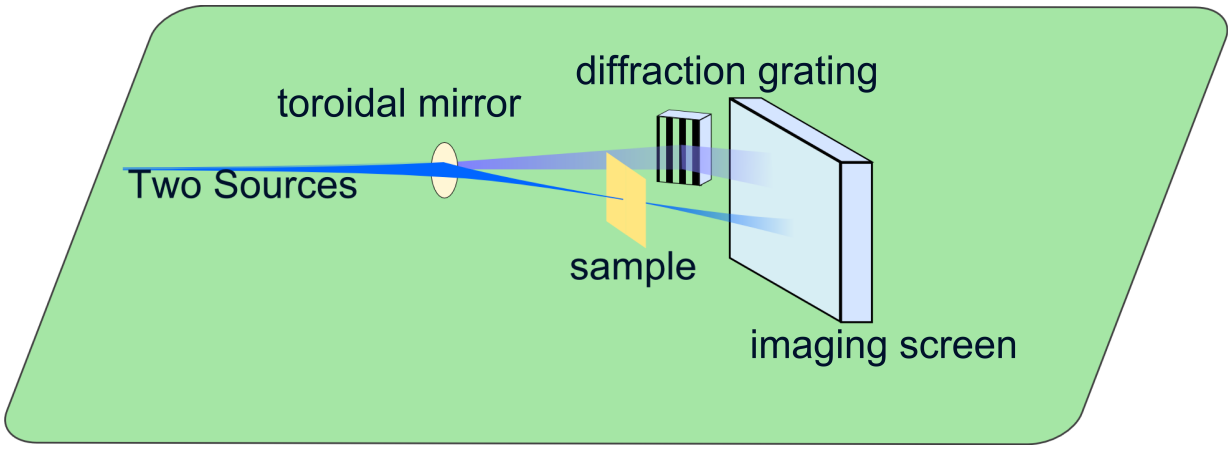

Figure 3.6: The ideal setup for phase referencing of XUV or X-ray sources. The position of the toroidal focusing mirror is adjusted to leak a small portion of the light that serves as the reference beam. The larger portion of the light can be utilized for broadband XUV or X-ray spectroscopy or microscopy. The reference beam contains interference fringes of two broadband sources. Using a diffraction grating, the broadband sources are dispersed into wavelengths propagating at different angles. This improves the visibility of the fringes at the imaging screen, and provides better accuracy for the phase referencing technique. In our imaging experiment shown in chapter 6, we use the setup in figure 3.4 due to lack of toroidal mirror and limited space inside our vacuum chamber.

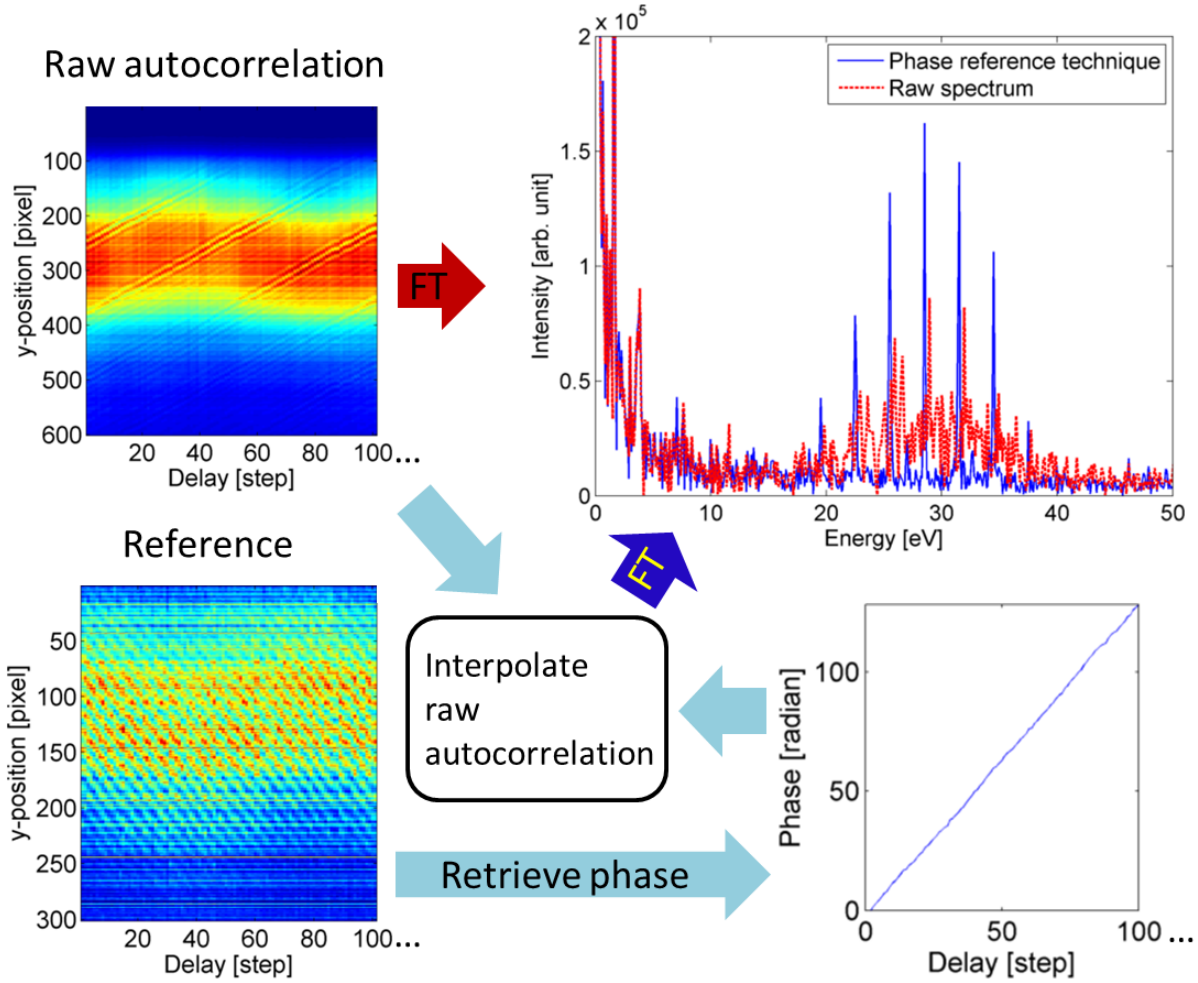

Figure 3.7: The procedure for phase referencing. The graph on the bottom left is the interference pattern of two narrow bandwidth XUV sources at different optical delays. Each vertical slice corresponds to the interference pattern at a particular delay. The phase retrieved can be seen in the bottom right figure. The graph on the top right shows the improvement given by the phase referencing. The plot shows the power spectrum of a high order harmonic source at the zero diffraction order. After phase referencing, the peaks becomes evenly spaced and show signature of harmonic peaks. The x-axis is calibrated by comparing the frequency ratio between the adjacent peaks, and the assumption that the harmonic peaks are at the odd multiple energy of an 800 nm photon. Energy is converted from harmonic numbers.

spacing divided by the number of camera pixels per fringe. Assuming an imaging system of 10 µm spatial resolution, and two 4 nm reference sources at 200 µm foci separation, the resolution of the retrieved phase is 1 nm at 2 m away, 0.2 nm at 10 m away.

Here we derive the procedure for retrieving the two source delay from the interference fringes. For simplicity, we consider two coherent monochromatic Gaussian beams with a wavelength of λ, spatial separation of d, and beam divergence of θ. As the two beams propagate in the same direction, they diverge and overlap in the imaging plane. The imaging plane has the coordinates (x,y) and is distance L away from the two sources (see figure 3.8).

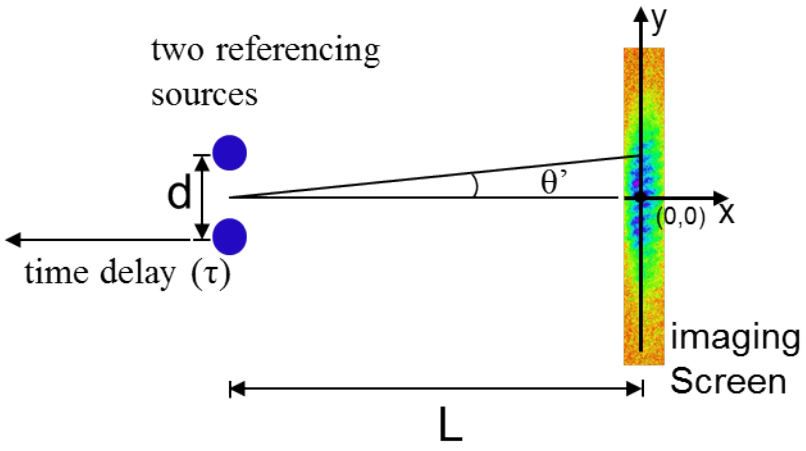

Figure 3.8: The setup of two source interference. L is the distance between the two sources and the imaging screen, y is the vertical axis on the imaging screen.

Using the far field approximation, the interference pattern at the imaging plane can be written as:

$$I(x,y,\tau) = cos^2(\frac{\pi}{\lambda}(dsin(\theta') + c\tau))e^{-2(y+x)^2/(\theta L/2)^2}. \tag{3.2}$$

If $y/L \ll 1$, then $sin(\theta') \approx \theta' = y/L$.

We substitute $sin(\theta') = y/L$ into equation 3.2:

$$I(x,y,\tau) = \frac{1}{2}[1 + cos(\frac{2\pi}{\lambda}(\frac{yd}{L} + c\tau))]e^{-2(y+x)^2/(\theta L/2)^2}. \tag{3.3}$$

To extract the relative delay between the two sources, we perform spatial Fourier trans-

formation along the y axis at $x = 0$:

$$\begin{aligned}
&\mathcal{F}_y[I(0, y, \tau)] = S(v, \tau) \\
&= [\delta(v)/2 + \delta(v - \frac{d}{\lambda L})e^{-\frac{i2\pi\tau c}{\lambda}}/4 + \delta(v + \frac{d}{\lambda L})e^{\frac{i2\pi\tau c}{\lambda}}/4] * e^{-2(\frac{v\theta L}{\pi})^2} \\
&= \frac{1}{2}e^{-(\frac{v\theta L}{\pi})^2/2} + \frac{1}{4}e^{-\frac{i2\pi\tau c}{\lambda}}e^{-2(v-\frac{d}{\lambda L})^2(\frac{\theta L}{\pi})^2} + \frac{1}{4}e^{\frac{i2\pi\tau c}{\lambda}}e^{-2(v+\frac{d}{\lambda L})(\frac{\theta L}{\pi})^2},
\end{aligned} \tag{3.4}$$

where $*$ is the symbol for convolution. Now we have the sum of three Gaussian functions centered at 0,$+\frac{d}{\lambda L}$,$-\frac{d}{\lambda L}$ respectively.

If $\theta d \gg \lambda$, only the second Gaussian function in 3.4 has significant value at $v = +\frac{d}{\lambda L}$. We take the phase in $S(+\frac{d}{\lambda L}, \tau)$ to retrieve τ:

$$Phase(S(\frac{d}{\lambda L}, \tau)) \approx Phase(e^{-\frac{i2\pi\tau c}{\lambda}}) = -\frac{2\pi\tau c}{\lambda}. \tag{3.5}$$

Since c and λ are constant, we have retrieved τ, the delay between the two sources.

Chapter 4

XUV Fourier transform spectroscopy

4.1 Fourier transform spectroscopy using first order diffraction

The first order diffraction from a diffraction grating contains dispersed wavelengths propagating at different angles. The incident light is spectrally resolved by spatial separation after the grating. While a diffraction grating spectrally resolves light in the spatial domain, Fourier transform spectroscopy does it in the temporal domain without affecting the spatial properties of the light. We combine the two techniques in one experiment and perform Fourier transform spectroscopy at the first diffraction order. This creates two independent copies of the spectral information with two different techniques. We use the spectral information obtained from the first order diffraction, an established method, to examine our spectral retrieval method: XUV Fourier transform spectroscopy with phase referencing. We are interested in whether our method can spectrally resolve light of narrow bandwidth, and how effective it can spectrally filter a selected wavelength.

We collect the first order diffraction of the two spatially overlapped broadband XUV beams. As shown in figure 4.1, the first order diffraction at the imaging screen contains well separated harmonic peaks, which is characteristic of high order harmonic sources. The higher order harmonic corresponds to shorter wavelength, and a narrower interference fringe between the two sources.

As the relative time delay between the two sources is varied, we record the intensity at each pixel as a function of the time delay. The intensity at different delays are used as the

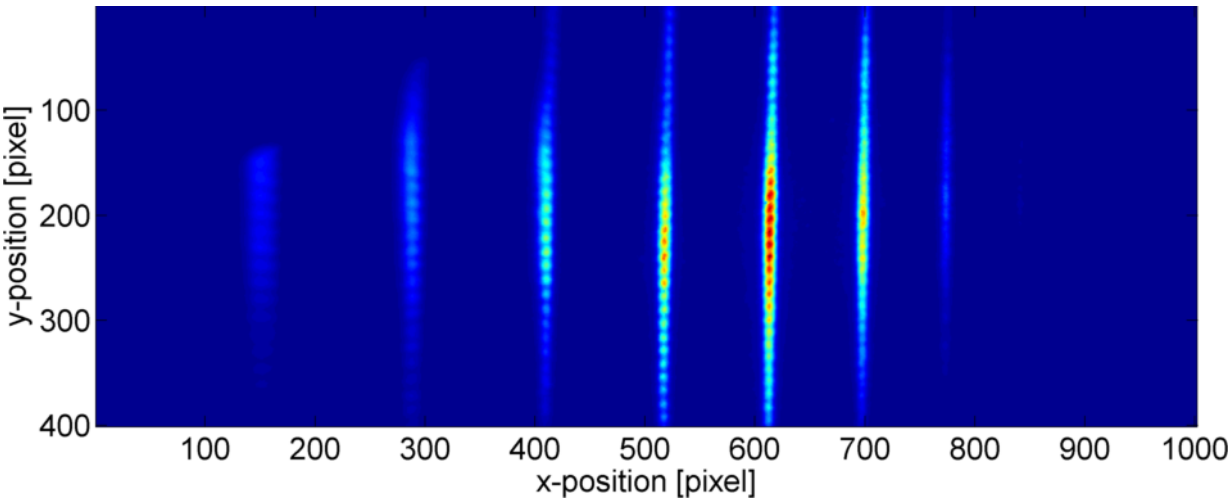

Figure 4.1: The first order diffraction of a broad bandwidth high order harmonic source.

autocorrelation trace at each pixel. Using the experimental setup shown in section 4.1, we scan the two sources at 10 attoseconds per step over a total delay of 17 femtoseconds.

Figure 4.2 shows the autocorrelation trace collected at a single pixel. We show the autocorrelation trace before and after performing our phase referencing method (see section 3.2). Here, we use the interference fringe at x=518 as our referencing beam. As shown in figure 4.2, the phase referencing technique interpolates the signal from non-uniform to uniform delay, and smooths the autocorrelation trace. We then take the Fourier transformation of the autocorrelation trace, which gives us the power spectrum shown in figure 4.3. The harmonic signal after phase referencing is stronger by a factor of 3 and narrower by a factor of 27 compared to before.

We apply the same approach to every camera pixel. In principle, this would give us another way to spectrally resolve the first order diffraction. By spectrally selecting 21st, 23rd, and 25th harmonic peaks with a frequency window of 0.3 eV bandwidth, we plot the spectrally filtered images without phase referencing in figure 4.4, and with phase referencing in figure 4.5. The figure 4.5 shows that after phase referencing, we can spectrally distinguish adjacent harmonics with more than one order of magnitude of dynamic range. Without phase referencing, the same dynamic range drops to 2, as shown in figure 4.4. The order of the harmonic is obtained by comparing the frequency ratio between the retrieved harmonic peaks, and the ratio of odd integers.

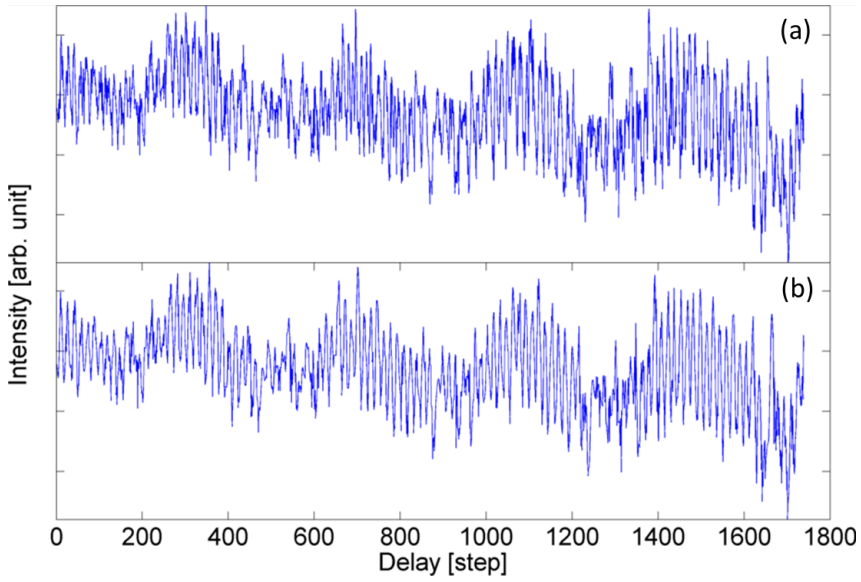

Figure 4.2: The autocorrelation trace at a single pixel before phase referencing (a), and after phase referencing (b). Both traces were collected at a single pixel at position [614,200] of figure 4.1.We use the vertical slice at x=518 for phase referencing.

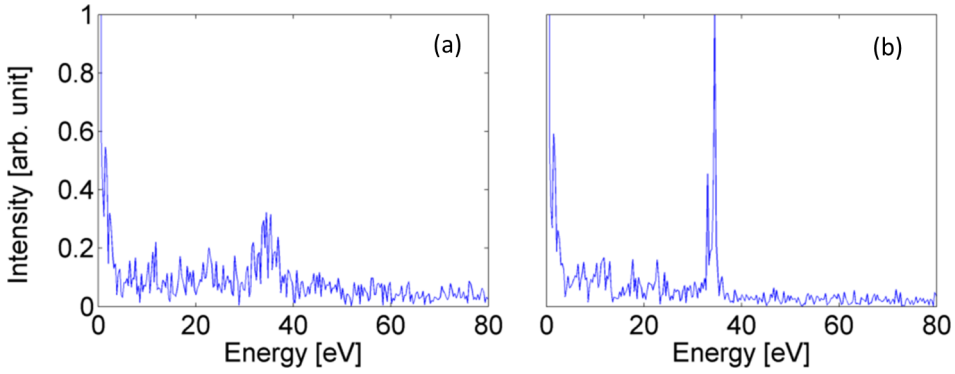

Figure 4.3: The retrieved power spectrum of a single pixel before phase referencing(a), and after phase referencing(b). Both plots use the same intensity scale which is normalized to the harmonic peak in (b). We take the average from 60 to 80 eV to be our baseline. The full width of half maximum of the harmonic peak is 8 eV on the left, and 0.3 eV on the right.

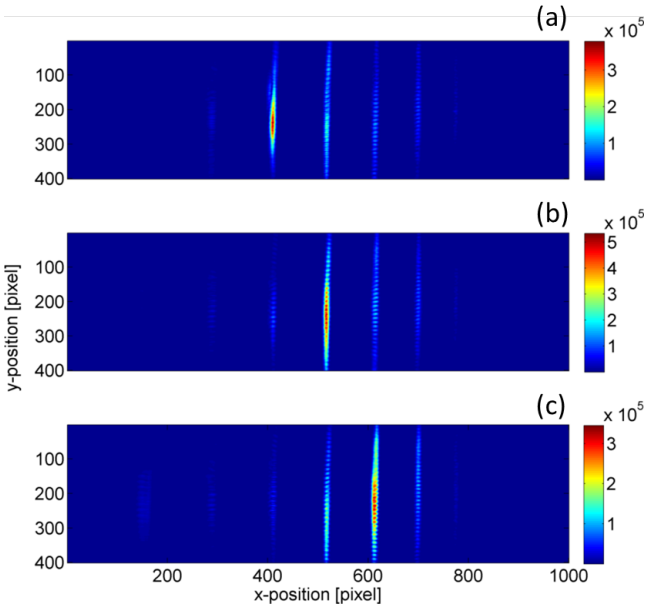

Figure 4.4: The spectrally filtered image without using the phase referencing technique. a, b and c each present the spectrally filtered image at 21st, 23rd and 25th harmonic with 0.3eV bandwidth, respectively. Despite spectral filtering only one harmonic, other harmonics remain visible on the linear intensity scale.

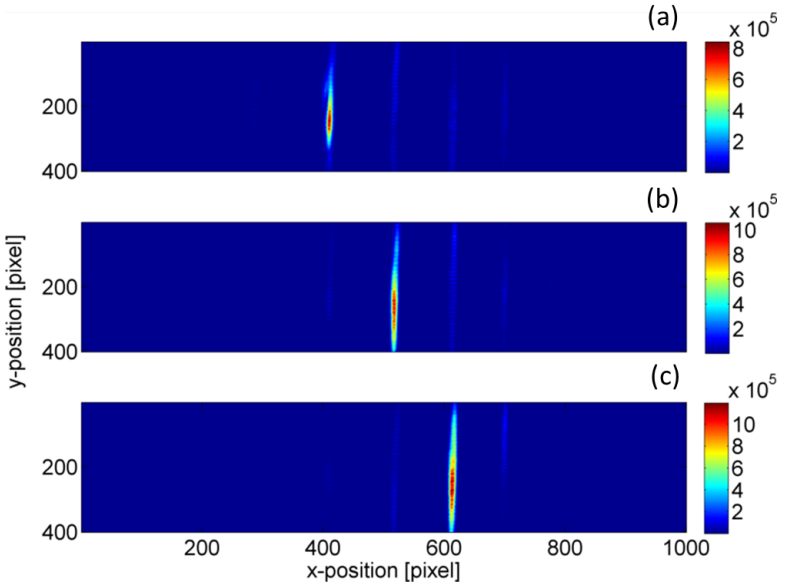

Figure 4.5: The spectrally filtered image after using phase referencing technique. a, b and c each present the spectrally filtered image at 21st, 23rd and 25th harmonic with 0.3eV bandwidth, respectively. Only the spectrally filtered harmonics have clear visibility on the linear intensity scale.

4.2 Fourier transform spectroscopy using zero order diffraction

Now we examine the Fourier transform spectroscopy at the zero-order diffraction of a diffraction grating. Zero-order diffraction is similar to the light reflected off a mirror, which contains non-dispersed broadband XUV. We use zero-order diffraction to check whether we can spectrally resolve light of a broadband source.

Figure 4.6 shows the retrieved raw data along a vertical slice. The data is taken at 180 µm foci separation of the 800 nm. By performing Fourier transformation in the time domain, we retrieve the power spectrum shown in figure 4.7. In figure 4.7, we presents the power spectrum at three different single camera pixels. The spectral peaks are well distinguished from the background noise and are evenly spaced as harmonics. We used phase referencing for the retrieved power spectrum. This demonstrates that we can retrieve the full power spectrum at every single camera pixel. The delay between the two sources is scanned with 30 attoseconds step size over a total delay of 39 femtoseconds.

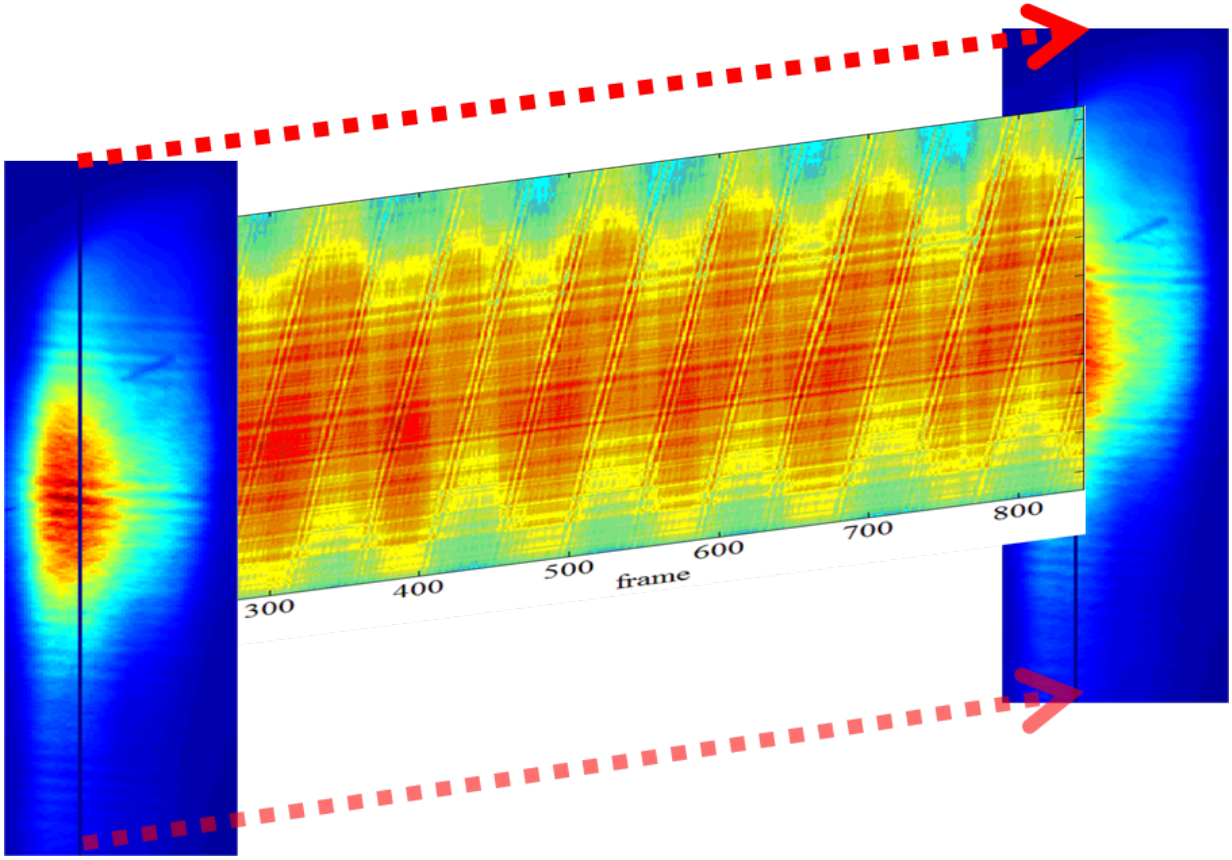

Figure 4.6: The figure in the middle follows the evolution of the interference pattern during a scan. The horizontal axis corresponds to the delay step between the two sources. Each vertical slice in the middle figure corresponds to a vertical line on the imaging screen as indicated by the blue line in the left/right figure. The left and right figures are the two interference patterns recorded at the two dimensional imaging screen at the beginning and the end of the delay, respectively. As the relative time delay between the two sources is varied, the fringes move in the y(vertical) direction.

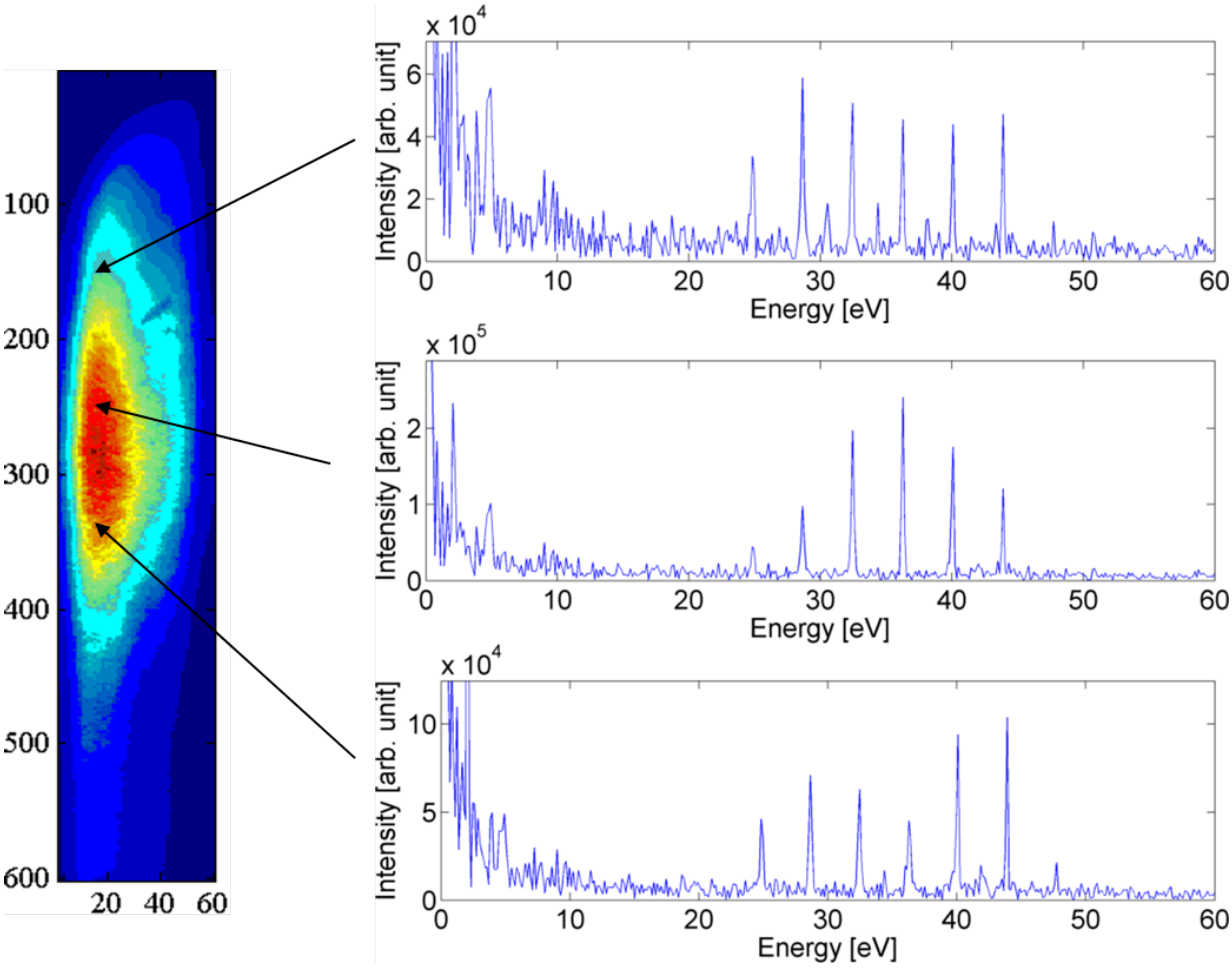

Figure 4.7: The graph on the left is the frequency integrated high order harmonic source. The asymmetric beam profile of the zero-order diffraction is due to the curvature of the employed grating. The three plots on the right show the retrieved power spectrum at each single camera pixel.

4.3 Spatial modulation at the focus

Ideally, we want the two sources to be identical and independent of each other, just like the common Fourier transform spectroscopy. However, high order harmonic generation is a highly nonlinear process. As the spatial tails of the two 800 nm sources interfere, the wave front at the laser focus is perturbed and this leads to a change of the far field pattern. This process is called spatial modulation [53].

As shown in figure 4.8, an effect of spatial modulation is the intensity modulation at the periodicity of 800 nm, which is equivalent to 2.7 femtoseconds in time delay. This gives a intensity envelope of 800 nm period for each of the harmonics. In the Fourier domain, this creates additional side peaks that do not exist in the actual spectrum. The side peaks are at one 800 nm photon energy away from the odd harmonics, making them appear as even harmonics.

Assume we have the autocorrelation trace of a monochromatic high order harmonic:

$$I(\tau) = cos(n\omega\tau) + 1, \tag{4.1}$$

where τ is the delay of the autocorrelation function. If it follows intensity modulation of the fundamental frequency ω, we have:

$$I(\tau) = (cos(n\omega\tau) + 1) \times (Acos(\omega\tau) + 1), \tag{4.2}$$

where A is the modulation amplitude. Now the power spectrum we get is the Fourier transformation of the autocorrelation function:

$$\begin{aligned}
&\mathcal{F}_t[I(\tau)] = \mathcal{F}_t[(cos(n\omega\tau) + 1)(cos(\omega\tau) + 1/A)A] \\
&= (\delta(\omega' - n\omega) + \delta(\omega' + n\omega) + \delta(\omega')) * (\delta(\omega' - \omega) + \delta(\omega' + \omega) + \delta(\omega')/A)A \\
&= \delta(\omega') + [(\delta(\omega' - n\omega)] + \delta(\omega' + n\omega)] + [\delta(\omega' - \omega) + \delta(\omega' + \omega)]A + ... \\
&[\delta(\omega' - (n-1)\omega) + \delta(\omega' - (n+1)\omega) + \delta(\omega' + (n+1)\omega) + \delta(\omega' + (n-1)\omega)]A.
\end{aligned} \tag{4.3}$$

The last 4 terms show the retrieved frequency sideband at fundamental frequency away from the high order harmonic. This explains the even harmonic we see in the retrieved power spectrum, as shown in figure 4.9.

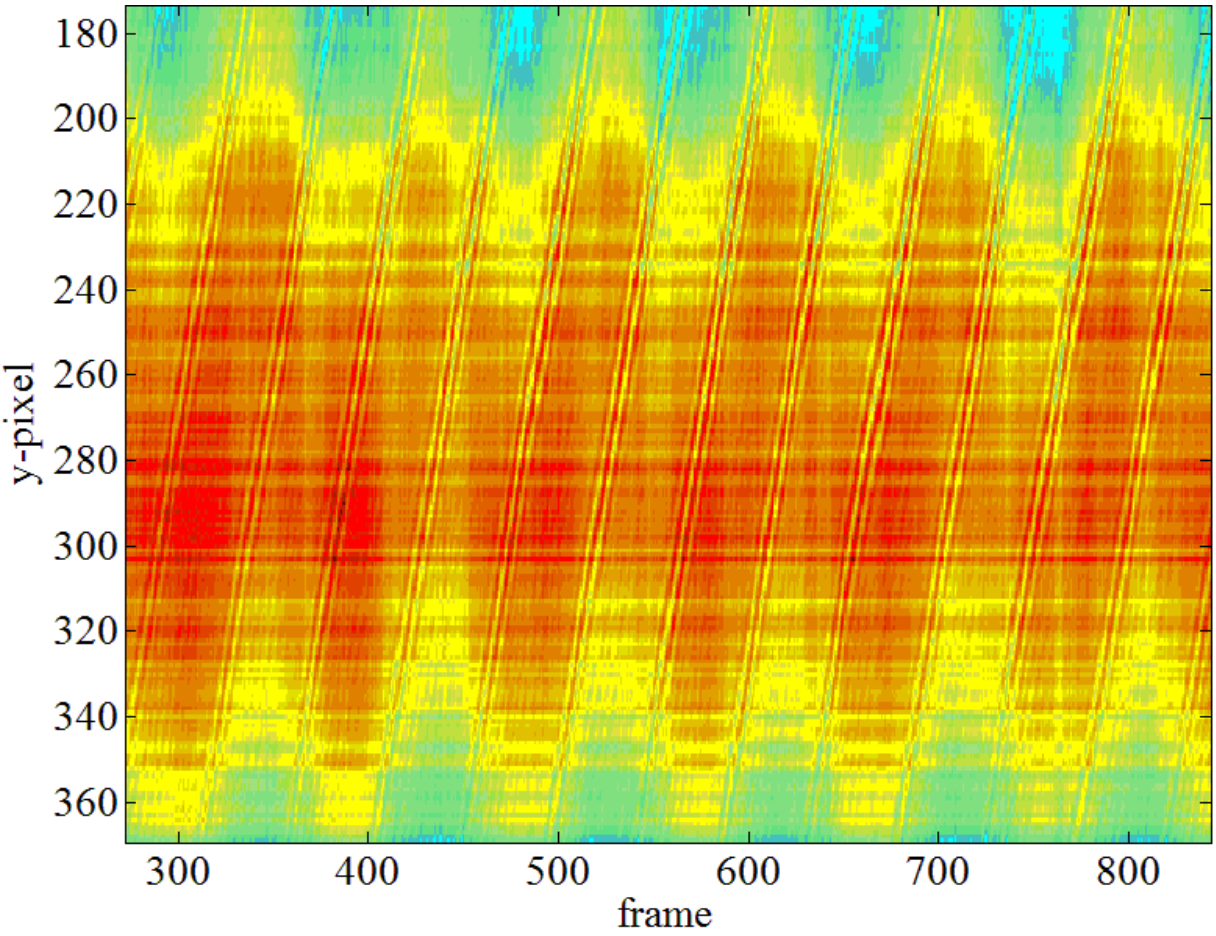

Figure 4.8: The horizontal axis corresponds to the delay step between the two sources. As the relative time delay between the two sources is varied, the fringes move in the y(vertical) direction.

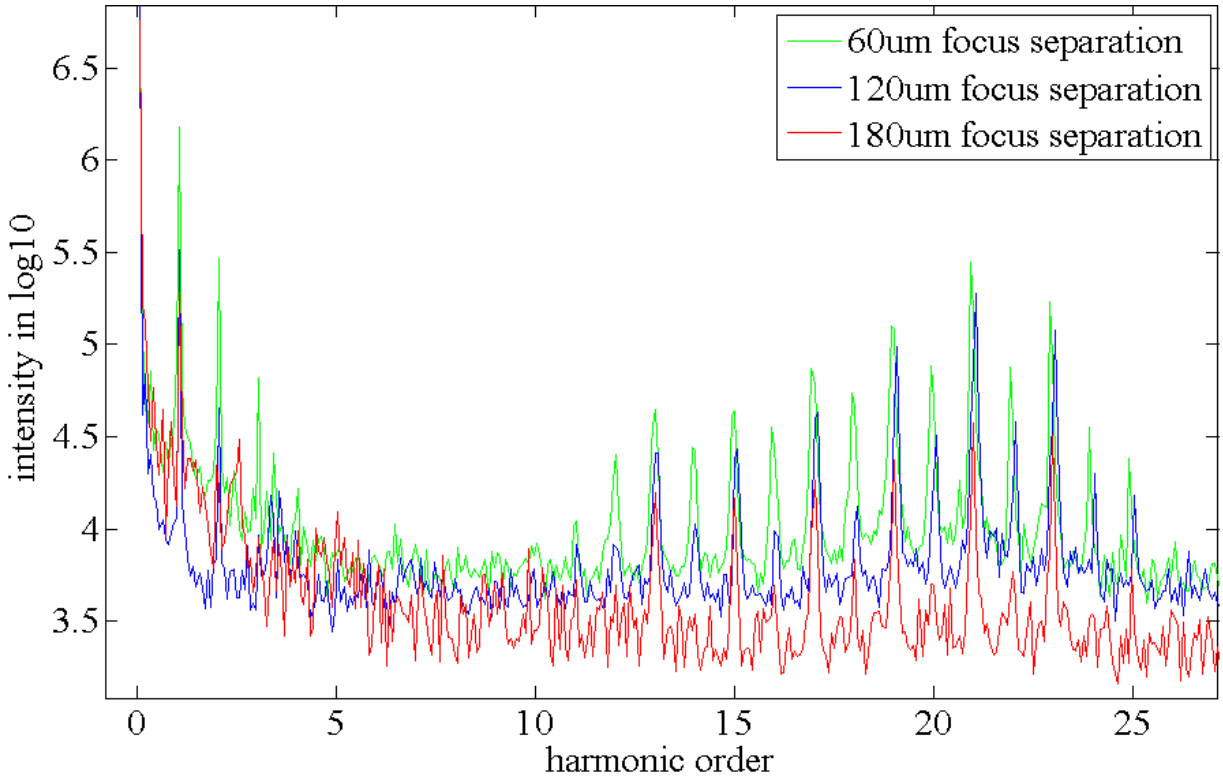

Figure 4.9: The power spectrum obtained from Fourier transform spectroscopy at different foci separations of the two 800 nm beams at the gas jet. At 60 µm separation, both odd and even harmonics are at similar amplitude. However, as the foci separation increases to 180 µm, the even harmonic peaks can no longer be distinguished from the background noise.

4.4 The effect of non-uniform delay on Fourier transform spectroscopy

Here we simulate the effect of non-uniform delay on the Fourier transform spectroscopy using a simulated power spectrum of HHG (see figure 2.12). Using inverse Fourier transformation, we convert the power spectrum to an autocorrelation trace. The time delay in the autocorrelation trace is at 30 attosecond step size over a total delay of 30 femtoseconds, which is similar to our experimental setting for the XUV hyperspectral coherent diffractive imaging. We interpolate the autocorrelation trace to the non-uniform step size. The deviation from the uniform step size is given by a random Gaussian distribution with standard deviation of σ_t. The interpolated autocorrelation trace is then treated as a uniform delay, and converted back to a distorted power spectrum by Fourier transformation. The result of our simulation is shown in figure 4.10. We examine the effect of non-uniform delay at three different σ_t of 5, 10, 20 attoseconds, respectively. As the delay noise increases, the ability to resolve the harmonic frequencies is quickly reduced. When σ_t of the delay step reaches 20 attoseconds, the retrieved harmonic peaks at 13th and 25th are no longer distinguishable from the background noise.

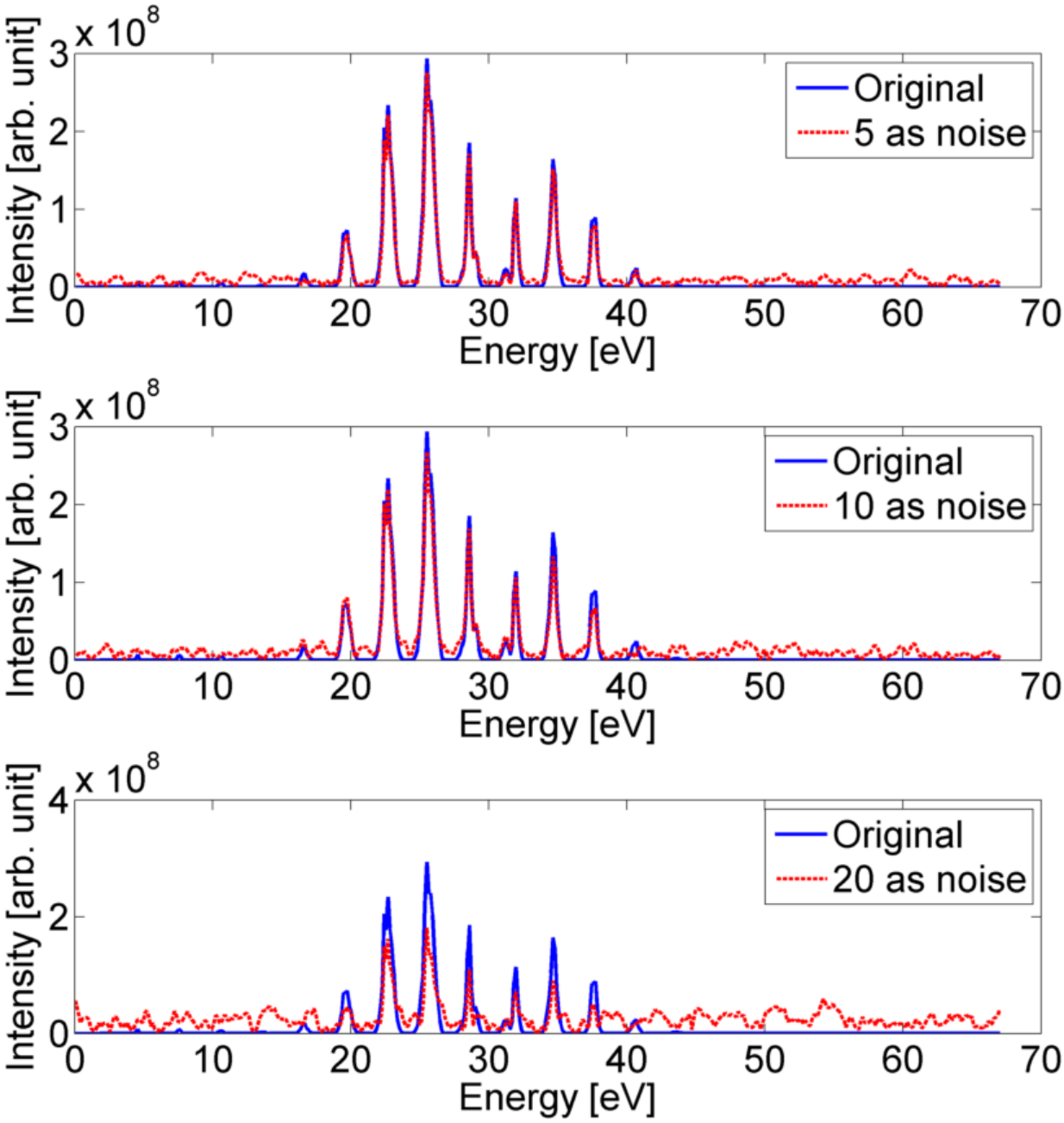

Figure 4.10: Simulated power spectrum retrieved from Fourier transform spectroscopy with non-uniform delay. The top, middle, and bottom plot shows the increasing distortion of the retrieved power spectrum as the delay noise increases from 5 to 20 attoseconds.

Chapter 5

Simulation of noise effect on image retrieval

Here, we perform computer simulations to examine our method of image retrieval and the effect of noise on the quality of image reconstruction routines. There are two types of noise: intensity fluctuations, and time errors in the relative delay between the two sources.

For the effect of intensity noise, we apply Gaussian noise to the far field diffraction intensity, and we examine the robustness of HIO, OSS, RAAR, and Fourier transform holography under different level of noises.

$$I^*(x, y, \omega) = I(x, y, \omega) + \Delta I(x, y, \omega), \tag{5.1}$$

where $I^*(x, y, \omega)$ is the noisy far-field diffraction pattern, $I(x, y, \omega)$ is the noise free far-field diffraction pattern, $\Delta I(x, y, \omega)$ is a random variable that follows Gaussian distribution with zero mean.

In addition, we study how a non-uniform delay from Fourier transform spectroscopy reduces the effective spectral resolution and distorts the spectrally resolved diffraction pattern. We use OSS and Fourier transform holography to study the quality of image retrieval under the effect of non-uniform delay.

$$\mathcal{F}_t(R^*_{auto}(x, y, t_i)) = \mathcal{F}_t(R_{auto}(x, y, t_i + \delta t_i)) = I(x, y, \omega), \tag{5.2}$$

where $\mathcal{F}_t$ is a 1D fourier transform operator along the time domain, $R_{auto}(x, y, t_i)$ is the au-

tocorrelation function retrieved in the far-field at uniform sampling point t_i=$[0, t_s, 2t_s, \dots]$, R^*_{auto} is the distorted auto correlation function at non-uniform delay, δt_i is a Gaussian random variable with zero mean and standard deviation of σ_t.

5.1 Sample

To check the validity of our method, we have simulated the far field diffraction pattern of a sample and looked at the result of the retrieval. As shown in figure 5.1, we use the image of an actual sample and convert it to a bit map. The sample used in the simulation is similar to our experiment shown in chapter 6, consists of a slanted 'F' and a reference slit.

Figure 5.1: The sample used in the simulation is a bit map converted from a real sample. The picture on the left is taken from a light microscope. The length of the reference slit is on the order of 20 µm. The picture on the right shows the converted bit map. We use the picture on the right as our diffraction sample and the true object space for all simulation in this section.

As shown in figure 5.2, the far-field diffraction of the sample is generated by the absolute squared spatial Fourier transformation of the bit map.

5.2 Image retrieval with noiseless data

Here we examine our retrieval method with noiseless data. Using the far field diffraction intensity simulated in the previous section, we implement both Fourier transform holography and the HIO algorithm. The retrieved image from Fourier transform holography is shown in 5.3, and the retrieved image from HIO algorithm is shown in 5.4. Both methods

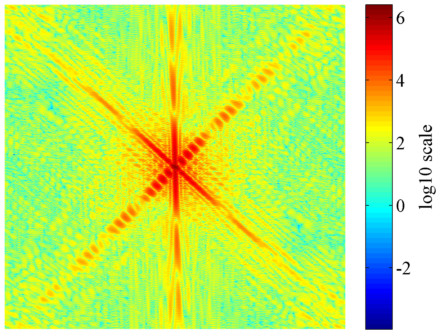

Figure 5.2: Simulated far field diffraction pattern of the sample. The far field pattern is generated from 2 dimensional Fast Fourier transformation of the known sample.

give a robust object reconstruction. HIO algorithm is shown to produce less artifacts compared to Fourier transform holography. Here we chose the initial phase for HIO algorithm to be random. We can also improve the convergence rate of the HIO algorithm using initial phase obtained from Fourier transform holography. The simulated result is shown in appendix B.

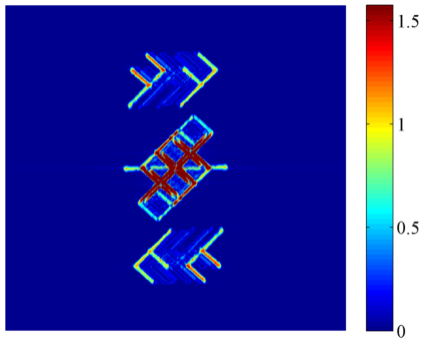

Figure 5.3: Using Fourier transform holography, the diffraction sample can be directly retrieved. The method gives unambiguous reconstruction of the object 'F'. The method of Fourier transform holography is described in section 2.4.

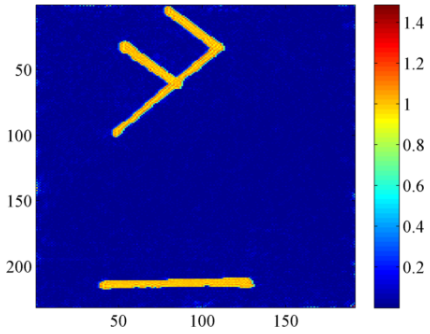

Figure 5.4: Using hybrid input output routine, we retrieve the object image.

5.3 Phase retrieval routines using noisy data

5.3.1 Noise effect from intensity fluctuation

Here we study how noise affects the iterative phase retrieval algorithms. To show the effect of the intensity noise on the HIO phase retrieval algorithm, we add Gaussian noise with standard deviation of 5%, 10%, 30%, and 50% of the far field diffraction intensity. It can be shown in figure 5.5 that the additional intensity noise decreases the quality of the reconstruction at two different phases. From 5% to 30% noise level, the HIO algorithm gives an accurate structure of the imaging sample but the contrast of the retrieved images decreases with increasing noise. When the noise level reaches 50% of the diffraction intensity, the HIO algorithm no longer gives robust image reconstruction, and the relative position between the reference slit and structure of F becomes destabilized at different phase retrieval iterations. In this study, we chose the free parameter B to be 0.9, similar to the optimal values shown in other papers [38, 54].

To verify the effect of the intensity noise is not characteristic to the HIO algorithm at a singular free parameter value, we perform phase reconstruction at 50% noise level using three different popular phase retrival algorithm: HIO, RAAR, OSS. For each algorithm, we use free parameter B at 0.6,0.7,0.9, respectively. We run each phase retrieval routine for up to 300 iterations. Figure 5.6 shows none of the phase retrieval algorithms gives a robust image reconstruction at the 50% noise level.

As a contrast to phase retrieval algorithms, Fourier transform holography is robust against high intensity noise levels. As shown in figure 5.7, we can see a clear letter 'F' up to 200% noise level. This is a great improvement in comparison with phase retrieval by

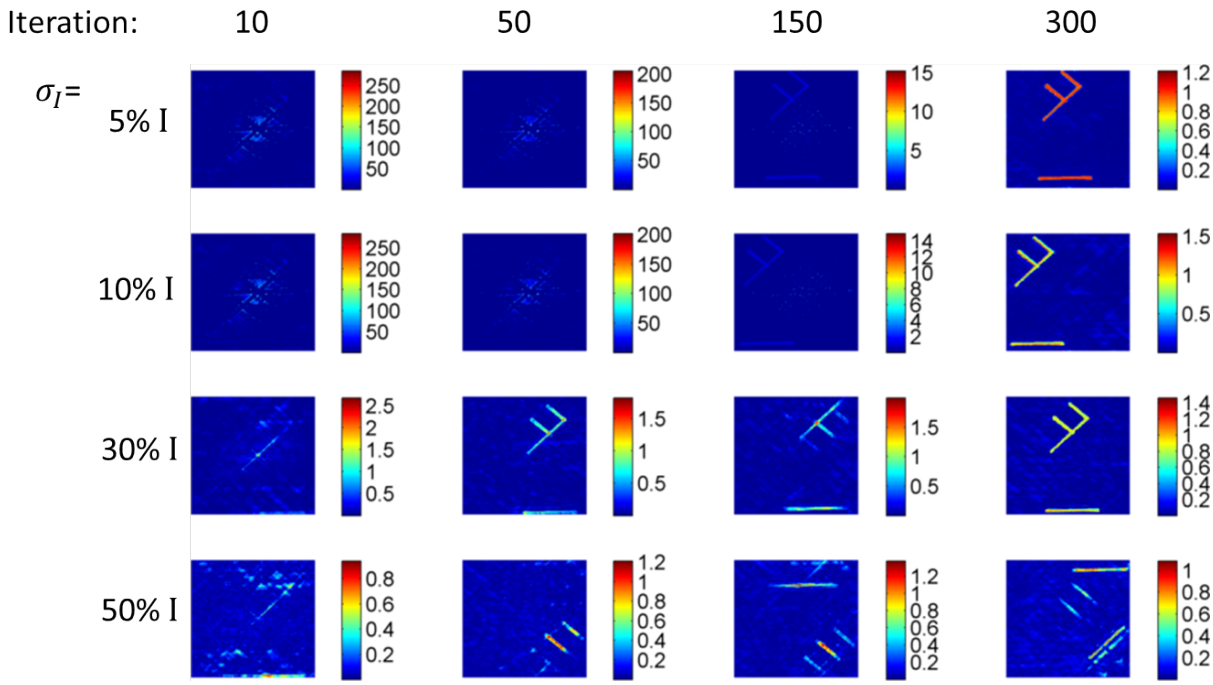

Figure 5.5: The four rows are the image retrieved from noisy diffraction pattern at noise level of $5\%, 10\%, 30\%, 50\%$, respectively. At each noise level, we plot the retrieved image from the 10th iteration to the 300th iteration of the phase retrieval algorithm.

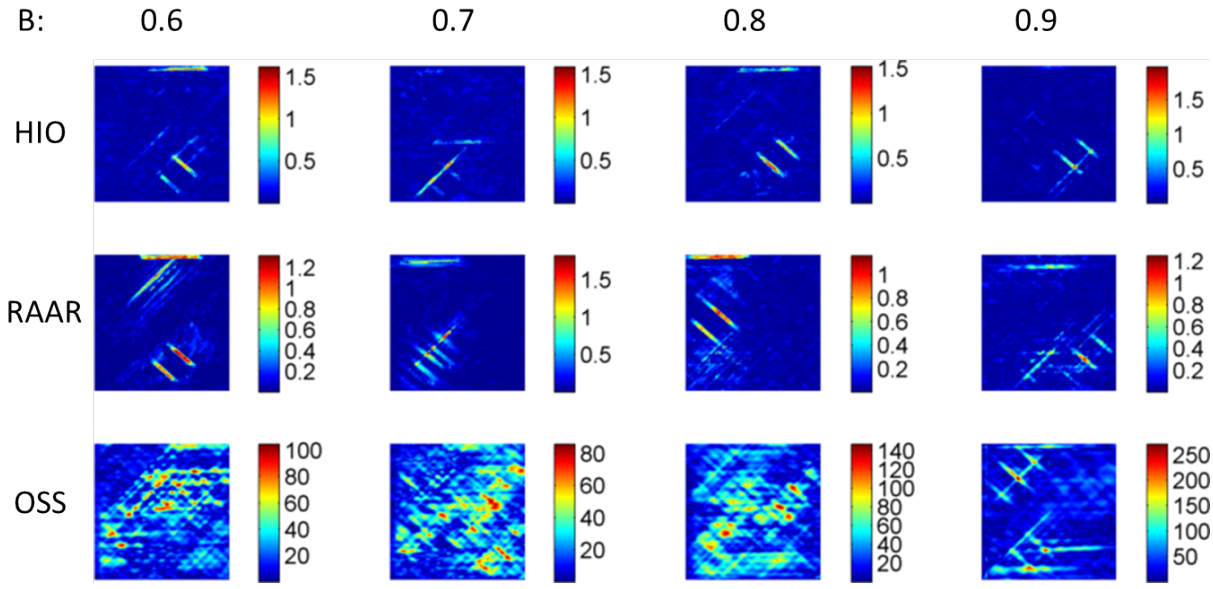

Figure 5.6: The retrieved images using three existing popular phase retrieval algorithms at 50 % noise level.

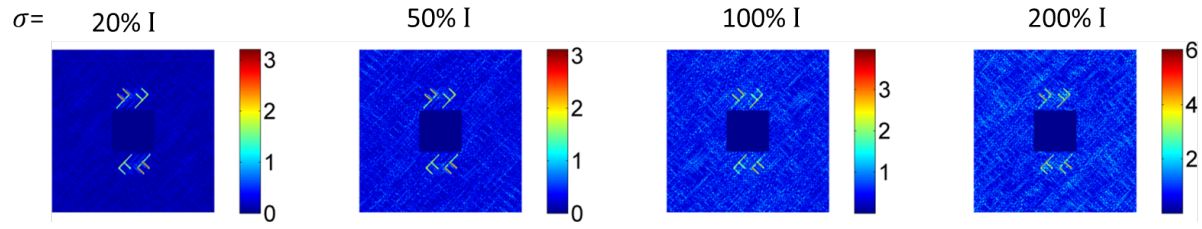

Figure 5.7: Rhe retrieved images using Fourier transform holography at different level of Gaussian noise.

iteration, where OSS, HIO, RAAR all failed at 50 % intensity noise level. Since intensity noise is random in time, it is disproportional to the total exposure time and photon intensity in the coherent diffraction imaging experiments. Consequently, Fourier transform holography can be used for robust image reconstruction with less photon flux required than phase retrieval algorithms.

5.3.2 Noise effect from non-uniform delay

To study the effect of non-uniform delay on the image reconstruction, we simulate a spectrally resolved diffraction pattern from 2 to 45 eV using the far field approximation. In the far field approximation, the diffraction patterns are the same for all wavelength but their size scales with the wavelength. Due to this wavelength dependence of the diffraction pattern, the spectrum at each single pixel is different from the source. Our simulated far field diffraction data contains three dimensional information: the two dimensional intensity pattern at the imaging screen, and the one dimensional power spectrum at each image pixel. We use inverse Fourier transformation along the frequency domain, and collect the autocorrelation function at each pixel. The power spectrum of the source is the simulated spectrum from subsection 2.5.2. We introduce non-uniform delays by adding Gaussian noise to the uniform delay of the autocorrelation function. We then linearly interpolate the autocorrelation function to the non-uniform delays. Finally, we use the values of the new autocorrelation with uniform delays, and Fourier transform it into a distorted power spectrum with the influence of delay noise.

We simulate spectrally filtered diffraction patterns from both uniform and non-uniform delays. Figure 5.8 shows the retrieved far-field diffraction pattern at the 13th, 21st, and 27th harmonics of 800 nm. The step of the uniform delay is at 30 attoseconds, similar to

the delay step used in the experiment shown in chapter 6. We use three different levels of delay noise at 5, 20, 30 attoseconds standard deviation, respectively. For comparison, we plot the ratio of the diffraction intensity after and before adding the delay noise. As shown in figure 5.8, the ratio is spectrally and spatially dependent, and increases at higher order harmonics or higher delay noise.

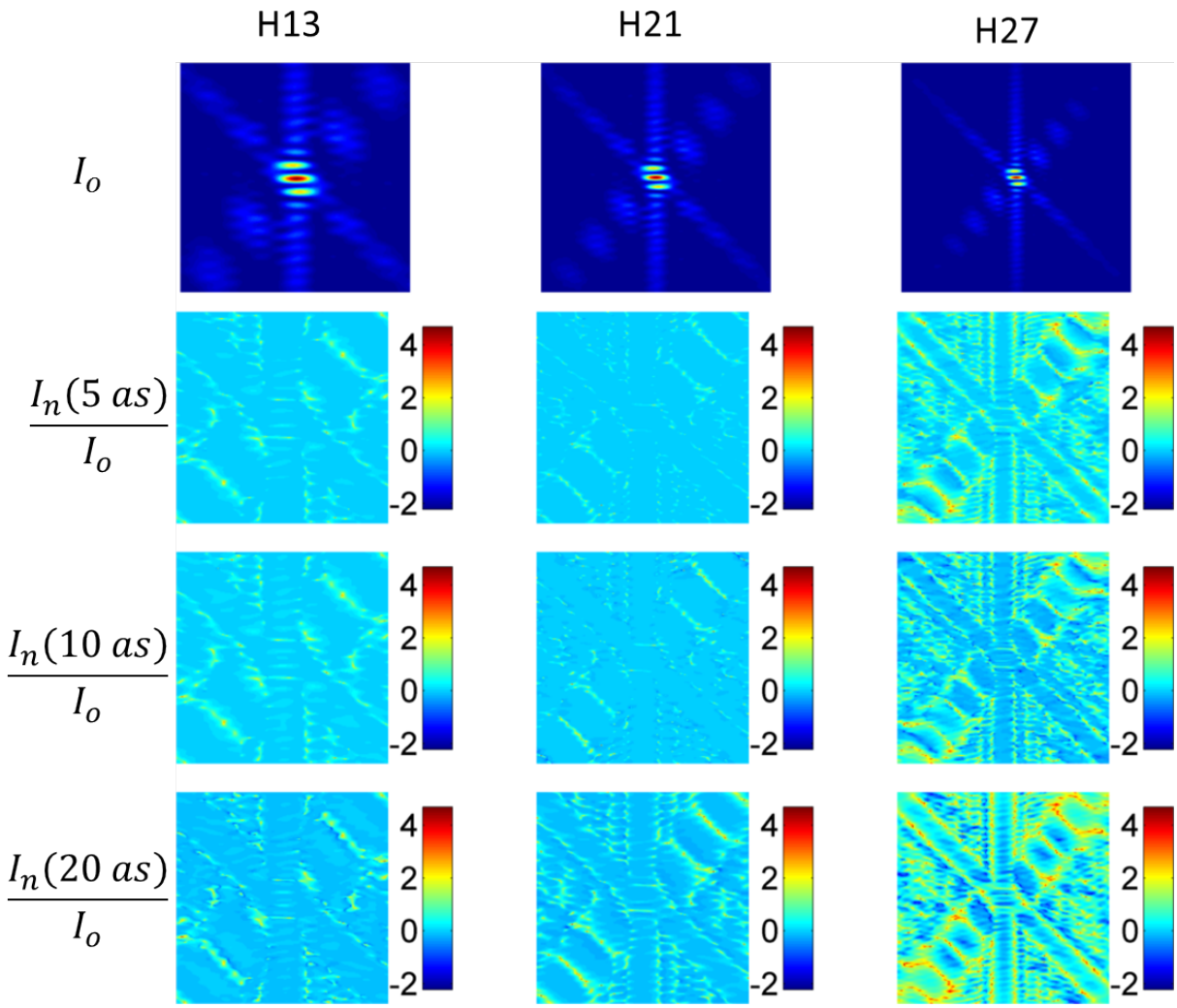

Figure 5.8: The top three plots show the noise free diffraction pattern. The bottom graphs show the ratio of intensity between the retrieved diffraction pattern from non uniform delay and uniform delay. The standard deviation of the assigned noise are at 5, 10, and 20 attoseconds.

Figure 5.9 shows the retrieved image using Fourier transform holography method with

non-uniform delay. We use the same data set from figure 5.8, and plot only the retrieved images. It is shown that the quality of the reconstructed image decreases quickly with the increasing harmonic number. While the retrieved 'F' pattern at 20 attosecond delay noise is barely visible at 27th harmonic, there is no ambiguity of the retrieved pattern at the 21st harmonic. This agrees qualitatively with our simulation on the effect of non-uniform delay on Fourier transform specstroscopy (see figure 4.10).

In addition, we simulate the effect of non-uniform delay on the iterative phase retrieval using OSS algorithm (see figure 5.10). We use the spectrally filtered 21st harmonic, and plot the reconstructed image after 300 iterations at 0, 5 ,20, 30 attosecond delay noise respectively. For unambiguous image retrieval, the delay noise should be similar to or less than 5 attoseconds. It shows the phase iterative algorithm is less robust against non-uniform delay in comparison to the Fourier transform holography, as shown in figure 5.9.

In theory, the 21st harmonic can be resolved at a maximum 63 attosecond uniform-delay, which is one order of magnitude higher than the maximum delay noise allowed for unambiguous image retrieval using either the phase retrieval algorithm or Fourier transform holography.

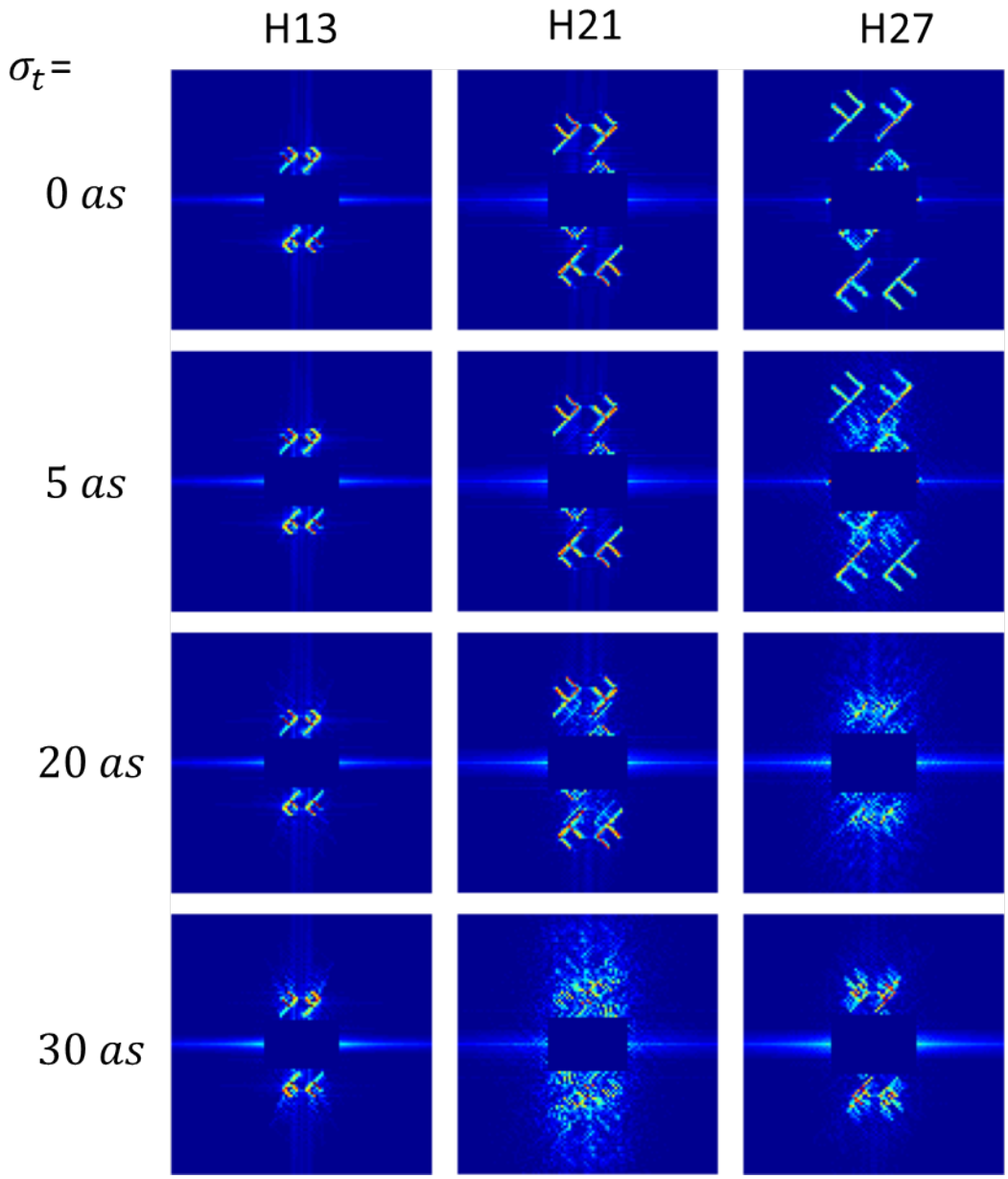

Figure 5.9: The retrieved object images using Fourier transform spectroscopy at non-uniform delay. The row label indicates the standard deviation of the random noise, while the column label indicates which harmonic is used for object retrieved.

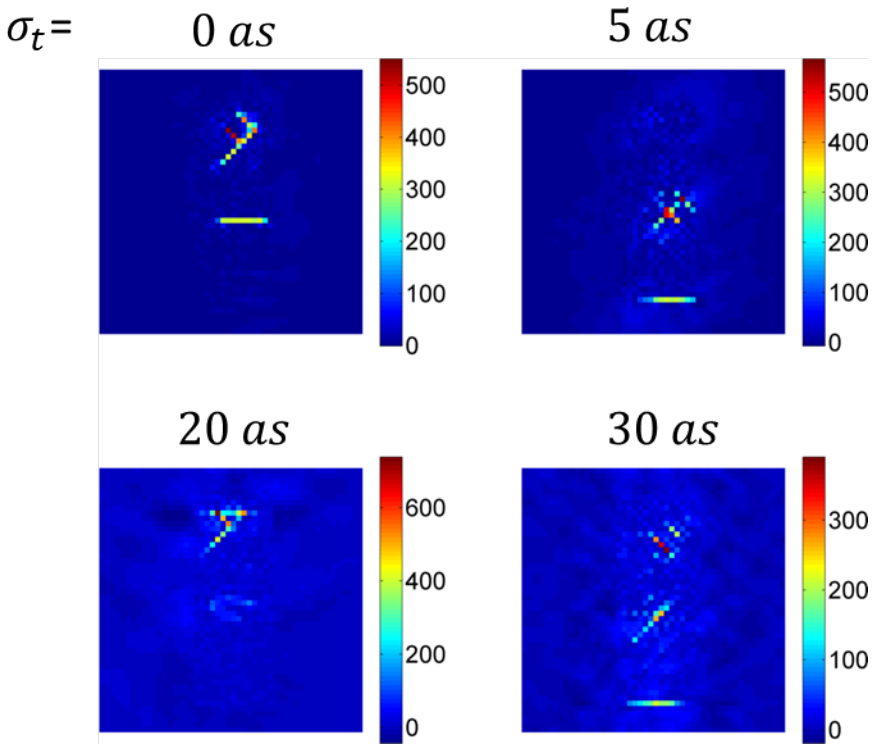

Figure 5.10: Retrieved images using OSS at various non-uniform delay noise.

Chapter 6

Broadband XUV hyperspectal coherent diffractive imaging

In this chapter, we show the experimental result for hyperspectral diffractive imaging. To our best knowledge, we have demonstrated for the first time, spectrally resolved broadband coherent diffractive imaging using the method of Fourier transform holography and Fourier transform spectroscopy.

The frequency range of our high order harmonics source contains more than one octave of frequencies. We use the same Fourier transform spectroscopy approach described in subsection 2.6 to spectrally resolve the diffraction pattern. The experimental setup for this experiment is shown in subsection 3.1. For each step we record diffraction images for 20 seconds, which consists of 10 frames each with 2 seconds exposure time, and is equivalent to illumination on the order of 10^{11} XUV photons. The total delay is 30 femtoseconds, which gives in principle, a 0.15 eV spectral resolution. Figure 6.1 shows the spectrum retrieved at a single pixel.

The imaging sample used is a 100 nm thick silicon nitride thin film with a thin Au layer for better imaging contrast. Shown in figure 6.2 , the pattern on the sample is transparent and the backgrounds are the silicon nitride and Au layers that are opaque to XUV light. The sample was patterned by electron lithography at 100 nm resolution. The pattern consists of a letter 'F', the object we want to retrieve, and a single slit for phase referencing. The slit has width of 1 µm, and 15 µm long. The 'F' is angled at 45 degree with respect to the slit.

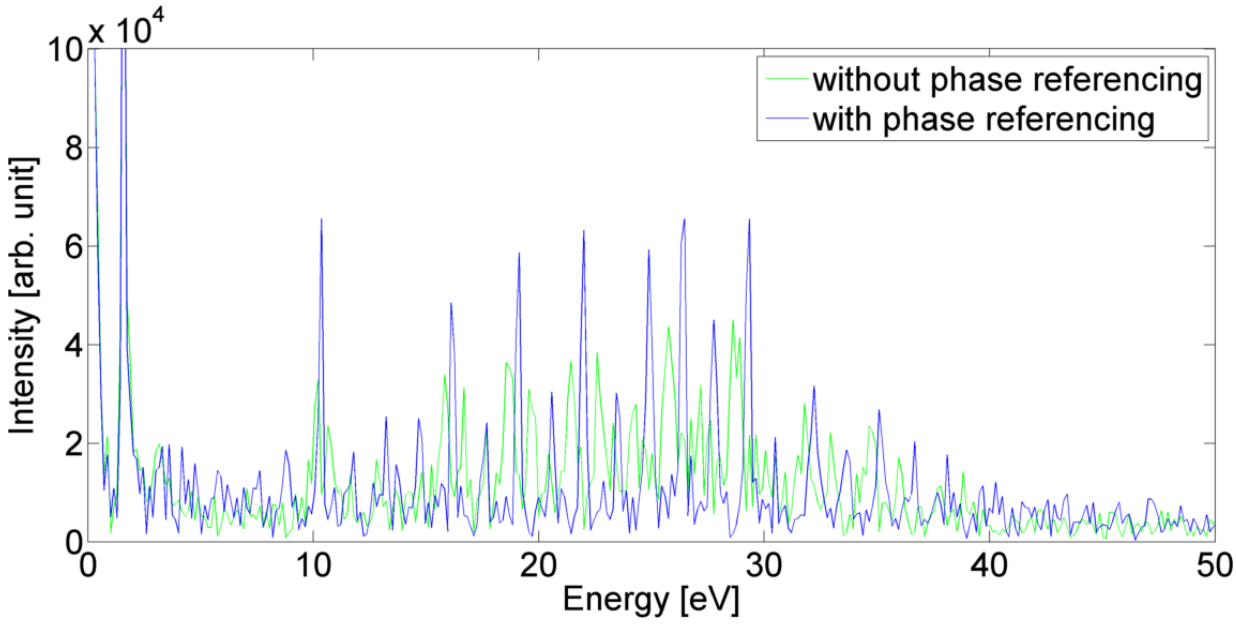

Figure 6.1: The spectrum obtained from a single pixel in the center of the diffraction pattern. After phase referencing, the peaks become evenly spaced and show the signature of the harmonic peaks. The energy axis is calibrated by comparing the ratio between the adjacent peak frequencies and odd integer numbers. Energy is converted from the harmonic numbers.

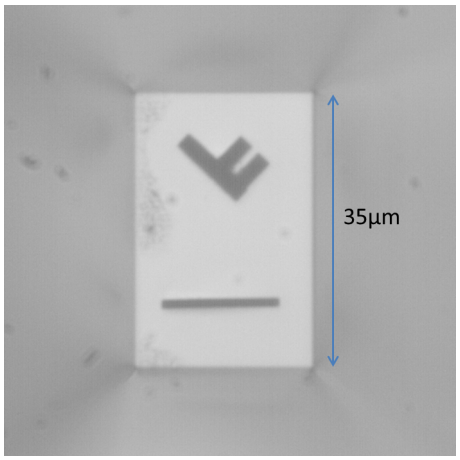

Figure 6.2: The imaging sample used for the experiment. The picture is taken with a visible microscope.

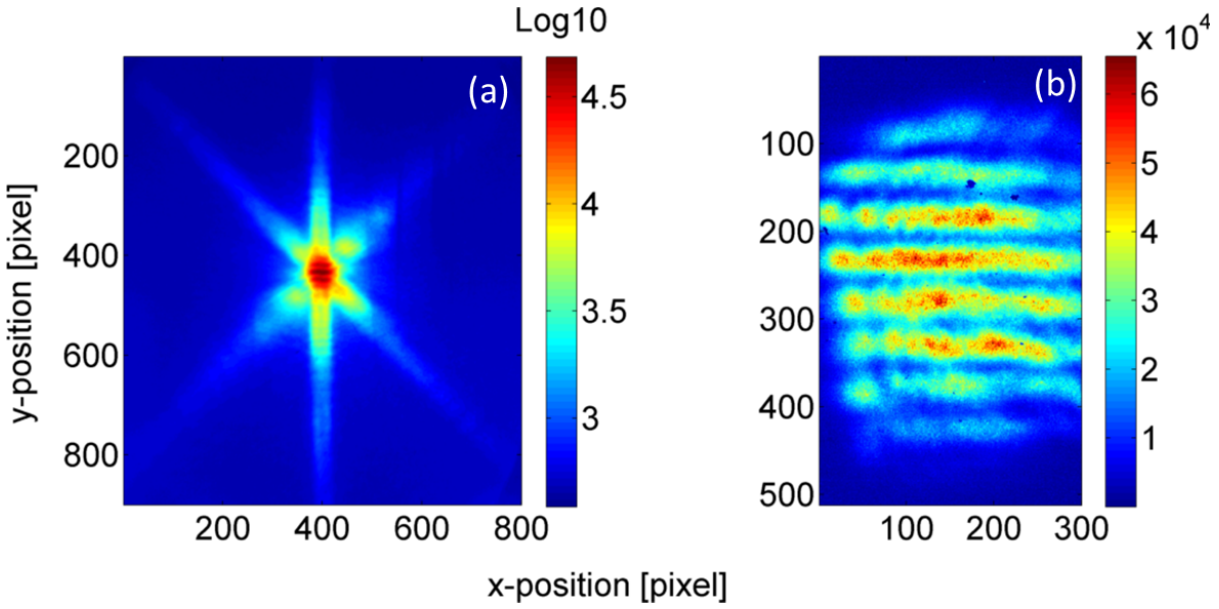

Figure 6.3: Figure a is the diffraction pattern at a stationary delay between two sources, and figure b is the 800 nm reference beam at a stationary delay. Both images were taken at a stationary optical delay of two sources.

Figure 6.3 shows the image of the diffraction pattern and the referencing beam at a stationary delay. The overall shape of the diffraction pattern is similar to our simulated data. In the diffracted pattern, the vertical line shape contains photon flux mostly from the referencing slit and the 'cross' shape from the slanted letter 'F'.

We first examine whether our experiment could spectrally filter the far-field diffraction pattern using Fourier transform spectroscopy. We chose a vertical slice from the diffraction pattern, and plotted the intensity against the photon energy (see figure 6.4). Using fit of inverse functions, we show the position of the diffraction pattern is inverse proportional to the energy, and thus proportional to the wavelength. This shows the retrieved diffraction pattern has the expected spectral dependence.

In principle, the shape of the far field diffraction pattern is the same for all wavelengths. However, the size of the diffraction pattern at an imaging screen scales with the wavelength. This relationship can be shown by the change of variable for the Fraunhofer diffraction equation 2.7.

Figure 6.5 shows the spectrally filtered diffraction pattern from the 7th harmonic to the 17th harmonic. The diffraction pattern at different harmonics are similar but at different

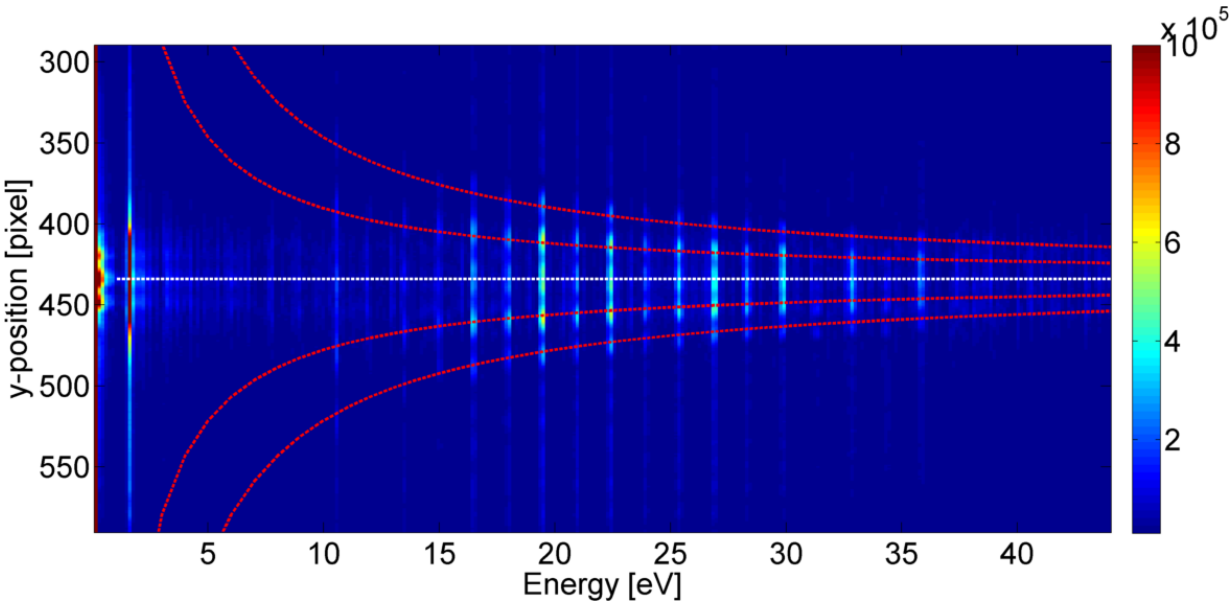

Figure 6.4: The diffraction pattern of a vertical slice at x=400 (see figure 6.3 a). The red dashed lines are inversely proportional to the photon energies.

spatial scales, which is consistent with our discussion on Fig 6.4.

Figure 6.6 shows the retrieved object using Fourier transform holography. The retrieved images show at least two well resolved copies of object 'F' from the 7th harmonic up to the 17th harmonic, which spans more than one octave of frequencies. This shows that our technique can effectively retrieve the far-field diffraction pattern across a broad range of harmonics. We speculate the uneven quality of the retrieved copies might come from the astigmatism introduced by our focusing mirrors. The non-even illumination affect the quality of phase referencing given by the slit.

As shown in figure 6.6, the retrieved images has different magnifications. The origin of magnification comes from equation 2.7. For the shorter wavelengths, each camera pixel corresponds to larger spacing in the reciprocal space. This means the diffraction pattern of higher order harmonics occupies larger area in the reciprocal space, and thus gives finer sampling in the real space. As a result, the 'F' pattern retrieved from higher order harmonics have higher magnification. This is analogous to the relationship between the spectral and temporal resolution shown in equations 2.42 and 2.43.

We measured the image resolution based on the sharpness of the retrieved object. Coherent diffraction limited resolution is also the pixel size in the retrieved images. As

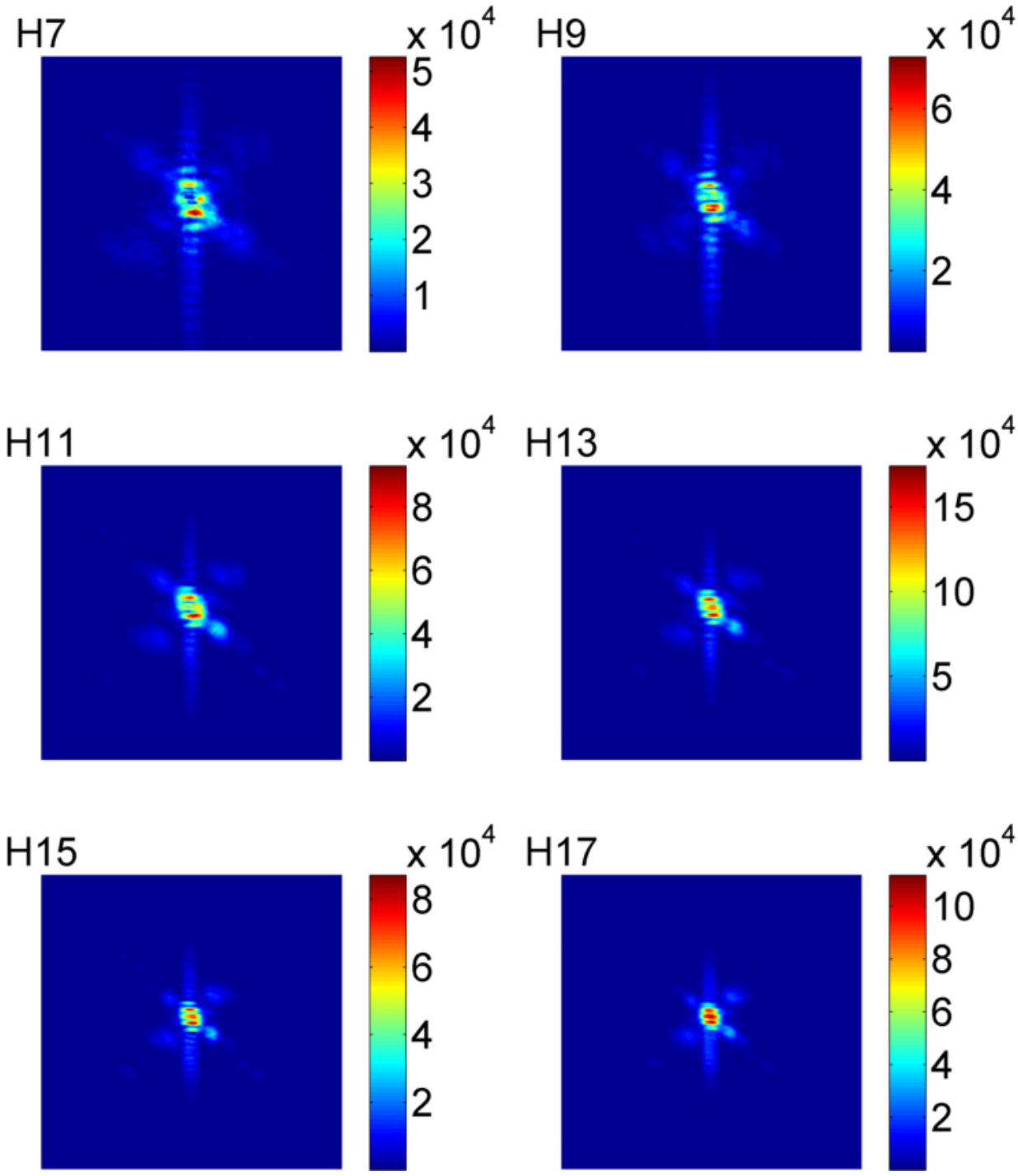

Figure 6.5: The spectrally resolved diffraction pattern from the 7th harmonic to the 17th harmonic. All diffraction patterns were collected simultaneously

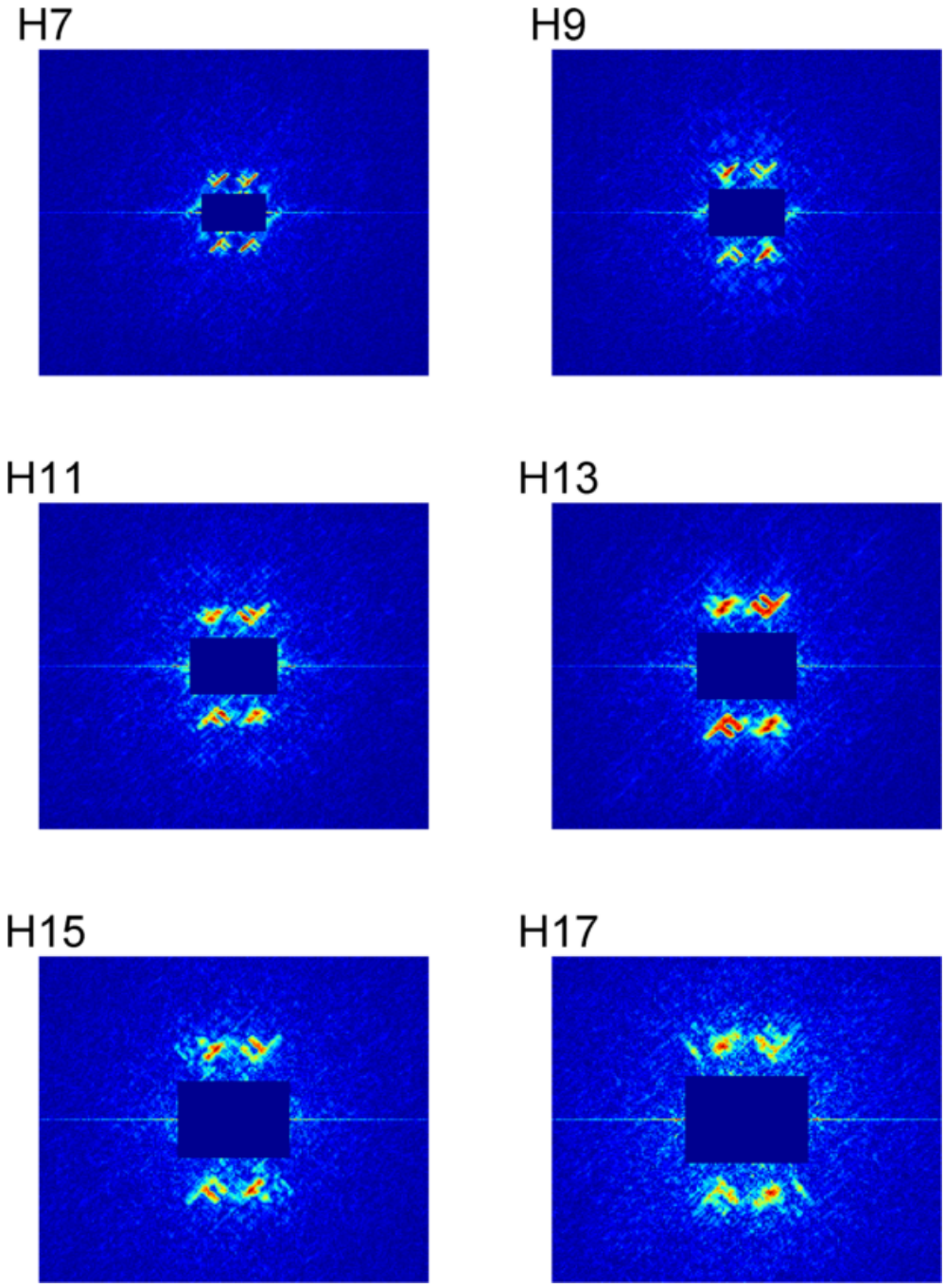

Figure 6.6: The retrieved object images from 7th harmonic to 17th harmonic. From 9th to 15th harmonic, two copies of the object were well resolved. The other two copies are less resolved. We speculate this might come from the astigmatism of our focusing geometry. The non-even illumination might affect the quality of phase referencing given by the slit.

shown in figure 6.7, we take a line cut at the retrieved image at the 13th harmonic. The drop at the edge of the retrieved 'F' pattern is close to one pixel, corresponding to 1.4 µm resolution.

The resolution of the retrieved object is limited by the width of the reference slit, the diffraction limited resolution, and the spectral resolution. The width of the reference slit is 1 µm. The numerical aperture of the setup is measured to be 0.06 . This means the diffraction limited resolution is 17 times the wavelength. The 7th and 13th harmonics each correspond to coherent diffraction limited resolutions of 2 µm and 1 µm, respectively.

In addition, the spectral limited resolution corresponding to 0.15 eV spectral resolution is 4 um at 15th harmonics. Our actual measurement shows better resolution close to 1 µm. We are not clear why this is the case as the spectral limit is based on the temporal coherence length, and is generalized for all coherent diffractive experiment. In addition, due to the magnification of the retrieved object at different wavelength. Another spectral limit given by the spectral bandwidth: d=2 µm/n, where n is the harmonic number. Finally, the width of the slit (1 µm,) is the limiting factor for all harmonics.

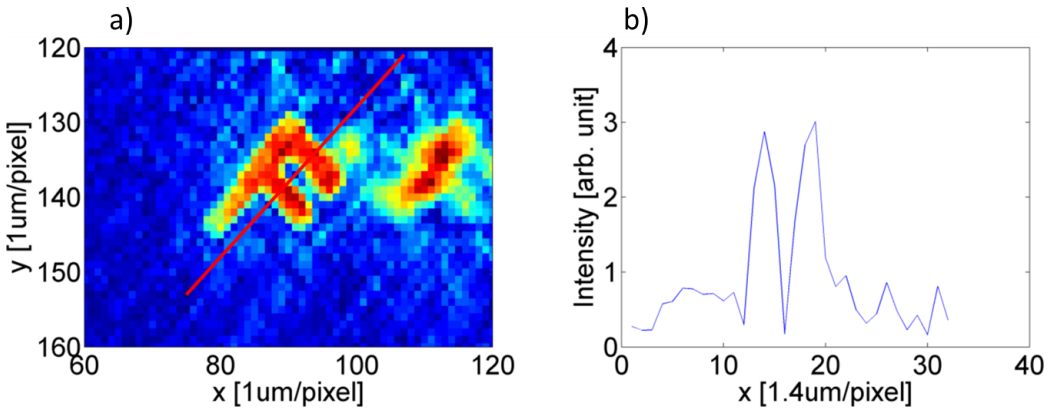

Figure 6.7: a) is the retrieved image using the 13th harmonic. b) is a linecut from the retrieved image.

In addition, we used OSS iterative phase retrieval for the image reconstruction. The retrieved images is shown in figure 6.8. This should in principle retrieve the image of the letter 'F' plus the reference slit. However, the phase retrieval does not converge to the correct image. As shown in the noise simulation from figure 4.10, as the delay noise exceeds 10 attosecond Gaussian noise, OSS cannot give the correct object retrieval for the 21st harmonic.

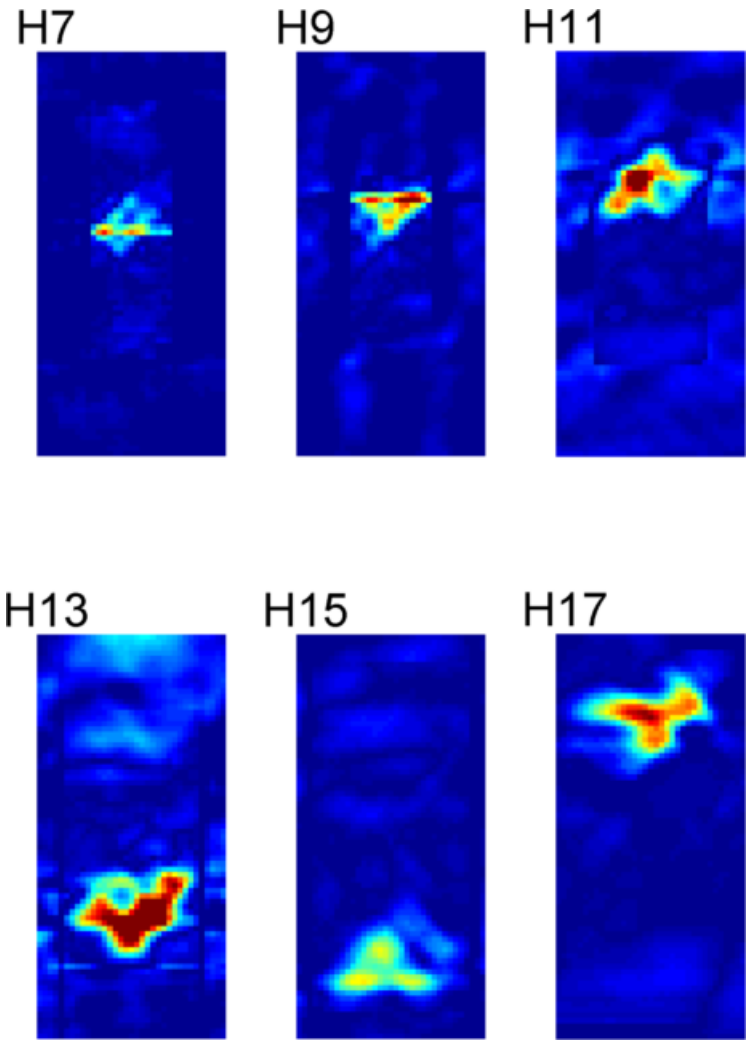

Figure 6.8: The retrieved object images from 7th harmonic to 17th harmonic using OSS phase retrieval routine. Image of F pattern is not well resolved. At harmonic 9,11, the recovered reference slit coincides with object F, whereas in harmonic 13,15,17, only F pattern is visible.

We have used the setup describe in figure 3.4, and the phase referencing was done with an 800 nm beam. Given the pixel size of our camera, we can reference the optical delay up to 50 attoseond resolution. This means our setup falls short for the requirement of coherent diffractive imaging using photon source between the 7th harmonic to 21st harmonic. However, if we can use XUV instead of 800 nm light as the reference beam, then the referencing resolution can be easily improved by one order of magnitude. For this experiment, we would need to increase the size of our vacuum chamber to accommodate the extra space required for the reference beam.

Chapter 7

Conclusion and outlook

We demonstrated hyperspectral imaging using coherent XUV source. For the first time, we combined broadband XUV high-harmonic sources, Fourier transform holography, and Fourier transform spectroscopy. We demonstrated the retrieval of spectrally resolved diffraction patterns which spans over more than one octave.

We designed a stable setup which uses the birefringent property of a calcite Wollaston prism for wave-front splitting and inline delay of the driving laser beam. This gives accurate control of the optical delay. In addition, we used a novel setup for phase referencing for correcting optical delay and pointing instability of the driving laser beam.

We demonstrated that our experimental setup is capable of 2D pixel-wise retrieval of the power spectrum. This opens future opportunities in hyper-spectral imaging using broadband high order harmonic sources. In comparison to monochromatic light sources, our scheme provides higher signal to noise ratio proportional to the number of frequencies collected.

The bandwidth from our diffraction images is well above one octave. This can be used to retrieve 3-D structural information from a single direction [55]. Using conventional coherent diffractive imaging setup, one can project the 2-D diffraction at the far field imaging plane into an Ewald sphere in the reciprocal space. Under the condition of oversampling, this projection can be interpolated to an Ewald sphere of a one voxel thick. As shown by Raine et al, using one voxel thick layer of the spherical reciprocal space, three dimensional information can be obtained through iterative phase retrieval algorithms such as Hybrid Input Output [55]. One proposal was to use a broadband source, which can potentially

provide more data points with each frequency corresponding to different radii of the Ewald sphere. Our setup provides the ideal setup for 3-D imaging from a single direction since the broadband diffraction pattern can be resolved spectrally.

In recent years, there has been rapid development of intense high order harmonic sources in the water window [7]. The common design is to use strong infrared driving laser with few optical cycles. The generation medium uses high pressure Helium gas due to its higher ionization potential. The state of the art high order harmonic source from 2014 produces $1.85 \pm 0.12 \times 10^7$ photons/s/1 % bandwidth at 300 eV [56, 46].

For coherent diffractive imaging , 10^{10} to 10^{12} photons are required to reconstruct a single image [29, 17]. The photon flux used in this thesis is on the order of 10^{10} photon at the most intense harmonic. This means the required data acquisition time for soft X-ray diffractive imaging based on Fourier transform spectroscopy can be as long as 1000 hours, well beyond a practical duration. However, we remain optimistic based on the rapid advancement in the past decade. The best photon flux produced in 2006 was 10^5 photons/s/1 % bandwidth, 2 orders of magnitude lower compared to today's number.

A short term goal for broadband coherent diffractive imaging can be imaging small nanomaterials. In figure 7.1, we plot the transmission rates of four common elements with 200 nm thickness: Mg, Ti,Al, and Si. The data is taken from X-ray database of the Center for X-Ray Optics at Lawrence Berkeley National Laboratory [57].

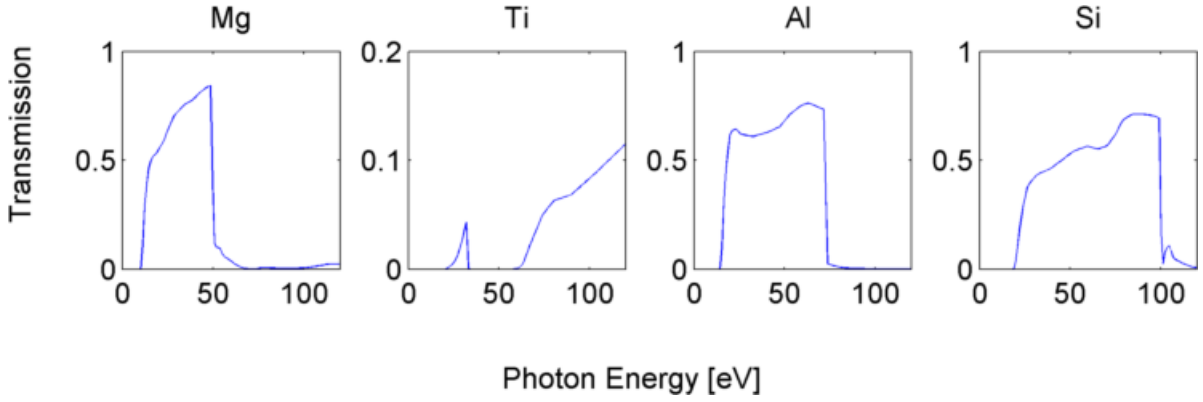

Figure 7.1: The transmission of XUV through 4 different metals.

Figure 7.1 shows sharp spectral feature at the range of 20 to 120 ev. Using the spectrally resolved coherent diffractive imaging, we can in principle retrieve material's structural

information and its spatially resolved material composition. The range of harmonics spectrum shown in figure 7.1 can be obtained using multi-cycle milijoule femtosecond pulses produced directly from commercial laser systems.

Appendix A

Derivation of Fourier transform holography

Here we derive some of the equations used for Fourier transform holography and Fourier transform spectroscopy. Similar proofs can be found in reference book [58] or paper [39].

If f(t) has the Fourier transform $F(\omega)$, and g(t) has the Fourier transform $G(\omega)$ The convolution of two functions f,g has the Fourier transform $F(s)G(s)$.

$$\begin{aligned}
\mathcal{F}[(f*g)(t)] &= \int_{-\infty}^{\infty}\int_{-\infty}^{\infty} f(\tau)g(t-\tau)e^{i\omega t}d\tau dt \\
&= \int_{-\infty}^{\infty} f(\tau)\int_{-\infty}^{\infty} g(t-\tau)e^{i\omega t}dtd\tau \quad = \int_{-\infty}^{\infty} f(\tau)\int_{-\infty}^{\infty} g(t)e^{i\omega(t+\tau)}dtd\tau \\
&= \int_{-\infty}^{\infty} f(\tau)e^{i\omega\tau}d\tau\int_{-\infty}^{\infty} g(t)e^{i\omega t}dt \\
&= F(w).G(w)
\end{aligned} \tag{A.1}$$

The cross correlation of two functions f(t),g(t) has the Fourier transform $F^*(\omega)G(\omega)$.

$$\begin{aligned}\mathcal{F}[(f\otimes g)(t)] &= \int_{-\infty}^{\infty}\int_{-\infty}^{\infty} f^*(\tau)g(t+\tau)e^{i\omega t}d\tau dt \\ &= \int_{-\infty}^{\infty} f^*(\tau)\int_{-\infty}^{\infty} g(t+\tau)e^{i\omega t}dtd\tau \quad = \int_{-\infty}^{\infty} f^*(\tau)\int_{-\infty}^{\infty} g(t)e^{i\omega(t-\tau)}dtd\tau \\ &= \int_{-\infty}^{\infty} f^*(\tau)e^{-i\omega\tau}d\tau\int_{-\infty}^{\infty} g(t)e^{i\omega t}dt \\ &= F^*.G\end{aligned} \tag{A.2}$$

This means the autocorrelation of function of f has the Fourier transform $F^*(\omega)F(\omega)$ or $|F(\omega)|^2$.

the Fourier transform of the first derivative of function f

$$\begin{aligned}\frac{d}{dt}f(t) &= \frac{d}{dt}(\int_{-\infty}^{\infty} F(w)e^{i\omega t}dt) \\ &= \int_{-\infty}^{\infty}[i\omega F(w)]e^{i\omega t}dt\end{aligned} \tag{A.3}$$

This means $\mathcal{F}(\frac{d}{dt}f(t)) = i\omega F(w)$

We can use this relation to derive the derivative rule for the convolution

$$\begin{aligned}\mathcal{F}(\frac{d}{dx}[f(x)*g(x)]) &= is[F(s)G(s)] \\ \mathcal{F}(\frac{d}{dx}[f(x)]*g(x)) &= is[F(s)]G(s) \\ \mathcal{F}(f(x)*\frac{d}{dx}[g(x)]) &= F(s)[isG(s)]\end{aligned} \tag{A.4}$$

Since Fourier transform of a function is unique, $\frac{d}{dx}[f(x)*g(x)] = \frac{d}{dx}[f(x)]*g(x) = f(x)*\frac{d}{dx}[g(x)]$

Similarly, we have the derivative rule for the cross correlation.

$$\begin{aligned}\mathcal{F}(\frac{d}{dx}[f(x)\otimes g(x)]) &= is[F(s)^*G(s)] \\ \mathcal{F}(\frac{d}{dx}[f(x)]\otimes g(x)) &= [-isF(s)^*]G(s) \\ \mathcal{F}(f(x)\otimes\frac{d}{dx}[g(x)]) &= F^*(s)[isG(s)]\end{aligned} \tag{A.5}$$

Therefore

$$\frac{d}{dx}[f(x) \otimes g(x)] = -\frac{d}{dx}[f(x)] \otimes g(x)) = f(x) \otimes \frac{d}{dx}[g(x)] \tag{A.6}$$

Properties of cross-correlation with an Dirac Delta function

set $f(x) = \delta(x - x_o)$

$$\begin{aligned} f(x) \otimes g(x) &= \int_{-\infty}^{\infty} f^*(x')g(x + x')d' \\ &= \int_{-\infty}^{\infty} \delta(x' - x_o)g(x - x')dx' \\ &= g(x_o + x) \end{aligned} \tag{A.7}$$

$$\begin{aligned} g(x) \otimes f(x) &= \int_{-\infty}^{\infty} g^*(x')f(x + x')d' \\ &= \int_{-\infty}^{\infty} g^*(x')\delta(x + x' - x_o)dx' \\ &= g(-x + x_o) \end{aligned} \tag{A.8}$$

Appendix B

Iterative phase retrieval with initial phase from Fourier transform holography

To implement HIO algorithm, an initial phase is required. This phase is usually chosen to be random. However, Fourier transform holography retrieves object directly at lower resolution. We can use the phase retrieved in Fourier transform holography to be the starting phase in a HIO algorithm. As shown in figure B.1 B.2, the initial phase from Fourier transform holography gives quicker convergence compared to random starting phase.

However, we did not find this approach to be effective against noisy data from our experiment. The information of initial phase from Fourier transform holography is lost to the contamination of noises during phase retrieval algorithm, this results in the stagnancy of the algorithm at local minimum, deviates from the desired retrieval pattern.

HIO phase retrieval with initial phase from Fourier transform holography

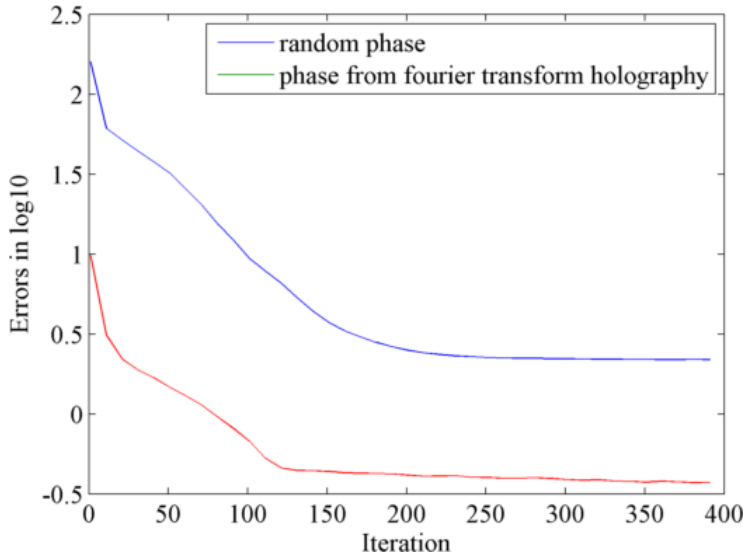

Figure B.1: The comparison between HIO algorithm using random phase and the phase retrieved from Fourier transform holography. x-axis is the iteration of the algorithms. y-axis is the sum of the absolute difference between the recovered real space at each iteration and real space of the actual object. The object can be retrieved directly from Fourier transform holography. However, its resolution is limited by the width of reference slit. Iterative phase retrieval after Fourier transform holography gives, in principle, higher spatial resolution of the recovered object. Retrieval with phase from Fourier transform holography is shown to converge faster than random phase. Using the phase retrieved from Fourier transform holography as initial iteration point, the reconstructed object shows one order of magnitude improvement.

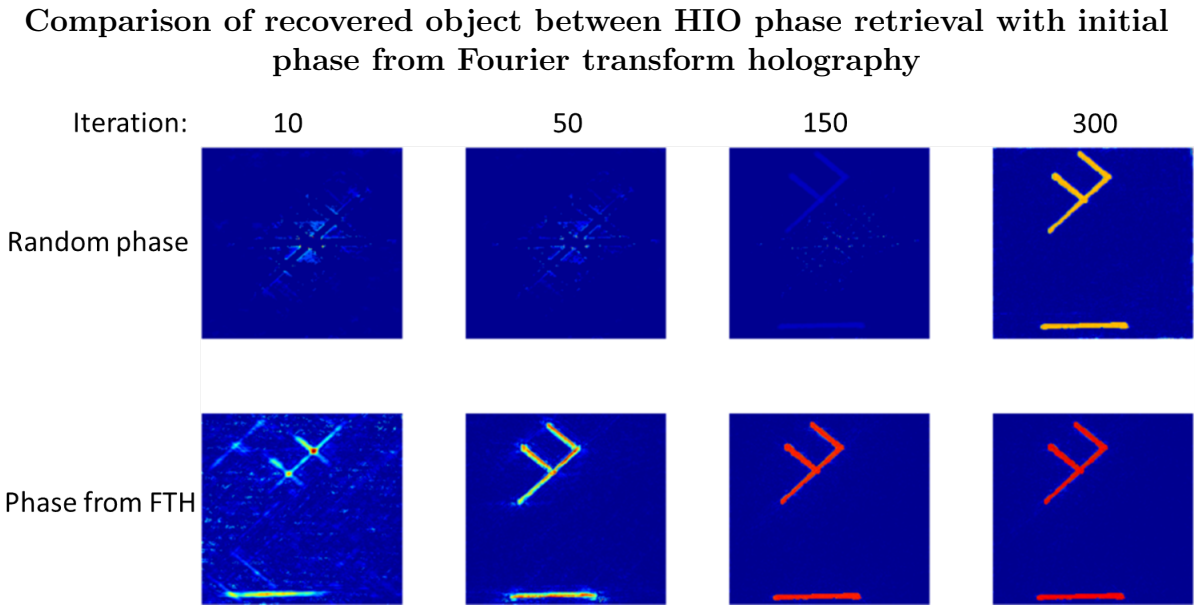

Figure B.2: We compare the efficiency of the iterative algorithm using random initial phase versus phase retrieved from Fourier transform holography.

Source codes in Matlab

B.1 Hybrid input output

```
 [record_r_space_iteration]=hio(iteration,k_space,record_r_space_iteration,
     record_r_space_iteration_points)
errors=zeros(40);

r_space=real((ifftshift(ifftn(k_space))));
for iteration = 1:300
    %sample(real(sample)>0) = buffer_sample(real(sample)>0);

% %step 1, go from object space to fourier space
         k_space = fftshift(fftn(r_space));
%
        copy_k_space=k_space;
         % step 2, meet fourier constraint, replace amplitude with exact one%
        phase_angle = angle(k_space);
        k_space = original_k_space.*exp(phase_angle*1j);

        %step3, transfer from real space to fourier space
       r_space = real(ifftn(ifftshift((k_space)))); % frequency to real space
         r_space(r_space<0|not(support_base))= error_reduction*(buffer_r_space(r_space
             <0|not(support_base)) - hio_para*r_space(r_space<0|not(support_base)));
             %reduce entire domain toward zero

        buffer_r_space=r_space;
```

```
        if rem(iteration,10) == 1
              imagesc((abs(r_space(360:590,360:570))))
             drawnow
                          iteration
        end
        for m=1:size(record_r_space_iteration_points,2)
            if iteration==record_r_space_iteration_points(m);
                record_r_space_iteration(:,:,m)=abs(r_space(360:590,360:570));
            end
        end

end
end
```

==========

B.2 Fourier transform holography

```
function [image_out]=holographic_rec(image_in,window1,window2)
        target=image_in;
        [X,Y]=meshgrid(0:size(target,2)-1,0:size(target,1)-1);
        X_max=max(max(X));
        frequency=-1:1/X_max*2:1
        B=repmat(frequency,[size(target,1),1]);

        to_plot=abs(fftshift(ifft2(double((target).*(1j*B)))));
        to_plot2=to_plot;

        y_c=round(size(image_in,1)/2);
        x_c=round(size(image_in,2)/2);
        to_plot2(y_c-window2:y_c+window2,x_c-window2-5:x_c+window2+5)=0;
        image_out=to_plot2(y_c-window1:y_c+window1,x_c-window1:x_c+window1);
end
```

B.3 RAAR

```
raar_para_i=test_b(j);
r_space=real((ifftshift(ifftn(k_space))));
to_plot_error=sum(sum(abs((fftshift(fft2(ifftshift(r_space))))-original_k_space)));
minimum=to_plot_error;
to_plot_phase=0;

for iteration = 1:300
    raar_para=raar_para_i;
    %raar_para=raar_para_i+(1-raar_para_i)*(1-exp(-(iteration/30)^3))-0.35
    r_space_pm=(pm(r_space,original_k_space));
    intermediate_r=r_space;
    phase_r_old=r_space;

    r_space=r_space*raar_para+(1-2*raar_para)*r_space_pm;
    r_space((support_base)&(2*r_space_pm-intermediate_r)>=0)=...
        r_space_pm((support_base)&(2*r_space_pm-intermediate_r)>=0);
 if iteration==300
     record_r_space_iteration_noise50_06_09_raar(:,:,j)=r_space(360:590,360:570);
 end

%%%%%%%%%%

function [output]=pm (current_real,magnitude)
        fourier_magnitude_square=abs(fftshift(fft2(ifftshift(current_real)))).^2;
        epsilon=10^(-15)*max(max(fourier_magnitude_square));

        first_part=fourier_magnitude_square./(fourier_magnitude_square+epsilon^2)
```

```
        .^0.5−magnitude;

    second_part=(fourier_magnitude_square+2∗epsilon^2)./(fourier_magnitude_square
        +epsilon^2).^(3/2).∗fftshift(fft2(ifftshift(current_real)));
output=current_real−fftshift(ifft2(ifftshift((first_part.∗second_part))));
end
```

References

[1] Paul Forman. The discovery of the diffraction of x-rays by crystals; a critique of the myths. *Archive for History of Exact Sciences*, 6(1):38–71, 1969.

[2] Joseph Goodman. Introduction to fourier optics. 2008.

[3] Weilun Chao, Peter Fischer, T Tyliszczak, Senajith Rekawa, Erik Anderson, and Patrick Naulleau. Real space soft x-ray imaging at 10 nm spatial resolution. *Optics express*, 20(9):9777–9783, 2012.

[4] M Marvin Seibert, Tomas Ekeberg, Filipe RNC Maia, Martin Svenda, Jakob Andreasson, Olof Jönsson, Duško Odić, Bianca Iwan, Andrea Rocker, Daniel Westphal, et al. Single mimivirus particles intercepted and imaged with an x-ray laser. *Nature*, 470(7332):78–81, 2011.

[5] Gelsomina De Stasio, B Gilbert, T Nelson, R Hansen, J Wallace, D Mercanti, M Capozi, PA Baudat, P Perfetti, G Margaritondo, et al. Feasibility tests of transmission x-ray photoelectron emission microscopy of wet samples. *Review of Scientific Instruments*, 71(1):11–14, 2000.

[6] Markus Mezger, Blandine Jérôme, Jeffrey B Kortright, Manuel Valvidares, Eric M Gullikson, Angelo Giglia, Nicola Mahne, and Stefano Nannarone. Molecular orientation in soft matter thin films studied by resonant soft x-ray reflectivity. *Physical Review B*, 83(15):155406, 2011.

[7] Ch Spielmann, NH Burnett, S Sartania, R Koppitsch, M Schnürer, C Kan, M Lenzner, P Wobrauschek, and F Krausz. Generation of coherent x-rays in the water window using 5-femtosecond laser pulses. *Science*, 278(5338):661–664, 1997.

[8] M Berglund, L Rymell, M Peuker, T Wilhein, and Hans M Hertz. Compact water-window transmission x-ray microscopy. *Journal of microscopy*, 197(3):268–273, 2000.

[9] Anne Sakdinawat and David Attwood. Nanoscale x-ray imaging. *Nature photonics*, 4(12):840–848, 2010.

[10] A Renieri, G Dattoli-ENEA, and Unità Tecnico Scientifica Tecnologie Fisiche Avanzate. Review of existing soft and hard x-ray fel projects. In *Proc. 27th Int. Free Electron Laser Conf*, pages 442–446.

[11] Wikimedia Commons. Aerial photo of the stanford linear accelerator center, 2007.

[12] JM Zuo, I Vartanyants, M Gao, R Zhang, and LA Nagahara. Atomic resolution imaging of a carbon nanotube from diffraction intensities. *Science*, 300(5624):1419–1421, 2003.

[13] Jianwei Miao, Yoshinori Nishino, Yoshiki Kohmura, Bart Johnson, Changyong Song, Subhash H Risbud, and Tetsuya Ishikawa. Quantitative image reconstruction of gan quantum dots from oversampled diffraction intensities alone. *Physical review letters*, 95(8):085503, 2005.

[14] Changyong Song, Huaidong Jiang, Adrian Mancuso, Bagrat Amirbekian, Li Peng, Ren Sun, Sanket S Shah, Z Hong Zhou, Tetsuya Ishikawa, and Jianwei Miao. Quantitative imaging of single, unstained viruses with coherent x rays. *Physical review letters*, 101(15):158101, 2008.

[15] Huaidong Jiang, Damien Ramunno-Johnson, Changyong Song, Bagrat Amirbekian, Yoshiki Kohmura, Yoshinori Nishino, Yukio Takahashi, Tetsuya Ishikawa, and Jianwei Miao. Nanoscale imaging of mineral crystals inside biological composite materials using x-ray diffraction microscopy. *Physical review letters*, 100(3):038103, 2008.

[16] Johanna Nelson, Xiaojing Huang, Jan Steinbrener, David Shapiro, Janos Kirz, Stefano Marchesini, Aaron M Neiman, Joshua J Turner, and Chris Jacobsen. High-resolution x-ray diffraction microscopy of specifically labeled yeast cells. *Proceedings of the National Academy of Sciences*, 107(16):7235–7239, 2010.

[17] Richard L Sandberg, Ariel Paul, Daisy A Raymondson, Steffen Hädrich, David M Gaudiosi, Jim Holtsnider, I Tobey Raanan, Oren Cohen, Margaret M Murnane, Henry C

Kapteyn, et al. Lensless diffractive imaging using tabletop coherent high-harmonic soft-x-ray beams. *Physical Review Letters*, 99(9):098103, 2007.

[18] L Poletto, F Frassetto, F Calegari, S Anumula, A Trabattoni, and M Nisoli. Microfocusing of attosecond pulses by grazing-incidence toroidal mirrors. *Optics express*, 21(11):13040–13051, 2013.

[19] Jose A Rodriguez, Rui Xu, C-C Chen, Yunfei Zou, and Jianwei Miao. Oversampling smoothness: an effective algorithm for phase retrieval of noisy diffraction intensities. *Journal of applied crystallography*, 46(2):312–318, 2013.

[20] Jianwei Miao, Tetsuya Ishikawa, Erik H Anderson, and Keith O Hodgson. Phase retrieval of diffraction patterns from noncrystalline samples using the oversampling method. *Physical Review B*, 67(17):174104, 2003.

[21] David Sayre. Some implications of a theorem due to shannon. *Acta Crystallographica*, 5(6):843–843, 1952.

[22] Jianwei Miao, Pambos Charalambous, Janos Kirz, and David Sayre. Extending the methodology of x-ray crystallography to allow imaging of micrometre-sized noncrystalline specimens. *Nature*, 400(6742):342–344, 1999.

[23] RL Sandberg, DA Raymondson, C La-O-Vorakiat, A Paul, KS Raines, J Miao, MM Murnane, HC Kapteyn, WF Schlotter, et al. Tabletop soft-x-ray fourier transform holography with 50 nm resolution. *Optics letters*, 34(11):1618–1620, 2009.

[24] Franz Pfeiffer, Timm Weitkamp, Oliver Bunk, and Christian David. Phase retrieval and differential phase-contrast imaging with low-brilliance x-ray sources. *Nature physics*, 2(4):258–261, 2006.

[25] Ian Robinson and Ross Harder. Coherent x-ray diffraction imaging of strain at the nanoscale. *Nature materials*, 8(4):291–298, 2009.

[26] Henry N Chapman, Anton Barty, Michael J Bogan, Sébastien Boutet, Matthias Frank, Stefan P Hau-Riege, Stefano Marchesini, Bruce W Woods, Saša Bajt, W Henry Benner, et al. Femtosecond diffractive imaging with a soft-x-ray free-electron laser. *Nature Physics*, 2(12):839–843, 2006.

[27] MC Scott, Chien-Chun Chen, Matthew Mecklenburg, Chun Zhu, Rui Xu, Peter Ercius, Ulrich Dahmen, BC Regan, and Jianwei Miao. Electron tomography at 2.4-angstrom resolution. *Nature*, 483(7390):444–447, 2012.

[28] Bradley J Siwick, Jason R Dwyer, Robert E Jordan, and RJ Dwayne Miller. An atomic-level view of melting using femtosecond electron diffraction. *Science*, 302(5649):1382–1385, 2003.

[29] A Ravasio, D Gauthier, FRNC Maia, M Billon, JP Caumes, D Garzella, M Géléoc, O Gobert, Jean-François Hergott, AM Pena, et al. Single-shot diffractive imaging with a table-top femtosecond soft x-ray laser-harmonics source. *Physical review letters*, 103(2):028104, 2009.

[30] Stefan Witte, Vasco T Tenner, Daniel WE Noom, and Kjeld SE Eikema. Lensless diffractive imaging with ultra-broadband table-top sources: from infrared to extreme-ultraviolet wavelengths. *Light: Science & Applications*, 3(3):e163, 2014.

[31] Wikimedia Commons. Diffraction geometry. 2007.

[32] Max Born and Emil Wolf. *Principles of optics: electromagnetic theory of propagation, interference and diffraction of light*. CUP Archive, 1999.

[33] Yoav Shechtman, Yonina C Eldar, Oren Cohen, Henry N Chapman, Jianwei Miao, and Mordechai Segev. Phase retrieval with application to optical imaging. *arXiv preprint arXiv:1402.7350*, 2014.

[34] Edwin J Akutowicz. On the determination of the phase of a fourier integral, ii. *Proceedings of the American Mathematical Society*, 8(2):234–238, 1957.

[35] Rick Trebino. *Frequency-Resolved Optical Gating: The Measurement of Ultrashort Laser Pulses: The Measurement of Ultrashort Laser Pulses*, volume 1. Springer, 2000.

[36] Ralph W Gerchberg. A practical algorithm for the determination of phase from image and diffraction plane pictures. *Optik*, 35:237, 1972.

[37] James R Fienup. Reconstruction of an object from the modulus of its fourier transform. *Optics letters*, 3(1):27–29, 1978.

[38] D Russell Luke. Relaxed averaged alternating reflections for diffraction imaging. *Inverse Problems*, 21(1):37, 2005.

[39] Manuel Guizar-Sicairos and James R Fienup. Holography with extended reference by autocorrelation linear differential operation. *Optics express*, 15(26):17592–17612, 2007.

[40] PB Corkum and Ferenc Krausz. Attosecond science. *Nature Physics*, 3(6):381–387, 2007.

[41] M Yu Ivanov, R Kienberger, A Scrinzi, and DM Villeneuve. Topical review: Attosecond physics. *Journal of Physics B Atomic Molecular Physics*, 39:1, 2006.

[42] XF Li, A LHuillier, M Ferray, LA Lompré, and G Mainfray. Multiple-harmonic generation in rare gases at high laser intensity. *Physical Review A*, 39(11):5751, 1989.

[43] Paul B Corkum. Plasma perspective on strong field multiphoton ionization. *Physical Review Letters*, 71(13):1994, 1993.

[44] AD Shiner, C Trallero-Herrero, N Kajumba, H-C Bandulet, D Comtois, F Légaré, M Giguère, JC Kieffer, PB Corkum, and DM Villeneuve. Wavelength scaling of high harmonic generation efficiency. *Physical review letters*, 103(7):073902, 2009.

[45] Eiji J Takahashi, Tsuneto Kanai, Kenichi L Ishikawa, Yasuo Nabekawa, and Katsumi Midorikawa. Coherent water window x ray by phase-matched high-order harmonic generation in neutral media. *Physical review letters*, 101(25):253901, 2008.

[46] Chengyuan Ding, Wei Xiong, Tingting Fan, Daniel D Hickstein, Tenio Popmintchev, Xiaoshi Zhang, Mike Walls, Margaret M Murnane, and Henry C Kapteyn. High flux coherent super-continuum soft x-ray source driven by a single-stage, 10mj, ti: sapphire amplifier-pumped opa. *Optics express*, 22(5):6194–6202, 2014.

[47] Vladislav S Yakovlev, Misha Ivanov, and Ferenc Krausz. Enhanced phase-matching for generation of soft x-ray harmonics and attosecond pulses in atomic gases. *Optics express*, 15(23):15351–15364, 2007.

[48] M Lewenstein, Ph Balcou, M Yu Ivanov, Anne Lhuillier, and Paul B Corkum. Theory of high-harmonic generation by low-frequency laser fields. *Physical Review A*, 49(3):2117, 1994.

[49] Peter R Griffiths and James A De Haseth. *Fourier transform infrared spectrometry*, volume 171. John Wiley & Sons, 2007.

[50] M Kovačev, SV Fomichev, E Priori, Y Mairesse, H Merdji, P Monchicourt, P Breger, Johan Norin, Anders Persson, Anne LHuillier, et al. Extreme ultraviolet fourier-transform spectroscopy with high order harmonics. *Physical review letters*, 95(22):223903, 2005.

[51] Yasuo Nabekawa, Toshihiko Shimizu, Yusuke Furukawa, Eiji J Takahashi, and Katsumi Midorikawa. Interferometry of attosecond pulse trains in the extreme ultraviolet wavelength region. *Physical review letters*, 102(21):213904, 2009.

[52] Wikimedia Commons. Wollaston-prism. 2008.

[53] Kyung Taec Kim, Chunmei Zhang, Andrew D Shiner, Sean E Kirkwood, Eugene Frumker, Genevieve Gariepy, Andrei Naumov, DM Villeneuve, and PB Corkum. Manipulation of quantum paths for space-time characterization of attosecond pulses. *Nature Physics*, 9(3):159–163, 2013.

[54] JR Fienup. Iterative method applied to image reconstruction and to computer-generated holograms. *Optical Engineering*, 19(3):193297–193297, 1980.

[55] Kevin S Raines, Sara Salha, Richard L Sandberg, Huaidong Jiang, Jose A Rodríguez, Benjamin P Fahimian, Henry C Kapteyn, Jincheng Du, and Jianwei Miao. Three-dimensional structure determination from a single view. *Nature*, 463(7278):214–217, 2009.

[56] SL Cousin, F Silva, S Teichmann, M Hemmer, B Buades, and J Biegert. High flux table-top soft x-ray source driven by sub-2-cycle, cep stable, 1.85 μm 1 khz pulses for carbon k-edge spectroscopy. *To be published in Optics Letters*, Accepted: 7 August 2014.

[57] Eric Gullikson. X-ray database, 1995-2010. http://henke.lbl.gov/optical_constants/.

[58] Ronald Newbold Bracewell and RN Bracewell. *The Fourier transform and its applications*, volume 31999. McGraw-Hill New York, 1986.